UNIVERSITY OF GENOVA

PHD PROGRAM IN BIOENGINEERING AND ROBOTICS

Microfluidic studies for monitoring the metastatic cascade and cancer-immune cells interaction

Hilaria Mollica

Thesis submitted for the degree of Doctor of Philosophy (32˚ cycle)

December 2019

Paolo Decuzzi   Supervisor

Giorgio Cannata   Head of the PhD Program

Thesis Jury:

Beatriz Pelacho Samper   External examiner
University of Navarra

Dmitry Fedosov   External examiner
Institute of Complex Systems, Jülich

Dibris

Department of Informatics, Bioengineering, Robotics and Systems Engineering

A Dino e alla mia famiglia

Declaration

I hereby declare that except where specific reference is made to the work of others, the contents of this dissertation are original and have not been submitted in whole or in part for consideration for any other degree or qualification in this, or any other university. This dissertation is my own work and contains nothing which is the outcome of work done in collaboration with others, except as specified in the text and Acknowledgements. This dissertation contains fewer than 65,000 words including appendices, bibliography, footnotes, tables and equations and has fewer than 150 figures.

Hilaria Mollica

December 2019

Acknowledgements

Abstract

Metastases are the primary cause of death in cancer patients. Small animal models are helping dissecting some key features of the metastatic cascade but many bio-mechanic details remains difficult to analyze in vivo. For this reason a series of tools for performing systematic analysis of vascular permeability, tissue architecture, blood flow, biochemical stimuli and inflammation were produced in the last decade. Particularly relevant for this field is the use of microfluidic chips allowing to include in vitro models a vascular component. During my PhD, I applied this novel technologies to replicate in vitro key steps in the metastatic cascade and cancer-immune cell interaction with a focus on the establishment of microfluidics for metastasis. More specifically I used 3 different microfluidic chips: i) a single-channel microfluidic chip allowing to study CTCs adhesion and rolling inside a small capillary; ii) a double-channel microfluidic chip, composed by an upper and a lower channels mimicking the vascular and extravascular compartments; the channels are laterally connected by an array of micro pillars acting as a vascular membrane; iii) a three channel device composed by a central 3D culture of tumor cells embedded into a collagen matrix flanked by 2 channels connected to the former by a series of trapezoidal pillars. The two lateral compartments are used to simulate the vascular and stromal environment respectively.

In the text we show how the aforementioned microfluidic devices can efficiently recapitulate in vitro multiple key steps of cancer metastatic cascade and some of the most important interactions between immune-cancer cell interactions.

Table of contents

1. INTRODUCTION

1.1 METASTATIC PROCESS

Despite considerable advances were made for the characterization, diagnosis and therapy of cancer, metastases remain a major problem causing 90% of deaths in cancer patients. The first studies on metastases started more than 130 years ago with the theory of "seed and soil"[1-2] elaborated by the English surgeon Stephen Paget. The theory states that tumor cells from the primary mass (the "seeds"), and the target organ (the "soil") are both fundamental for metastasis formation. In recent years, the correlation between cancer cell spreading and the microenvironment of colonized organs has been object of extensive studies. Among the major evidences, it was interestingly found that in most of the cases tumor cells endowed with unique properties are able to metastasize. The metastatic cells, follow these main steps: 1) detachment from the primary tumor mass, 2) intravasation in the circulatory system, 3) arrest and adhesion to the blood vessels with the consequent, 4) extravasation through the vascular walls. Once the parenchyma of distant tissues is reached, the formation of metastatic colonies starts [3-4] (**Figure.1**).

1.1.1 EPITHELIAL TO MESENCHYMAL TRANSITION

The metastatic process allows Circulating Tumor Cells (CTCs) to acquire capabilities fostering their survival in distant tissues. One of the main processes to support this phenomena is the epithelial-mesenchymal transition (EMT), a development program normally occurring during embryogenesis, or in adults, for epithelial tissue healing[5]. Tumor cells gradually and partially lose their epithelial properties and acquire mesenchymal cells features. These new properties include an augmented motility and the ability to degrade extracellular matrix (ECM) components[6] thus leading to an increased invasiveness (**Figure.1.1b and c**). EMT programs are usually triggered by stromal cells residing in the tumor niche. To boost EMT activation, these cells releases different mediators: TGF-

β, WNTs and several interleukins. From a molecular point of view this paracrine signaling is able to activate in cancer cells several transcription factors (Snail, Slug, Twist and Zeb1) as deeply documented in several studies[7]. EMT is considered a fundamental process for metastasis formation since the presence of a certain number of CTC in the primary tumor mass is a prodromal process to metastatization. It is important to note that this transformation occurs in several cancer types, such as colorectal[8], ovarian[9], pancreatic[10], prostate[11] and renal[12] and often leads to tumor resistance to chemotherapy and radiotherapy [13]. The process is anyway considered reversible: when reversion occurs, cancer cells turn back to the previous phenotype.
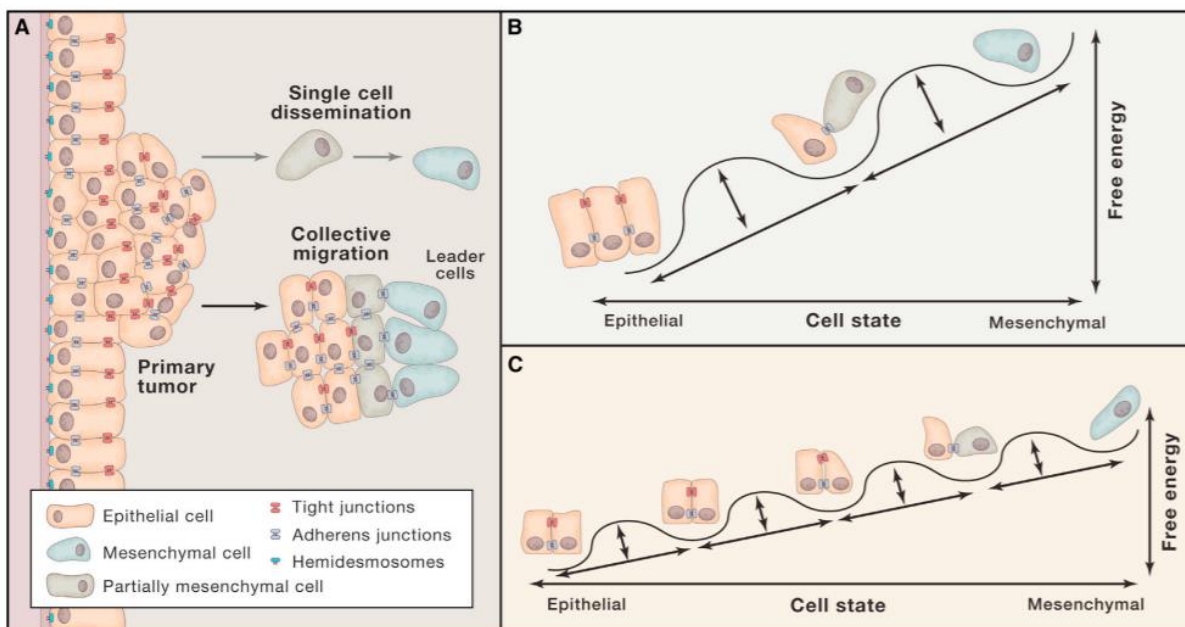
Lambert, A. W., Pattabiraman, D. R., & Weinberg, R. A. (2017). Emerging biological principles of metastasis. *Cell*, *168*(4), 670-691.

Figure 1.1 Dissemination of cancer Cells: (A) Carcinoma cell dissemination occurs via two mechanisms: single-cell dissemination through an EMT (gray arrow) or the collective dissemination of tumor clusters (black arrow). Recent evidence suggests that the leader cells of tumor clusters also undergo certain phenotypic changes associated with the EMT. (B) The epithelial state can be portrayed as the default state of residence; as cells undergo an EMT they enter into a succession of multiple epigenetic states, depicted here as free energy wells, with each state moving toward a more mesenchymal phenotype representing a higher energy state. (C) However, the barriers between states depicted here again as free energy wells, may be relatively low, resulting

in substantial spontaneous interconversion between them. This process has being manifested as phenotypic plasticity.

It is important to note that cells can invade surrounding tissues individually or in cohorts[14] driven by cancer-associated fibroblasts (CAF)[15]. In general the second scenario is more probable in those cases in which EMT is not completed and the cancer cell need to be supported during the migration by other cells providing missing functions (i.e.: matrix degrading functions)[16]. Considering the complexity and the heterogeneity of these processes many points still need to be clarified and more importantly classified, since any kind of tumor, possess its own trends and differences are appreciable also in sub-phenotypes of the same tumor. Despite this extreme complexity many studies are currently shading light on important details of the process[17]: 1) the different heterotypic signals acting on tumor cells that can activate EMT programs previously turned off; 2) the activation trends in tumor development phases; 3) how the differentiation program in normal cells influences the expression of the various components of the EMT program; 4) the role of somatic mutations (supported during the formation of the primary mass) on the activation and expression of EMT process; and 5) the roles of intracellular and extracellular signaling pathways in supporting the expression of already activated EMT programs.

1.1.2 INVASION AND STROMA INTERACTION

Once tumor cells acquires the aforementioned characteristics they start penetrating the extracellular matrix (ECM) and the interaction with the stroma is furtherly favored. Tumor cells start producing several soluble factors, which can influence stromal cell activity. For example by secreting granulocyte colony stimulator factor (G-CSF) and granulocyte macrophage-colony stimulating factor (GM-CSF), mesenchymal stem cells are attracted to the site and activated[18]. Resident mesenchymal cells and macrophages turns into CAF and tumor-associated macrophages (TAM), respectively. These activated classes of stromal cells (CAF and TAM) are deputed to secrete angiogenic factors,

proteolytic enzymes and proteins, which ultimately boost angiogenesis and lymphangiogenesis, and actively remodel the tissue favoring tumor progression. The overall process recapitulate a wound healing response[19], the substantial difference is the aim of the process: while wound healing response stimulates regeneration of normal tissues and the restoration of homeostasis, stromal cell activation in cancer promotes tumor progression in several ways: 1) CTC phenotype is supported by the continuous stimulation furnished by stromal cells. 2) Angiogenesis and lymphangiogenesis stimulate tumor growth. 3) Tissue remodeling facilitates tumor cell penetration through newly formed immature vessels; these vessels are generally highly permeable and lack in pericytes.

1.1.3 CIRCULATING TUMOR CELLS

Individual invasive carcinoma cells and invasive cohorts derived from primary tumors can transit and invade the vasculature of adjacent tissues or intravasate in the neo-vasculature assembled within the tumor. This process, as mentioned above, possibly provides a route to circulating tumor cells (CTCs) to distant sites where they can establish new metastatic colonies[20]. The transport in the vessels is a stressful process given the blood flow, shear stress, collision with other cells. Cancer cells persist in the circulation until their trap inside micro-vessels as single cells or as clusters. According to experimental data, CTC clusters introduced into the venous circulation are much more efficient than single carcinoma cells in reaching a distant tissue. Compared to single CTCs, clusters results more resistant to apoptosis, can have an advantage in the physical lodging into the vessel lumia and in post-extravasation proliferation that could contribute to their increased metastatic efficiency[21]. Furthermore, clusters are more protected from immune system attack and thus easier contribute to metastases formation, facilitating the cancer cells extravasation at distant sites (**Figure.1.2**).

Single CTCs have been extensively studied in recent years due to technical improvements in their isolation from cancer patients blood[22], they can form aggregates with platelets, leukocytes, monocytes or macrophages. Platelets can adhere to CTCs through a variety of mechanisms, one of which is the

recognition of the tissue factor expressed on the surface of some carcinoma cells[23]. Alternatively, this interaction occurs by translocation of P-selectin on the surface of activated platelets binding tumor cells. Platelets physically protect CTCs from natural killer (NK) cells elimination[24] secreting factors such as platelet derived growth factor (PDGF) and TGF-β that attenuate NK cell activity[25].

However, it is still not clear which types of CTC (single-cell or cluster) are actually responsible for metastases formation, but the probability that a single CTC successfully funds a metastatic colony is very low[26]; more probably the presence of a single CTC may be considered a marker of the presence of cell clusters in circle.
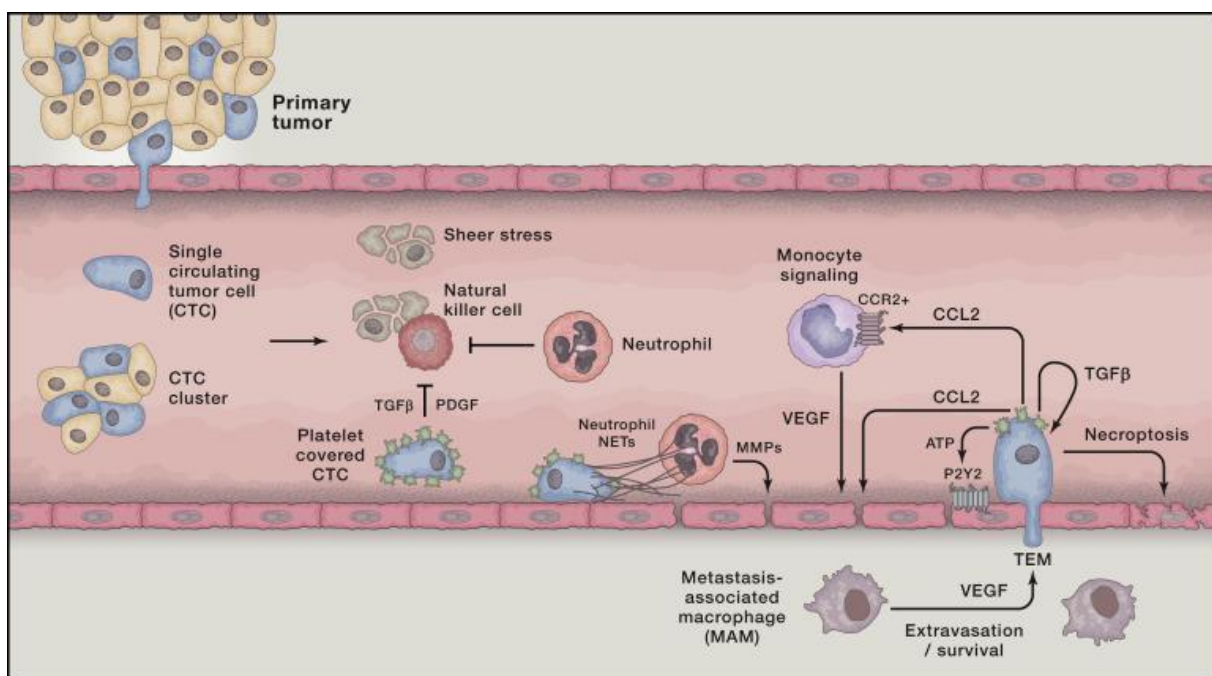
Lambert, A. W., Pattabiraman, D. R., & Weinberg, R. A. (2017). Emerging biological principles of metastasis. *Cell*, *168*(4), 670-691.

Figure 1.2. Interactions in Transit: Carcinoma cells escaping from primary tumors can intravasate into the circulation, either as single circulating tumor cells (CTCs) or as multicellular CTC clusters. The bloodstream represents a hostile environment for CTCs, exposing them to rapid clearance by natural killer (NK) cells or fragmentation due to the physical stresses encountered in transit through the circulation. Carcinoma cells gain physical and immune protection through the actions of platelets, which coat CTCs shortly after intravasation. Neutrophils can provide protection from NK cell attacks as well, while also contributing to the physical entrapment and extravasation of CTCs. Once lodged in a capillary, activated platelets and

carcinoma cells secrete a number of bioactive factors that can act on monocytes, endothelial cells, and the carcinoma cells themselves. The collective effects of these interactions promote the transendothelial migration (TEM) of carcinoma cells, which can be aided by metastasis-associated macrophages (MAMs) in the target parenchyma. In lieu of TEM, arrested carcinoma cells may also proliferate intraluminally (not shown) or induce necroptosis in endothelial cells.

1.1.4 EXTRAVASATION PROCESS

Tumor cell extravasation is a necessary process for the formation of the pre-metastatic niche. This step has similarity with leukocytes extravasation at the injury sites. A first similarity among tumor cells and leukocytes is their sensitivity to chemokines. Chemokines secreted by endothelial cells direct leukocyte subgroups to sites where their functions are required[27] and similarly attract cancer cells.

To interact and adhere to the blood vessels wall, cancer cells bind endothelial adhesion molecules, as leukocytes do. During the first transient interaction phase, both tumor cells and leukocytes loosely bind E and P Selectins on endothelial cells. A strong adhesion phase follows: ICAM-1 and VCAM-1 proteins, expressed on the endothelial cells, are bound by integrins on the counterpart[28]. After cancer cell adhesion and in order to reach interstitium, cells need overcome the endothelial barrier; this process is known as transendothelial migration (TEM), and applies to cancer cells and leukocytes as well. As for leukocyte migrating to inflammatory sites also for cancer cells the preferred route is generally the paracellular one (**Figure.1.3**)[27].

Other mechanisms are also documented: in some cases CTCs stacked in small capillaries located within secondary organs can proliferate and cause the rupture of the vessel with consequent extravasation[29].
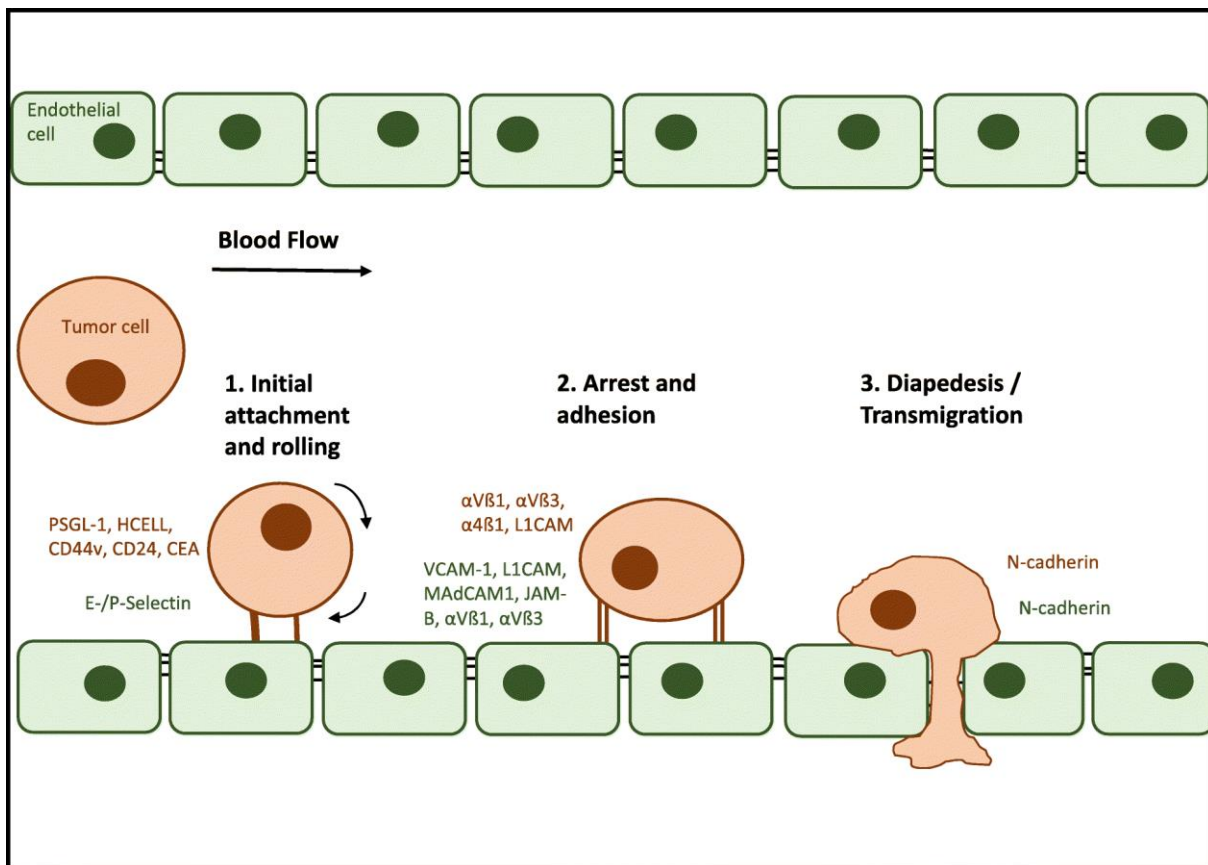
Sökeland, G., & Schumacher, U. (2019). The functional role of integrins during intra-and extravasation within the metastatic cascade. Molecular cancer, 18(1), 12.

Figure 1.3. Cancer cell extravasation: The extravasation of tumor cells. To achieve improved clarity the figure is limited to the major adhesion molecules and their interactions. Tumor adhesion molecules are shown in brown, endothelial ligands are shown in green.

1.1.5 METASTATIC COLONIZATION

Distant districts colonization is the last step of malignant tumor progression. This process depends on the ability of tumor cells to adapt to the new microenvironment. Experimental models estimate that only 0.01% of the intravenous injected tumor cells form metastases, highlighting the low efficiency of this process[30]. Furthermore, extravasated cells can undergo a dormancy phase, lasting weeks to years, in which they can be eliminated. This process was observed in several organs, including the lung, bone and brain. The residency site of dormant cells is usually the perivascular niche[31]. To date it is not clear if this process can be considered as an active retention promoted by the cell itself or

simply indicates cell inability to colonize the site due to growth factors lack[32]. In any case, it is clear instead that perivascular niche factors actively promote cell dormancy.

It was shown that stromal cells found in the new district are somehow able to activate the dormant tumor cells by producing signaling factors stimulating tumor cell expansion and colonies formation as previously mentioned for the primary mass. This considered, the comprehension of this latency phase of the metastatic colonization could allow the development of treatments aimed to stop the metastatic cascade at this phase.

1.1.6 ROLE OF THE IMMUNE SYSTEM IN THE METASTATIC CASCADE

Immune system, deputed to protect the body from a broad variety of insults, also has a role in cancer development and, most importantly in countering this process. This dual role: pro-tumor or anti-tumor, also influences the metastatic cascade. The idea that immune system could somehow interact with tumor dates back to the 19th century. Rudolf Virchow first observed leukocytes infiltrated into malignant tissues and hypothesized that tumors originated from chronically inflamed sites[33]. On the other hand, William Coley noted that a patient with inoperable sarcoma was completely cured after a concomitant infection. He is considered a pioneer in immunotherapy since after this observation he started treating cancer patients with a mixture of killed bacteria, known as Coley's toxin[34].

Tumor antigens or fragments of cancer dead cells can be absorbed by antigen presenting cells (APC), like dendritic cells (DC). DCs move to lymph nodes and present tumor-derived antigens on MHC-II to the T cells. Once activated toward a specific antigen, T cells are competent in killing cancer cells. In this ideal scenario, as reported in the work of Boon et al., adaptive immune system is able to detect cancer cells[35], after infiltrating in the tumor mass, possibly improving the cancer patients' survival[36-37]. T cells and NK cells can also protect humans from metastatic lesions[38-39]. Indeed, defects in NK expression, increase the risk of metastatic disease in solid tumors[40]. Furthermore it was observed an inverse correlation between the number of circulating or infiltrating NK cells and the presence of

metastases in patients with various solid tumors[41]. Other immune cells such as macrophages, neutrophils, eosinophils and mast cells can directly kill tumor cells by phagocytosis, the production of reactive oxygen species and the secretion of cytokines. Moreover, they are involved in the T cells recruitment into the tumor via chemokines secretion[42].

A relevant mechanism of immune evasion is the creation of an immunosuppressive environment. Different factors released by tumor cells, such as TGFβ and interleukin (IL)-10 support the differentiation of tumor-infiltrating immune cells into a tumor-promoting phenotype[43-44], leading to alterations in the immune composition of TME and (pre) metastatic organs. In addition, tumor-associated macrophages (TAMs) and neutrophils (TANs) can inhibit antitumor immune responses through the production of immunosuppressive cytokines and the expression of co-inhibitory T cell molecules. Indeed, the abundance of TAM is correlated with a negative prognosis in different types of cancer[45]. Different factors released by tumor cells can negatively stimulate myeloid cell recruitment leading alterations in the immune composition of TME and (pre) metastatic organs. Immune cells can also remodel the ECM, favoring the invasion of tumor cells and therefore their metastatization[46]. Various tumor-associated immune cells, and moreover fibroblasts and endothelial cells, influence the composition, organization and dynamics of ECM by secreting ECM remodeling enzymes, such as matrix metalloproteinases[47] (MMPs), or regulating angiogenesis and lymphangiogenesis[48].

The immune system can farther promote the CTCs survival. As mentioned in paragraph 1.1.3, the CTCs interact with platelets, promoting their activation[49]. As result, activated platelets form a fibrin clot around the CTCs, which promotes the survival of CTCs by protecting them from attack by NK cells[24]. Furthermore, regulatory T cells (Tregs) can directly provide survival factors to CTCs such as receptor activator of nuclear B-factor κB ligand (RANKL) and its activators[50]. Platelets contribute to tumor cell extravasation by promoting an invasive phenotype similar to the mesenchymal type,

through direct platelet-tumor cellular interactions, releasing TGFβ, or releasing granules containing ATP that modulate the endothelial lining and cause vascular leakage[51].

Inflammatory monocytes can also facilitate the extravasation process, helping tumor cells during migration through the vascular wall, increasing the expression of different adhesion molecules, such as ICAM-1 and E selectin on endothelial cells that are more permeable due the inflammatory factors released from these immune cells[51].

In summary, the immune system is highly connected with the metastatic cascade, and the balance between pro-tumor inflammation and anti-tumor immunity is a key factor in the cancer progression and metastasis.

1.2 CANCER IN VITRO MODELING

Both in vitro and in vivo models give us important informations on the metastatic cascade that is still the main cause of mortality in cancer[52]. The study of each step of the metastasis formation can provide new details on the cancer cells behavior and on their molecular mechanism. While in vivo systems can reproduce better the intricacy of a living system, at the same time they lack a precise control of different parameters like blood vessels sizes and flow rates, moreover analyzing by imaging these models is limited by spatial resolution. Therefore a plethora of in vitro models have been developed to gain insight about the complex processes of metastatic cascade[53]. In 2D models cells organize themselves in monolayer and in many cases this limits the similarity to in vivo scenarios; for this and other reasons 2D models were partially substituted by more complex 3D models[54]. The ideal model to study the metastatic process should take in account a series of factors including: vascularization, extracellular signals, extracellular stromal environment and the hypoxia[55]. Having all of these parameters in the same model it is not feasible to date, but many step forward have been made: 1) multiple cell types can be co-cultured into a 3D organized space; 2) ECM materials can be incorporated; 3) soluble factors can be introduced in different areas and at different time; 4) fluidics

part can be included in the design. In the following paragraphs I will go through the advancement made in modeling the metastatic cascade, starting from the first 2D models to the most advanced technologies available on this topic.

1.2.1 TRANSWELL CHAMBER

One of the most used system to characterize tumor cell migration and invasion is the transwell systems[56]. With these in vitro devices, cells migrate from one position to another, using soluble factors gradients, electric field or different matrix stiffness[57]. Generally, cells are placed in the upper compartment and migrate through a porous membrane into the lower compartment in which chemotactic agents are present. Membrane pores are generally 3-8 μm large and recapitulate the empty spaces normally present in vascular endothelium[58]. The transwell chamber is widely used to model different processes, like: cell invasion, transendothelial migration or migration across a membrane. In migration models tumor cells seeding occurs directly on the porous membrane, while in the invasion assays, cells are placed on the porous membrane that is previously covered by an extracellular matrix, like matrigel, collagen and laminin[56]. In transendothelial migration tests an endothelial cell layer covers the upper part of the membrane[59]. The test provides an extravasation model, tumor cells must first pass through the endothelium then through the membrane. Intravasation process can be modeled as well, in this case endothelial cell are seeded on the lower side of the transwell membrane while tumor cells are seeded in the upper chamber[60]. Different chemo/bio-attractants can be used for these assays: FBS, chemokines, cytokines or stromal cells such as fibroblasts. All of these assays are based on counting the number of cells passing through the porous membrane; cells can be easily recovered from the chamber and analyzed in different manner, for example using confocal microscope or flow cytometry. Some recent studies prove that cancer cells migrate three to five times more across the membrane with respect to non-cancerous cells[61]. Some of these models were tested to assess the capability of a certain drugs to reduce cancer cell migration or

invasion across the porous membrane[62-63]. Cancer cell able to invade can be than isolated and characterized for their metastatic potential[64] and their influence or interaction on other cell types including the immune cells.

1.2.2 SPHEROIDS IN METASTATIC MODEL

3D cellular architecture and surrounding microenvironment implies the use of spheroids for in vivo-metastasis models. Spheroid formation is a cell culture method in which cellular aggregates are grown in suspension or incorporated into a 3D matrix[65-66]. Spheroids are able to mimic cell-cell and cell-matrix interactions between tumor cells and the microenvironment[65] as well as properties of transport. They are more expensive and time-consuming than 2D cell culture, but are widely used for, tumor growth, proliferation, immune interactions and drugs screening, invasion studies, matrix remodeling of extracellular matrix protein, tumor angiogenesis, spreading of metastatic cells and characterization of tumor microenvironment[66-67]. There are several methods to form spheroids: suspension cultures, non-adherent surface methods, hanging drop methods and microfluidic methods[68]. In the first two methods, a matrix coating, like agarose or agar, is used to cover the plates (multiwell or dish) having a non-adherent bottom surface, this avoid cell attachment[69]. PEG (polyethylene glycol) and polystyrene plastic materials are also used as a non-adherent surface for spheroid formation. In these conditions, cells will aggregate in few days. However, not all the cells generate a spheroid but a large number of them generate aggregates of irregular shape. The suspension culture is very simple but the uniformity, in size and composition of the aggregate cannot be controlled. With non-adherent surface method, there is better efficiency, uniformity is preserved and the spheroid can be produced by cell co-culture, but it is difficult to obtain a long-term culture.

The hanging drop method and techniques employing microfluidic devices allow better a control of spheroid size and composition[68]. The hanging drop method is based on the natural disposition of cells to aggregate without the need of polymer scaffolds or microporous support, cells are simply placed

in hanging drop culture plate and incubated under physiological conditions until they form true 3D spheroids.

A microfluidic platforms for the spheroid formation, can be used to analyze important cancer progression stages such as angiogenesis, intravasation and extravasation in a controlled microenvironment, applying long-term perfusion cell cultures, maintaining high-cell viability and obtaining the aggregate formation in a very fast way[70]. Moreover microwell-based microfluidic platforms , thanks to their easiness and the possibility to monitor in real time the spheroid formation, have been used more than other methods[71].

Spheroids can better mimic low vascularized tumor masses that usually have a necrotic core[72], showing proliferation gradients and areas that resemble tumors[73]. The size of the spheroids varies between 200 and 500 μm, above 600 μm, a phenomenon of necrosis can be observed where the cells in the center of the spheroid die both by apoptosis and by necrosis, while cells in the external core remain alive thanks to their oxygen exposure[72].

1.2.3 TUMOR BIOPSY

Others in vitro models used to characterize the metastatic cascade are tumor biopsies or sections of resected tumors embedded in an ECM. This method preserve both the simplicity of an in vitro model and the complexity of the tumor microenvironment since the wide heterogeneity of the cancer tissue is conserved[74]. Cell-cell interaction and cellular morphology remain the same of what can be found in vivo but perfusion lacks.

These models are used to characterize patient metastatic cancer cells, cell morphology, cell invasiveness, cell adhesion to a different matrices, cell growth and sensitivity to chemotherapeutics and other drugs[75]. The great advantage of using this method is the development of a patient-specific model which can give some precious therapeutic indications. The tumor sections can be incorporated

into a type I collagen or matrigel matrix to mimic the ECM[76], as an alternative a single cell population can be directly isolated from the biopsy and used to perform different studies. For example, patient-derived cells can be cultured as 2D monolayers cells or as spheroids in a 3D matrix, and treated with anti-cancer compounds. Some additional studies can provide information about cancer invasiveness, metastatization probability[77-78], and some physical studies about drug penetration inside the inner part of the tissue can be carried out[79-80]. The obtained results (mainly those regarding drug screening) are usually compared with those obtained in the clinical trials[81].

1.2.4 MICROFLUIDIC DEVICES

In the last decade, the use of microfluidic chips (called 'chips' because they were initially fabricated using micro-manufacturing methods adapted from computer microchip fabrication[82]) has revolutionized the way to study the metastatic cascade and the interaction of cancer cells with the immune system. Microfluidic chip technology allows real-time imaging, high resolution, chemical or biological analysis, such as: immunoassays, drug screening, blood analysis and DNA sequencing. These devices usually made of glass, plastic or flexible polymers such as polydimethylsiloxane (PDMS), present perfusable microchannels recapitulating the in vivo physiology of specific tissues or organs[83]. Different organ on chip have been developed: lung alveoli[84] and bronchioles[85], kidney tubules[86] and glomeruli[87], small intestine[88], liver[89], bone marrow[90] and the blood–brain barrier (BBB)[91]. To mimicking the vascular compartment these channels are filled with endothelial cells which form a uniform monolayer along the channel walls; ECM gel like collagen, matrigel, or fibrinogen are instead used to simulate the extracellular space and cells from one or more type of tissue can be included to recapitulate the specific complexity of the organ. The possibility to have a series of interconnected compartments allows to culture different cells, maintaining cell-cell communication by recreating a tissue interface[92]. Living cells can be kept in the chips for short or long time (depending on the cell type) by flowing whole blood or cell growth medium into the

perfusable channels or in some dedicated reservoirs. Using syringe pumps it is also possible to recreate pressure gradient among the compartments[93]. Perfusable channels allow to analyze the recruitment of circulating cells and recapitulate the actual dosing of a certain drug reaching the surrounding tissue. Moreover, different mechanical forces as: fluid shear stress, hydrostatic pressure and tissue deformation that influence cancer cell behavior, can be invesigated[94].

There are two main branches where microfluidic has emerged as a powerful platform: the investigation of the metastatic cascade (**Figure.1.4**), and the cancer cells-immune system interaction[95]. Microfluidic chips among all in vitro models, are able to better recapitulate the dynamics of the metastatic steps[96]. Processes like: angiogenesis, tumor expansion, cell-cell interaction, epithelial-mesenchymal transition (EMT), extracellular matrices composition, microenvironmental signals and chemical gradients can be systematically explored. Immune system interactions with tumor cells during the metastatic cascade[97] is another branch in which microfluidics present a lot of advantages in terms of modeling; this is mainly due to the fact that the use of in vivo model is still disputed considering that animals, engrafted with human tumors are usually immunosuppressed. Studying immune cells – cancer cells interaction in immunosuppressed models can be challenging since the pathological conditions of the models are often not close enough to the patient's ones. To overcome this limit novel microfluidic models were generated to mimic tumor environment in a 3D and using patient derived tumor cells.
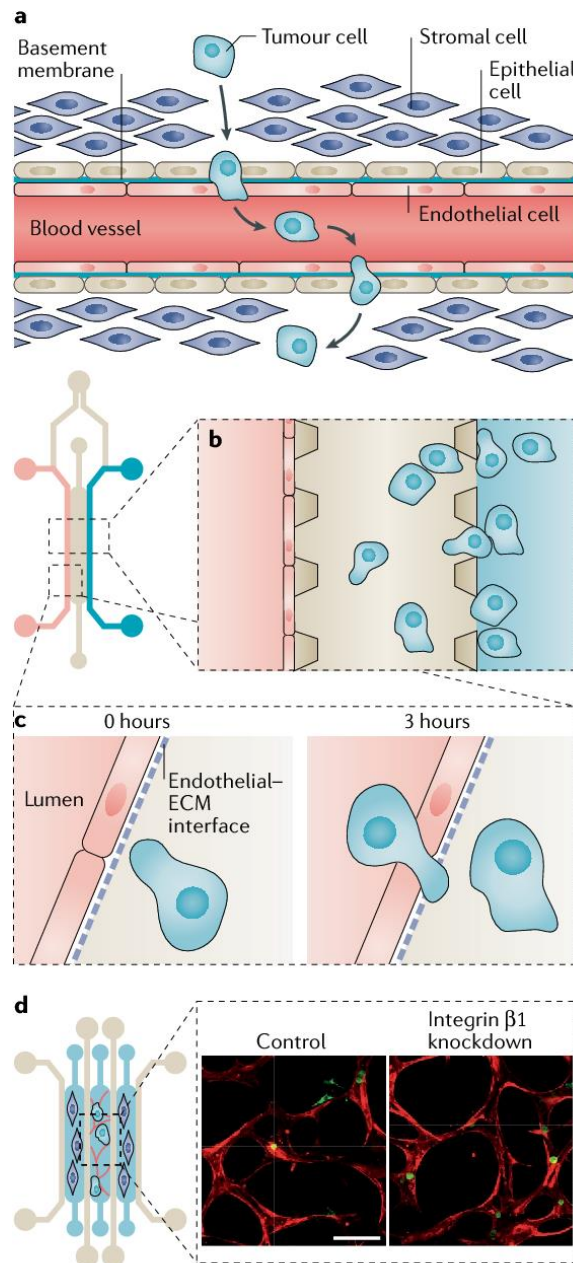
Sontheimer-Phelps, Alexandra, Bryan A. Hassell, and Donald E. Ingber. "Modelling cancer in microfluidic human organs-on-chips." Nature Reviews Cancer 19.2 (2019): 65-81.

Figure 1.4. Metastatic cancer cell dissemination models. **a.** Schematic depicting how metastatic cancer cells disseminate by invading tissue boundaries, intravasating into blood vessels, circulating through the vasculature and then extravasating at a distant site to form a new metastatic lesion is shown. A three-channel microfluidic tumour–vascular interface model is depicted that contains an endothelial channel separated from a tumour cell-lined channel by a 3D gel-filled channel. **b.** An enlarged cross section is shown of the three channels of the device, showing cancer cell dissemination towards the channel lined with endothelial cells. **c.** A zoomed in,

schematic view of the device depicting the interface between the endothelial and extracellular matrix (ECM) gel channels is shown. Cancer cell intravasation was evaluated through image-based quantification. This device enables analysis of cancer cell intravasation through the endothelial barrier (dashed line) and into the vascular lumen. **d.** A schematic of a microfluidic microvascular network platform that enables analysis of cancer cell extravasation is shown. This system was used to show that human MDA-MB-231 breast cancer cells in which β1 integrin was knocked down exhibit less trans-endothelial migration than wild-type breast cancer cells.

Here we present a series of studies regarding the microfluidic based in vitro modeling of these two important processes.

1.   Metastaitic Cascade:

To model the key steps in the metastatic cascade, microfluidic has elucidated the contributions of different cell types in the tumor progression. For example, a microfluidic chip equipped with pneumatic micro-valves for paracrine cycle analysis of human pulmonary adenocarcinoma cells and pulmonary fibroblasts has been developed. The study showed that cancer cells secrete TGFβ to stimulate fibroblasts to turn into myofibroblasts, which consequently release of other soluble factors that stimulate the tumor cell speed and migration propensity[98]. In another study the co-culture of primary human macrophages with MDA-MB-231 human breast cancer cells or PC3 prostate or MDA-MB-435S melanoma cells in a microfluidic device, revealed that secreted cytokines by macrophages stimulate the migration of tumor cells, as well as their speed and persistence[99].

Through microfluidic devices it is possible study the metastatization capability of different tumors in the extravasation and intravasation steps. In a recent study, a chip was used to visualize the interactions between HT1080 fibrosarcoma cells and human endothelial cells; when the endothelium was stimulated with tumor necrosis factor (TNF), there was an increase in the number of adhering cancer cells on the endothelial cells[100]. Therefore, this work suggests that changes in the dynamics of

tumor-endothelial cells may promote tumor cell intravasation and extravasation during the metastatic cascade.

Diffusion analysis of circulating tumor cells in vivo, revealed that metastatic cells were preferably adhered to the endothelium of the organs expressing high levels of cytokines that increase vascular permeability[101]. Other microfluidic chips have been used for the identification of tumor cell integrins, secreted factors and components of the ECM that play an essential role in the cancer cells extravasation. In the Kamm group the bone and muscle microenvironment was recreated, using a three-channel microfluidic device, seeding the HUVECs, which formed a perfusable microvascular network, primary human bone marrow-derived mesenchymal stem cells (BM-MSCs) and osteoblasts[102]. HUVEC cells and C2C12 myoblasts were used to mimic the muscular microenvironment. Then the extravasation capacity of the metastatic breast cancer cells was studied, flowing them on the endothelium. The extravasation rate increased in the bone microenvironment compared to that of the muscle, and this effect could be explained by the greater permeability of the vessels in the bone environment than the muscle[102]. In a similar study, extravasation was modelled by flowing MDA-MB-231 breast cancer cells through an interconnected microvascular network formed by HUVECs in the central channel of a microfluidic device. This model revealed that β1 integrin expression is required for cancer cells to be able to invade through the endothelial basement membrane[103].

2.   Immune system modeling:

Recently, immunology of cancer has gained momentum owing to the emergence of cell-based immunotherapy as a promising complementary strategy for anticancer treatment. One of the most studied application is the immune migration, which includes the homing of the innate immune system cells responding to infections, the extravasation at inflammatory sites, migration through the thymus during B and T cell maturation, and migration during wound healing and tissue remodeling, as well as local movements at sites of inflammation[104]. Microfluidic chips through a constant perfusion of

compounds and established conditions that provide signals like cytokines and nutrients, allow migration analysis. Wu et al. for measuring primary T-cell migration in a situation mimicking lymph node related movements[105], have used CCL21 and CCL19 which are principle cytokines governing attraction and migration within lymphoid tissues. Moon et al. investigated factors governing T-cell adhesion[106], coating the channel chip surfaces with adhesion molecules like E-selectin, ICAM-1, and VCAM-1 and studying adhesion and migration processes. Perfusion was also used to characterize neutrophil rolling under flow by Sundd et al., in this study the channel surfaces were covered with P-selectins proteins[106]. Han et al. investigated 3D neutrophil transendothelial migration through extracellular matrix across an inflammatory gradient[107]. Lymphoid migration was studied by Haessler et al. with a 3D system that measured dendritic cells movement[108].

Invasion of tumor cells has also been studied, measuring invadopodia formation[109]. The group of Jeon N.L. used RAW 264 cell line, mouse macrophages, to evaluate the cell invasion in collagen type I or in Matrigel, in the presence of triple negative human breast cancer cells MDA-MB-231. Macrophages invaded gels when breast cancer cells grown in the device but not when the tumor cells were absent[110]. These studies have revealed how the invasive behavior of cancer cells could be controlled by the presence of neighbor cells. Other variables to consider are the physical properties of the tumor microenvironment that can modify the behavior of cancer cells at tissue and organs level. For example with the use of a microchip composed of two channels separated by a porous membrane, was studied the effect of mechanical forces in lung cancer, detecting tumor cell growth suppression when physiological breathing motions were mimicked[111].

Pavesi et al., studied the migration of engineered T cells in a solid 3D matrix embedding HepG2 liver carcinoma cells. This microfluidic model was able to detect that lower oxygen levels (2%) led to reduced killing of dispersed cancer cells by engineered T cells compared with higher levels of oxygen (20%) and that the addition of the inflammatory cytokines interferon-γ (IFN-γ) or TNF significantly increased killing of cancer cell aggregates by engineered T cells[112].

These studies show how microfluidic organ chip technology offers a major advantage over static models, including transwell, spheroids and organoid cultures. This is important in the context of cancer and immune cell studies that focus on neovascularization, invasion and cancer cell dissemination, as well as for maintaining cell viability and functionality over extended times. Inclusion of a perfused endothelium offers greater clinical relevance for studying drug delivery, as well as to screen novel types of anticancer molecular, cellular and nanotechnology-based therapies, optimize treatment parameters and investigate effects of combination therapies in an in vivo-like TME[113].

Considering the possibility offered by microfluidic systems to provide novel tools aimed to finely recapitulate a series of processes which are fundamental for the comprehension of partially understood dynamic, I focused my work in applying these techniques to investigate the metastatic cascade and the role of immune cells in cancer development. I particularly emphasized my research on three microfluidic devices that allowed me to mimic the metastatization process of breast and colorectal cancers and the immune-tumor cell interaction in the pancreatic adenocarcinoma.

2. AIM OF MY WORK

The advancements made in microfluidic field in the past few years and the interest in modeling metastatic cascade and the interaction between cancer and immune cells brought me to devote my PhD to develop novel microfluidic tools aimed to investigate these processes, clarifying key aspects of their mechanisms. I used a series of microfluidic devices comprehensive of 3D cultures *in vivo*-like microenvironments and a vascular counterpart in the need to clarify the biophysical forces regulating these processes. Thus the aim of my work was than to clarify cancer cell behavior in terms of adhesion to a vascular wall, intravasation in the circulatory system, extravasation and migration in the surrounding tissue characterizing their invasiveness and their correlation with immune system.

In the first year of my PhD, I analyzed the adhesion step of both colon (HCT-15) and breast cancer (MDA-MB-231) cell lines, under static and dynamic conditions. Human Umbilical Vein Endothelial cells (HUVEC) were used to mimic the vascular walls. During my second year, I focused on the other steps of the metastatic cascade, analyzing migration, intravasation and extravasation steps of breast cancer cells (MDA-MB-231). HUVEC were used to model the vasculature, while matrigel solution was used to mimic the extracellular matrix. In the last year I looked at the interaction between T cells and pancreatic adenocarcinoma ductal cells (Panc-1). HUVEC were used to form the vessels, while collagen type I was used to mimic the extracellular matrix

3. *Deciphering the relative contribution of vascular inflammation and blood Rheology in metastatic spreading*

3.1 INTRODUCTION

The formation of distant metastasis from a primary neoplastic mass is a very inefficient biological process.[114-117] Spreading of cancer cells evolves following a precise cascade of events – the metastatic cascade – requiring cell migration away from the primary mass and intravasation into blood or lymphatic vessels, following the epithelial to mesenchymal transition; circulation within the blood stream, where cells have to survive hemodynamic stresses and immune cell recognition; extravasation, migration and proliferation at the secondary sites. Radioactive assays documented that only 1% of circulating tumor cells (CTCs) can successfully overcome all these sequential steps and eventually establish distant metastases.[118] Despite the inefficiency and complexity of the process, the vast majority of cancer patients who relapse eventually succumb because of metastases, disseminated at different secondary sites, rather than for the uncontrolled growth of the original malignancy.[119]

CTC arrest within different vascular districts is a key step in the metastatic cascade and is primarily mediated by two mechanisms: vascular occlusion, which generally occurs in the small capillary beds of the brain and lungs[120]; and vascular adhesion, which is regulated by specific interactions between receptor molecules on the endothelium and ligand molecules on CTCs.[121-122] A wide range of vascular molecules are involved in this specific adhesion process, including E- and P-selectins, $\alpha_v\beta_3$ and $\alpha_v\beta_5$ integrins, VCAM-1 and ICAM-1 adhesion molecules.[123-125] These receptors can bind several different ligands expressed on the CTC membrane, making target therapies against metastasis practically impossible. This picture is further complicated by the fact that platelets, leukocytes and CTCs tend

to form in the circulation stable aggregates that favor blood longevity and vascular deposition of malignant cells.[126-127] In this context, pro-inflammatory cytokines[128-129], such as TNF-α, IL-1β and IL-6; tumor-derived exosomes[130-131] and hematopoietic cells[132-133] have been shown to modulate the expression of adhesion molecules in specific vascular districts thus priming the formation of so called 'pre-metastatic niches' where CTCs more efficiently, and in a larger number, accumulate.

Cell-cell adhesion is strongly modulated by external forces and, as such, static assays may not always reproduce the complex interactions developing under flow within the vasculature. Intravital microcopy has been extensively employed to document cell migration within vascular and extravascular compartments,[120, 134] however these in vivo analyses lack a precise control on the governing parameters. On the other hand, microfluidic chips allow to precisely control blood vessel sizes, flow rates and the expression of vascular adhesion molecules and are amenable for high through-put systematic characterizations. A variety of microfluidic chips are being developed for studying the different steps in the metastatic cascade. For instance, the group of Kamm designed flow devices for assessing transvascular migration of cancer cells in different extravascular matrices.[135-138] The vascular adhesion and transmigration of individual and clustered CTCs was studied under chemokine stimulation (exposure to CXCL12 and SDF-1α) by various groups[139-141]. Studies of cancer cell migration within the lymphatic system were presented by Swartz and collaborators.[142] The group of Jiang focused on investigating the role of endothelial cell mechanical (cyclic shear stresses) and biochemical (exposure to TNF-α) stimulation on CTC vascular adhesion.[143] Huang and collaborators developed cellulose-based tubular artificial blood vessels for reproducing the intravasation, vascular adhesion and extravasation of cancer cells.[144]

Although red blood cells (RBCs) are known to affect the dynamics of leukocytes and CTCs, at authors' knowledge, no studies have addressed the relative roles of vascular inflammation and RBC

dynamics on the vascular deposition of malignant cells. In this work, a microfluidic chip is used to study the rolling and firm adhesion of breast (MDA-MB-231) and colorectal cancer (HCT-15) cells on a confluent layer of human vascular endothelial cells (HUVECs). The hematocrit of the working solution ranges from 0 to 40% and TNF-α is used for stimulating HUVECs. The rolling velocity and number of firmly adhering tumor cells are measured under different conditions. A Lattice-Boltzmann computational model is also included to interpret and reproduce the vascular adhesion dynamics of cells.

3.2 MATERIAL AND METHODS

Cell Culture

Human Umbilical Vein Endothelial cells (HUVEC) obtained from PromoCell were cultured using Endothelial Cell Growth supplement-mix Medium (PromoCell) supplemented with 10% FBS (GIBCO). Cells were used until passage (P) 7. Human Colorectal cancer cells (HCT-15) were purchased from ATCC and cultured according to seller's instructions using RPMI (GIBCO) supplemented with 10% FBS, L-glutammine 200 mM (EuroClone) and 10000 U/mL Penicillin (EuroClone). Experiments were made using cells till P 20. Human Breast adenocarcinoma cells (MDA-MB-231) were obtained from Perkin Elmer and were used till P 20. Cells were subcultured by the use of EMEM (Euroclone) supplemented with 10% FBS, L-glutammine 200 mM and 10000 U/mL Penicillin. All cells were seeded into a T75 tissue culture flask and incubated at 37°C with 5% of CO_2 in a humidified incubator until reaching about 90% confluence. Cells were detached via 0.25% trypsin (EuroClone) and counted using the Trypan Blue (GIBCO) exclusion test.

Cytotoxicity assay for endothelial cells

Recombinant human tumor Necrosis factor (TNF-α) was obtained from PeproTech. The cytotoxic effect of TNF-α (25 ng/mL) on HUVECs was evaluated by using the 3-(4,5-dimethylthiazol-2-yl)-2,5-diphenyltetrazolium bromide (MTT) assay (Sigma-Aldrich), at different time points. Following standard protocols, 104 HUVECs were plated in 96-well plates and after 24 hours were incubated with 25 ng/mL of TNF-α for 2, 6 and 12 h. MTT (5 mg/mL) was added to Endothelial Cell Growth supplement-mix Medium for 3 h. Next, each well was emptied out and 1 mL of ETOH 100% was added. Absorbance at 570 nm was measured via a spectrophotometer (mQuanti). Values of absorbance were expressed as percentage of TNF-α cytotoxicity.

Cancer cell adhesion on inflamed endothelial cells under static conditions

HUVECs were stained with DAPI (1:1000) (Life Technologies) and plated on 25 mm glass slide, pre-coated with 20 μg/mL of fibronectin (Sigma Aldrich). After the formation of a HUVEC monolayer, cells were treated with TNF-α (25 ng/mL) for 6 hours. In the control experiments, untreated cells were washed and the remained cells were cultured under the same conditions as per the TNF-α case. After TNF-α stimulation, HUVECs were washed three times with PBS with Ca2+ and Mg2+ and stored at 4°C for following analyses. HCT-15 cells were prepared at the concentrations of 104 cells/mL. Cells were seeded on top of HUVECs and allowed to adhere up to 4 h. After washing with PBS, pictures were acquired via a fluorescent microscope (Leica 6000) at 10X magnification. The number of adhering cells was quantified using ImageJ software (National Institute of Health, USA).

The procedures for this experiment are schematically shown in Supporting Figure.1a. After washing and removing loosely bound cancer cells, fluorescent images were taken of red fluorescent cancer cells (CM-DIL staining of the membrane) over blue fluorescent HUVECs (DAPI staining of the nucleus). The representative fluorescent microscopy pics of Supporting Figure.1b show HCT-15 cells firmly adhering to the HUVEC monolayer after 1 and 4 hours of incubation, with (+ TNF-α) and without (− TNF-α) stimulation. The density of red dots (cancer cells) grows with the duration of TNF-α stimulation. This is quantified in Supporting Figure.1c where the number of adhering cancer cells (nadh), normalized by the initial number of incubated cells (ninj = 104) and the area of the region of interest (A = 1.22□10-6 m2), is charted for 1 and 4 hours of TNF-α stimulation. A statistically significant difference in number of adhering cancer cells is observed between stimulated (blue bar) and unstimulated (orange bar) HUVECs. Specifically, after 1 hour, the normalized number of adhering tumor cells was 1.5-times larger than the corresponding control (67.72 ± 13.19 #/m2 versus 46.39 ± 8.128 #/m2, with $p < 0.001$). This difference grows higher with the duration of TNF-α stimulation. At 4 hours, the normalized number of adhering tumor cells was almost 2-times larger than the corresponding control (107.2 ± 6.46 #/m2 versus 60.29 ± 7.167 #/m2, with $p < 0.001$). Similar

26

data have been observed also for metastatic breast cancer cells (Supporting Figure.2). The cytotoxic effect of TNF-α on HUVECs was assessed, for the stimulation dose (25 ng/mL), using a conventional MTT assay. Supporting Figure.1d demonstrates that cell viability is not affected at the considered concentration upon 1, 6 and 12 hours of stimulation.

Fabrication of a single channel microfluidic chip

The single channel microfluidic chip was fabricated following protocols previously demonstrated by the authors.[48] Briefly, a SU8-50 master was used as a mold for PDMS replicas of the chip. First a 40 µm thick layer of SU8-50 photoresist (MicroChem) was spin coated on a silicon wafer (4"- P doped - <100> - 10- 20 Ω/cm2 – 525 µm thick, from Si-Mat) at 2000 rpm for 30 s. Then, the negative SU8-50 template was pre-and soft baked for solvent evaporation; exposed to UV light and baked again for epoxy crosslinking; and finally developed. This template was replicated using a mixture of PDMS and curing agent Sylgard 182 (Dow Corning Corporation), with a ratio (w:w) 10:1. Specifically, the mixture was poured on the SU8-50 template, cured in an oven at 60°C for 15 h, and moved at -20°C for 1 h. After peeling off from the template, the channel extremities of the PDMS replica were punched via a biopsy puncher (OD = 1 mm, Miltex) to form inlet and outlet ports. Finally, upon oxygen plasma treatment (Pressure = 0.5 mBar, Power = 15 w, Time = 15 s; Plasma System Tucano, Gambetti), PDMS replica was sealed with a glass slide (20 x 60 x 0.17 mm) (No. 1.5H, Deckaläser). The resulting microfluidic chip has a rectangular cross section with a width w = 210 µm, height h = 42 µm, and a port-to port length l = 2.7 cm.

Seeding of endothelial cells into the microfluidic chip

Chips were sterilized by autoclave, dried and covered with 20 µg/mL of fibronectin to allow cell adhesion. HUVECs were introduced in the channel from the inlet port at a density of 3×106 cells/mL

by using a pipette tip. Then, chips were placed in an incubator, to allow cell attachment and growth, and continuously perfused with Endothelial cell growth medium supplement-mix (PROMOCELL) until cell confluency was achieved. HUVEC monolayers were inflamed, at the occurrence, with 25 ng/mL of TNF-α for 6 or 12 hours. Each experiment was compared to untreated HUVEC monolayer (-TNF-α).

Cancer cell adhesion and rolling under dynamic conditions

The microfluidic chip was placed on the stage of an epi-fluorescence inverted microscope (Leica 6000). The working fluid was injected into the chip using a syringe pump 33 Dual (Harvard apparatus). After the tripsinization, the cancer cells were incubated for 30 minutes with CM-DIL, at 37 ˚C (0,5%, Thermofisher) according to the manufacture's protocol. Then, the cells were washed 3 times with PBS 1x (GIBCO) to remove the excess dye. Finally, the cells were re-suspended in the RPMI medium (HCT-15) or EMEM medium (MDA-MB-231), without FBS, that could interfere with the cell adhesion parameters, at 1x106 cells/mL. After each rolling experiment, a washing with PBS was performed to remove the non-adherent cancer cells from the endothelium. Tumor cells were introduced via a syringe pump on the HUVEC monolayer inside the single channel chip. The inlet port of the chip was connected to the syringe pump through a polyethylene tube (BTPE-60, Instech Laboratories), while the tube of the outlet port was in PBS, to ensure flow equilibrium. After 1 minute of flow, the interaction of tumor cells with HUVECs was recorded for 15 consecutive minutes for each experiment. Two flow rates Q were imposed via the syringe pump, namely 50 and 100 nL/min. The resulting rolling velocity of tumor cells was calculated offline by post processing the videos, using the distance traveled by the cell and divided by the time, within a region of interest (ROI) (magnification 10 X, $A = 1.22 \text{ X } 10^{-6} \text{ m}^2$). At least 15 cancer cells per experiment were monitored. Each experiment was repeated three times for each different conditions and flow rates. For the study of cell adhesion under whole blood flow, the working fluid was obtained by combining a cancer cell suspension (density of 10^6 cells/mL) with whole blood from rat, collected in a standard blood test

tubing containing 3.2% of buffered citrate to prevent clotting. The working hematocrit was fixed to 40%. Experiments and image acquisition were performed as described above.

Immunostaining and confocal microscopy analysis

HUVECs cultured in the single channel and tumor cells (HCT-15 and MDA-MB-231) were fixed with paraformaldehyde 4 % (PFA) (Sigma Aldrich), for 15 minutes at room temperature. The system was washed three times with PBS and cells were permeabilized with Triton X-100 for 10 minutes on ice followed by three washes with PBS. Then, permeabilized cells were incubated with Goat serum solution 20% (Sigma Aldrich) for 30 minutes and then incubated 3 hours with primary antibodies (Abcam) (mAb mouse Ve-cadherin, 1:100 dilution) in 10% Goat serum in PBS at 4°C. After several washes with PBS, cells were incubated 50 minutes with the secondary antibody (Abcam) (mAb goat FITC conjugated, 1:500 dilution) and DAPI dye. After washing, cells were maintained in PBS at 4°C for following microscopy analyses (Confocal microscope, A1R-A1 Nikon).

Computational modeling of cancer cell rolling and adhesion

The specific ligand-receptor mediated adhesive interactions at the interface between cancer cells and endothelium were simulated using a computational model previously developed by the authors[145-146], and adapted to this specific case. A combined Lattice Boltzmann-Immersed Boundary method is used for predicting the adhesive interaction of cells (particles) with blood vessel walls, under capillary flow. In particular, the evolution of the fluid is defined in terms of a set of nine discrete distribution functions $\{f_i\}$ (i=0,..., 8) which obey the forced dimensionless Boltzmann equation,

$$f_i(x + e_i \Delta t, t + \Delta t) - f_i(x,t) = \frac{-\Delta t}{\tau}\left[f_i(x,t) - f_i^{eq}(x,t)\right] + \Delta t F_i , \qquad (1)$$

in which **x** and t are the spatial and time coordinates, respectively; $[e_i](i = 0,\ldots,8)$ is the set of discrete velocities; Δt is the time step; and τ is the relaxation time [147]. The kinematic viscosity of the flow is related to the single relaxation time τ as $\nu = c_s^2\left(\tau - \frac{1}{2}\right)\Delta t$ being $c_s = \frac{1}{\sqrt{3}}\frac{\Delta x}{\Delta t}$ the reticular speed

of sound. The moments of the distribution functions define the fluid density $\rho = \sum_i f_i$, velocity $u = \sum_i f_i\, e_i/\rho + \frac{\Delta t}{2} F_i$, and the pressure $p = c_s^2 \rho = c_s^2 \sum_i f_i$. The local equilibrium density functions $[f_i^{eq}]$ (i=0,...,8) are expressed by the Maxwell-Boltzmann (MB) [148]. The effective forcing term accounting for the presence of an arbitrary shaped body into the flow-field, F_i, reads:

$$F_i = \left(1 - \frac{1}{2\tau}\right)\omega_i \left[\frac{e_i - u}{c_s^2} + \frac{e_i \cdot u}{c_s^4} e_i\right] \cdot f_{ib}\,, \tag{2}$$

where f_{ib} is the body force term evaluated through the immersed boundary technique. Here, external boundaries of the computational domain are treated with the known-velocity bounce back conditions by Zou and He[149]. The cells surface is decorated with ligand molecules, mediating specific adhesive interaction with counter-molecules (receptors) distributed over the vessel walls. These interfacial molecular adhesive forces are computed through a probabilistic approach determining bond formation and destruction over the entire particle surface.[150] The ligand-receptor bonds were treated as linear springs transmitting across the cell interface the mechanical force F_b

$$F_b = \sum_{l=1}^{n_l} \sigma(L_l - \lambda)\,, \tag{3}$$

with y_l the bond length for the l-th element of the n_l linear element on the discretized cell surface, respectively; λ the equilibrium bond length; σ the spring constant. Molecular bonds are generated only and only if the minimum separation distance between the cell boundary and the endothelial wall is smaller than a critical value, $y_{cr} = 5 \times 10^{-3}H$, being H the channel height. The equilibrium bond length, resulting in a null force, is chosen as $\lambda = 0.5y_{cr}$. Bond formation is regulated by a forward probability function given as

$$P_f = 1 - exp\left(-k_f N l \Delta t\right)\,, \tag{4}$$

with k_f the forward bond rate and N_l the number of ligand actually probing the surface over the total number of linear elements n_l. At each time step, a pre-existing bond can be destroyed according to the reverse probability function given as

$$P_r = 1 - exp\left(-k_{r0}exp\left(\frac{(\sigma - \sigma^{eq})(y_l - \lambda)^2}{2k_B T}\right)\Delta t\right). \tag{5}$$

Here, k_{r0} is the reverse bond rate, σ^{eq} is the equilibrium spring constant (taken as 0.5σ), and $k_B T$ is the thermal potential. The ligand-receptor bonds were characterized by an adhesive bond strength σ =1 and a biochemical affinity $k_f/k_{r,0} = 8.5 \times 10^3$. The ratio between the number of ligands decorating the surface of cancer cells and the number of receptors expressed on the endothelium is ρ_l.

The diameter of cancer cells $d = 15 \pm 3$ µm was quantified via bright field microscopy (see **Figure3.8**). At time zero, cancer cells were placed next to the endothelial wall, with a separation distance of $y_0 = 3 \square 10^{-3}$ H and a null velocity. Simulations were performed in a rectangular computational domain, with height H (= 42 µm) and length 10H, resembling the longitudinal cross section of the single channel in the microfluidic chip. A linear pressure drop ($\Delta p = \frac{8\mu}{\pi} \left(\frac{H}{2}\right)^{-4} Qx$) was imposed along the channel from the inlet section (x = 0) to the outlet section (x = 10 H); zero slip velocities were applied at the bottom and top walls in order to reproduce a parabolic velocity profile.

For deformable cancer cells, a dimensionless capillary number Ca ($= u_{max}H/E_l$) $= 10^{-2}$ was considered. This number is defined as the ratio between the max flow velocity u_{max} (= 94.48 µm/s for Q = 50 nL/min; = 188.96 µm/s for Q = 100 nL/min), the channel height H (= 42 µm); and the Young's modulus of the cell (E_l = 100 Pa).

3.3 RESULTS AND DISCUSSION

A continuously growing body of evidence documents that vascular inflammation supports the firm adhesion of circulating tumor cells (CTCs) and facilitate the distant colonization of otherwise healthy tissues with the consequent formation of tumor metastases.[128-131] In this context, human vascular endothelial cells (HUVECs) were stimulated with the pro-inflammatory cytokine TNF-α and the adhesion propensity of cancer cells (HCT-15 and MDA-MB-231) was assessed under static and dynamic conditions. The two cell lines are among the most metastatic and aggressively growing colon and breast cancer cells, respectively.[151-152]

Cancer cell adhesion on inflamed endothelial cells under dynamic conditions. HUVECs were seeded in multiwell plates and, after reaching confluency, were stimulated with TNF-α (10 ng/mL, 25 ng/mL 50 ng/mL) for 6 hours. Cancer cells were added to the multiwell plates and left interacting with the endothelial cells up to 4 hours, under static conditions. In agreement with a large body of literature, these static experiments continue to confirm that endothelial stimulation with a pro-inflammatory cytokine (TNF-α) favors CTC vascular adhesion in a dose dependent manner (**Figure.3.1** and **2**).
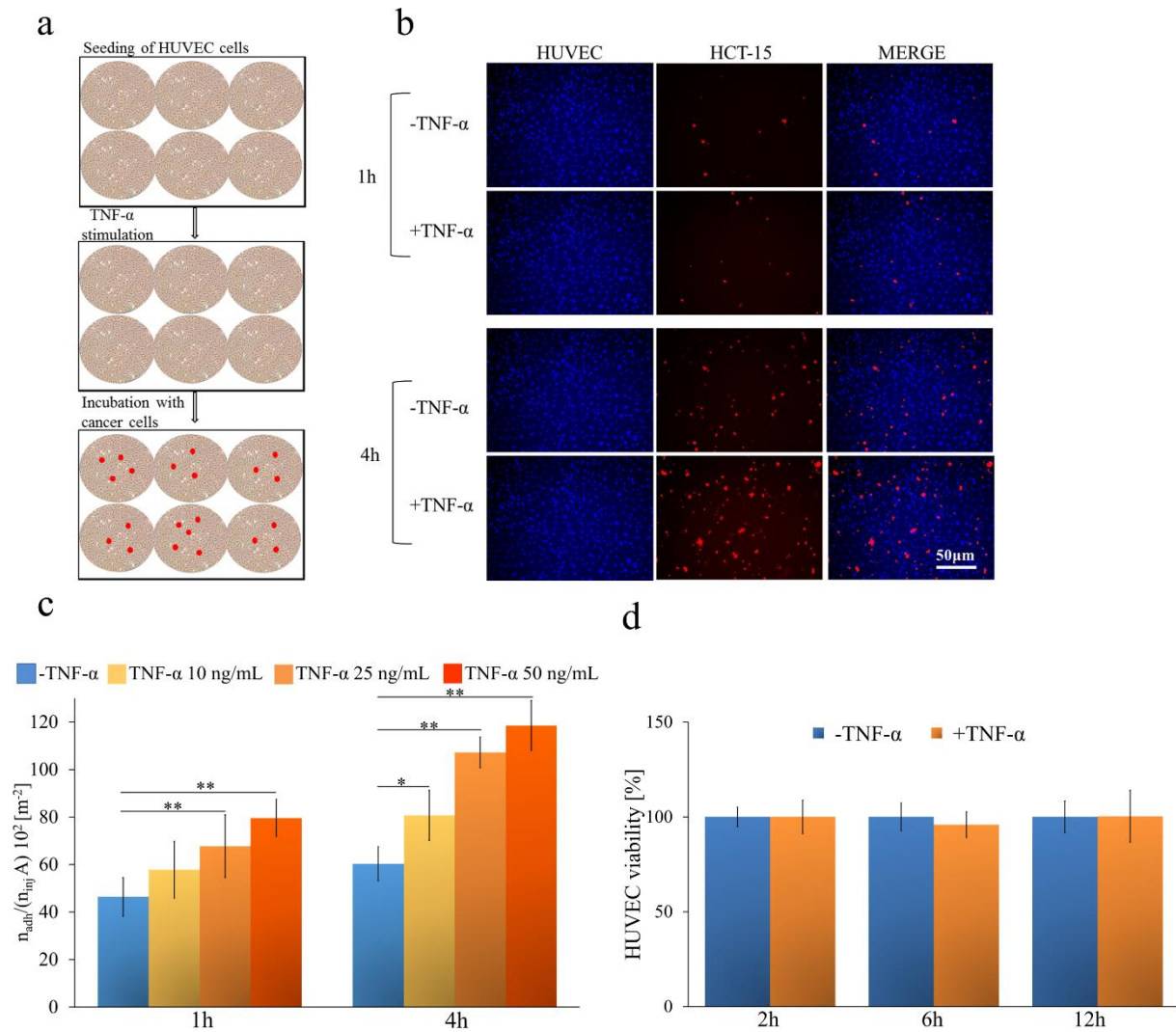
Figure 3.1. Cancer cell adhesion on inflamed endothelial cells under static conditions. **a.** Schematic representation of tumor cells adhering to a TNF-α inflamed endothelial monolayer cultured in a 6-well plate (TNF-α stimulation for 4 hours at 25 ng/mL). **b**. Representative fluorescence microscopy images of HUVECs (cell nuclei stained in blue with DAPI) and colon cancer cells HCT-15 (cell membrane labeled in red with CM-DIL) at 1 and 4 hours post stimulation with TNF-α. (- TNF-α: control experiment with no stimulation; + TNF-α: stimulation at 25 ng/mL) **c**. Normalized number of adhering cancer cells (HCT-15) on a HUVEC monolayer, with and without stimulation with TNF-α (10 ng/mL, 25 ng/mL, 50 ng/mL) ($n_{inj} = 10^4$ cells; A = 1.22 x10^{-6} m^2). **d**. Cell viability of HUVECs exposed at TNF-α (25 ng/mL) for 2, 6, and 12 hours. (Data are plotted as mean ± SD. n ≥ 5. Statistical analysis ANOVA: * denotes significant difference with p < 0.05, ** denotes significant difference with p < 0.001).
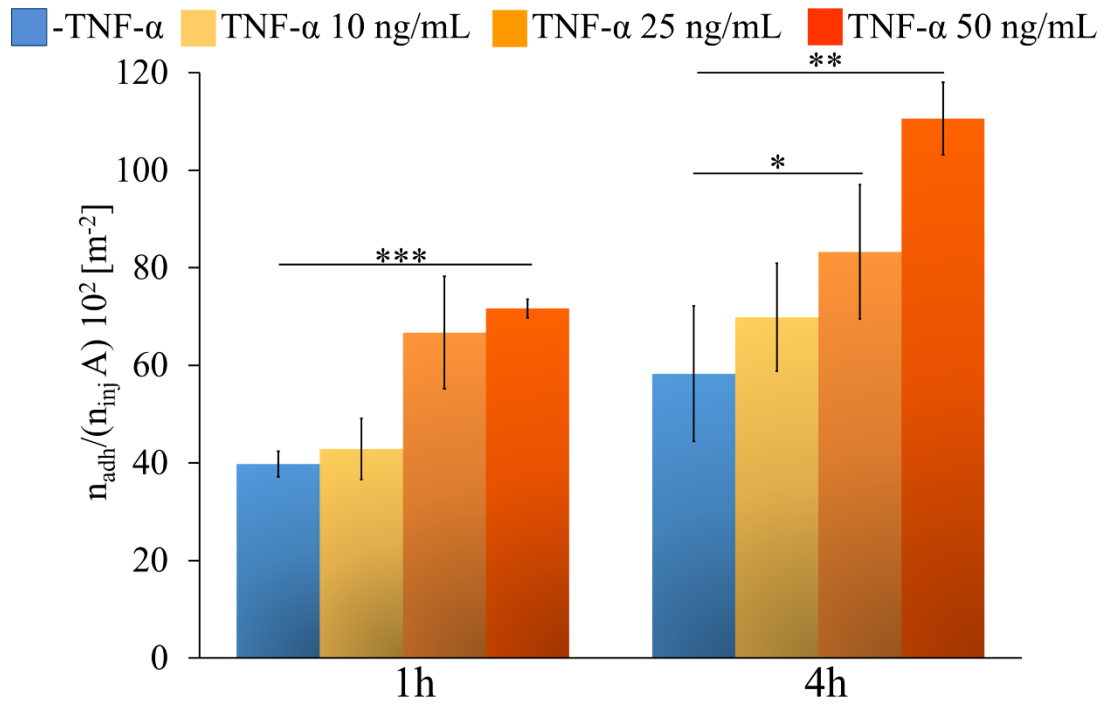
Figure.3.2 Cancer cell adhesion on inflamed endothelial cells under static conditions. Normalized number of adhering cancer cells (MDA-MB-231) on a HUVEC monolayer, with and without stimulation with TNF-α (10 ng/mL, 25 ng/mL, 50 ng/mL) ($n_{inj} = 10^4$ cells; $A = 1.22 \times 10^{-6}$ m^2). Data are plotted as mean $\pm$ SD. $n \geq 3$. Statistical analysis ANOVA. * denotes significant difference with $p < 0.05$.** denotes significant difference with $p < 0.01$. *** denotes significant difference with $p < 0.0001$.

Moving from static to dynamic experimental conditions, a PDMS single-channel microfluidic chip was used for monitoring the interaction of cancer and endothelial cells under flow (**Figure**.**3**.**3a**). The microfluidic channel was 2.7 cm long and had a 210 µm wide by 42 µm high rectangular cross section. The working fluid was introduced in the PDMS chip continuously for about 15 minutes at two different flow rates, namely 50 and 100 nL/min. These flow rates reproduce wall shear rates (13.49 and 26.99 s^{-1}) and mean blood velocities (94.48 and 188.9 µm/s) typically found in the microcirculation.[153] The PDMS channel was covered by a confluent layer of endothelial cells mimicking the blood vessel walls; whereas the cancer cells were dispersed within the working fluid consisting of either cell culture media or whole blood. Again, two different malignant cell lines were

considered, namely colon (HCT-15) and breast cancer (MDA-MB-231) cells. In order to reproduce an inflamed endothelium, the HUVEC monolayer was stimulated with the pro-inflammatory cytokine TNF-α. Representative confocal fluorescent images of the experimental set-up with cells are shown in **Figure.3.3b**. Red fluorescent cancer cells (CM-DIL staining of the membrane) are spotted firmly adhering over blue fluorescent HUVECs (DAPI staining of the nucleus). The same images show in green VE-cadherin molecules decorating the boundary between two adjacent endothelial cells and demonstrating the high level of confluency of the endothelial monolayer deposited on the microfluidic channel surface.
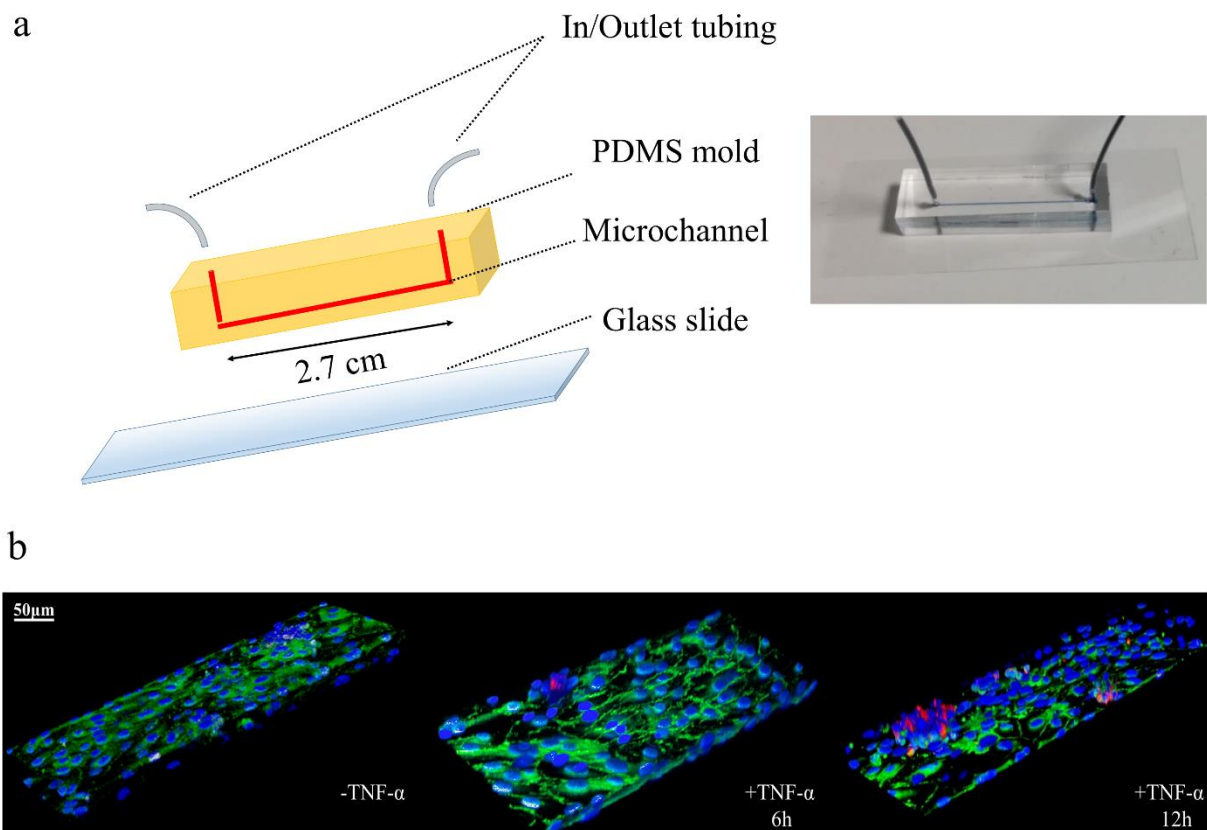

Figure 3.3. Single-channel microfluidic chip. a. On the left, schematic representation of a single channel microfluidic chip with length l = 2.7 cm, width w = 210 µm; height h = 42 µm. On the right, a single channel microfluidic chip, with connecting inlet and outlet tubing, filled with a blue ink and placed on the stage of a fluorescent inverted microscope. **b**. Representative confocal fluorescent microscopy images of HCT-15 cells (membrane labeled in red with CM-DIL) flowing in the chip and interacting with a confluent layer of HUVECs (nuclei stained in blue with DAPI). VE-cadherin adhesion molecules, arising at boundaries of the endothelial

cells, are stained in green. (Images are provided for unstimulated (-TNF-α) and TNF-α stimulated HUVECs for 6 (+ TNF-α 6h) and 12 hours (+ TNF-α 12h). TNF-α concentration: 25 ng/mL. Scale bar: 50 µm).

Via fluorescent microscopy, the number of adhering cells was quantified, within five different regions of interest (ROIs) along the channel, and normalized by the total number of injected cells ($n_{inj} = 10^6$) and the ROI area. This was performed for twelve different working conditions depending on the types of cancer (colon and breast); flow rates (50 and 100 nL/min) and levels of HUVEC inflammation (un-stimulated: -TNF-α; 6 hours stimulation: +TNF-α 6h; and 12 hours stimulation: +TNF-α 12h). Results are provided in **Figure.3.4b** and **d**, respectively, for a flow rate Q = 50 and 100 nL/min, and for breast cancer (blue bars) and colon cancer (red bars) cells. On the left hand side, **Figure.3.4a** and **c**, representative fluorescent microscopy images are shown for unstimulated, 6 hour stimulated, and 12 hour stimulated HUVECs.
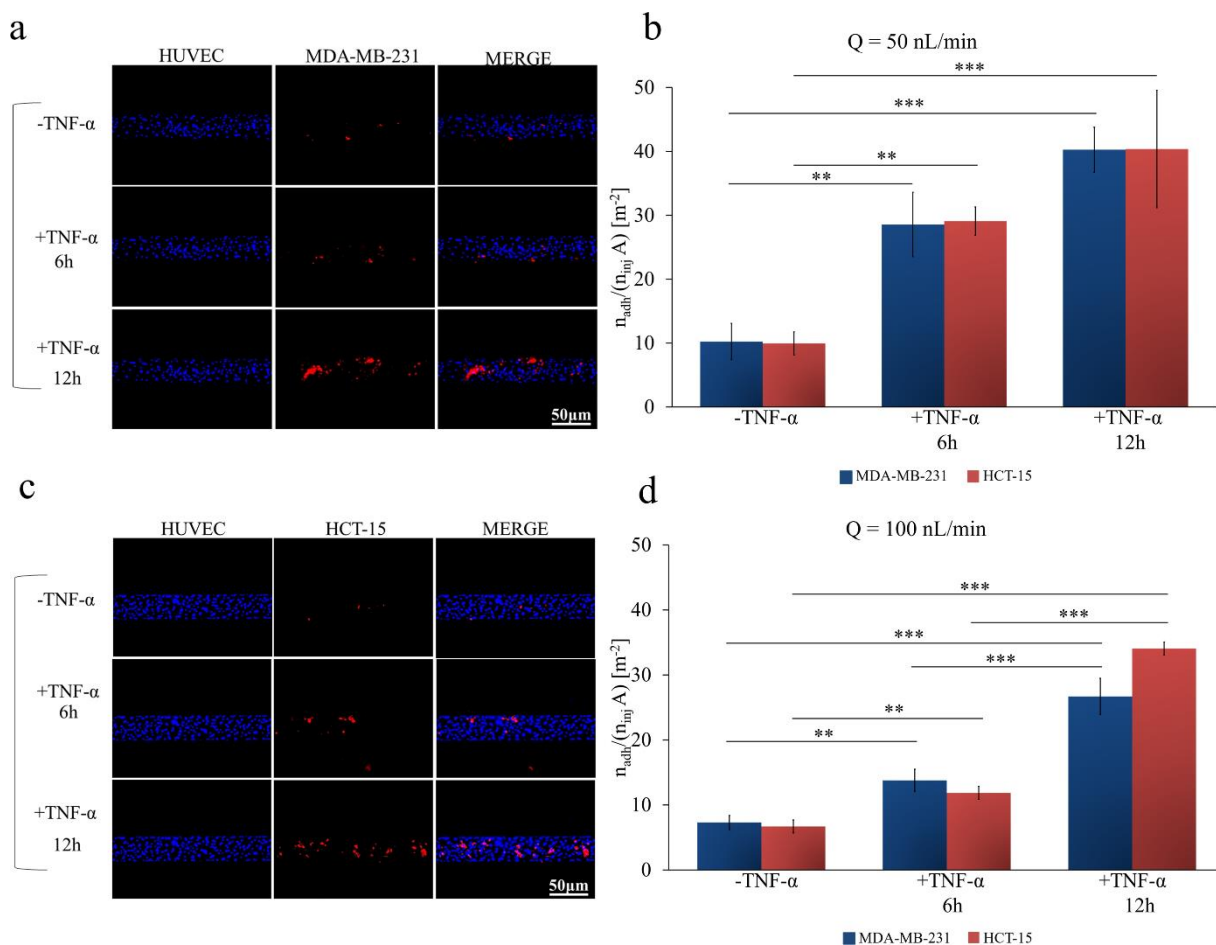
Figure 3.4. Cancer cell adhesion on inflamed endothelial cells under dynamic conditions. a. Representative fluorescence microscopy images of breast cancer cells MDA-MB-231 (cell membrane labeled in red with CM-DIL) flowing and interacting, in a single-channel microfluidic chip, with a confluent monolayer of HUVECs (cell nuclei stained in blue with DAPI). **b.** Normalized number of adhering cancer cells on a HUVEC monolayer at a flow rate of 50 nL/min, with and without stimulation with TNF-α (25ng/mL), for 6 and 12 hours. **c.** Representative fluorescence microscopy images of colon cancer cells HCT-15 (cell membrane labeled in red with CM-DIL) flowing and interacting, in a single-channel microfluidic chip, with a confluent monolayer of HUVECs (cell nuclei stained in blue with DAPI). **d.** Normalized number of adhering cancer cells on a HUVEC monolayer at a flow rate of 100 nL/min, with and without stimulation with TNF-α (25ng/mL), for 6 and 12 hours. (Data are plotted as mean $\pm$ SD. n = 3. Statistical analysis ANOVA: *** symbol denotes statistically significant difference p < 0.0001; ** symbol denotes statistically significant difference p < 0.001. (n_{inj}=10^6 cells and A = 1.22 x10^{-6} m^2). HUVECs are not stimulated with TNF-α (-TNF-α) or stimulated with 25 ng/mL TNF-α for 6h (+TNF-α 6h) or 12h (+TNF-α 12h)).

Notably, for all twelve different working conditions, no statistically significant difference was depicted when comparing breast and colon cancer cells. Conversely, significant differences arose when considering different flow rates and levels of TNF-α stimulation. At Q = 50 nL/min, the normalized number of adhering HCT-15 and MDA-MB-231 cells was, respectively, 9.952 $\pm$ 1.803 and 10.24 $\pm$ 2.841 #/m^2 in control experiments, 29.09 $\pm$ 2.219 and 28.54 $\pm$ 5.038 #/m^2 after 6 hours of TNF-a stimulation; 40.37 $\pm$ 9.205 and 40.26 $\pm$ 3.521 #/m^2 after 12 hours of TNF-a stimulation. At Q = 100 nL/min, the normalized number of adhering HCT-15 and MDA-MB-231 cells was, respectively, 6.698 $\pm$ 1.452 and 7.30 $\pm$ 1.088 #/m^2 in control experiments, 11.87 $\pm$ 0.899 and 13.78 $\pm$ 1.716 #/m^2 after 6 hours of TNF-a stimulation; 34.05 $\pm$ 1.427 and 26.69 $\pm$ 2.780 #/m^2 after 12 hours of TNF-a stimulation.

As compared to the healthy vasculature, cancer cells adhered 2 and 3-times more avidly to a 6h- and 12h-inflamed endothelium. Maximum cell adhesion is observed under static conditions (Q = 0,

Figure.3.1c), followed by Q = 50 and 100 nL/min. Thus, as expected, the number of adhering cells reduces as the flow rate increases. Indeed, this is related to the corresponding increase of the hydrodynamic dislodging forces that would decrease the likelihood of firm CTC adhesion on HUVECs.

Cancer cell rolling on inflamed endothelial cells under dynamic conditions. A subset of circulating tumor cells was observed to interact with the endothelial monolayer without firmly adhering but rather rolling steadily. The cancer cells exposed to a dynamic conditions are transported within the microfluidic chip at two different flow rates (50 and 100 nL/min). The solution is injected into the microfluidic chip using a syringe pump for 15 minutes Thus, the rolling velocity u_{roll} of tumor cells was quantified by monitoring the displacement of the cell centroid over time. By imaging post-processing, u_{roll} of the metastatic colon (HCT-15) and breast (MDA-MB-231) cancer cells was quantified at 50 and 100 nL/min, and under different HUVEC conditions, namely unstimulated HUVECs (- TNF-α), 6h-stimulated HUVECs (+TNF-α 6h), and 12h-stimulated HUVECs (+TNF-α 12h). Data are charted in **Figure.3.5a** and **b**, respectively, for 50 and 100 nL/min. At 50 nL/min, the rolling velocity of HCT-15 cells was of 113.9 ± 4.132, 103.4 ± 2.880 and 98.00 ± 4.552 µm/sec for unstimulated HUVECs (- TNF-α), 6h-stimulated HUVECs (+TNF-α 6h), and 12h-stimulated HUVECs (+TNF-α 12h), respectively. Under the same conditions, for the MDA-MB-231, the rolling velocities were 118.6 ± 1.349 µm/sec 105.68 ± 3.340 µm/sec 102.1 ± 5.288 µm/sec (**Figure.3.5a**). Even in the case of rolling velocities, no statistically significant difference was observed between the two cell lines. A 10% and 20% statistically significant decrease in rolling velocities between the control groups and the 6 and 12 hours TNF-α stimulated groups was observed. Under TNF-α stimulation, endothelial cells express a larger number of adhesion molecules, which would reduce the rolling velocity and favor the firm deposition of CTCs. Note that, this is in agreement with what was documented by Navarro and collaborators [154] in the case of polymorphonuclear (PMNCs) and peripheral blood mononuclear (PBMCs) cells.

As expected, the rolling velocity slightly but steadily decreased as the level of TNF-α stimulation increased. At 100 nL/min, the rolling velocities for the HCT-15 cells were 163.6 ± 20.10 µm/sec (-TNF-α), 157.4 ± 4.531 µm/sec (TNF-α 6h) and 158.06 ± 1.187 µm/sec (TNF-α 12h). For the MDA-MB-231, the same physical quantity took the values 170.9 ± 11.03 µm/sec (-TNF-α); 151.8 ± 8.182 µm/sec (6h TNF-α) and 144.9 ± 1.500 µm/sec (12h TNF-α).

Lastly, the ratio between the number of rolling and adhering cells was plotted for two different flow conditions (**Figure.3.5c** and **d**). For unstimulated HUVECs, most of the circulating tumor cells were observed to steadily roll over the endothelium monolayer, whereas the ratio decreases as the TNF-α stimulation increases. At low flow rates (Q = 50 nL/min), the ratio for the HCT-15 cells was 0.845 ± 0.084 (-TNF-α); 0.713 ± 0.122 (TNF-α 6h) and 0.553 ± 0.096 (TNF-α 12h). Very similar are the ratios quantified for the MDA-MB-231, for which it resulted 0.828 ± 0.067 (- TNF-α), 0.669 ± 0.034 (TNF-α 6h) and 0.597 ± 0.030 (TNF-α 12h). At high flow rates (Q = 100 nL/min), the ratio for the HCT-15 cells was 0.875 ± 0.020 (- TNF-α), 0.728 ± 0.038 (TNF-α 6h) and 0.591 ± 0.017 (TNF-α 12h). Similarly, for the MDA-MB-231, the ratio was 0.850 ± 0.061 (- TNF-α), 0.715 ± 0.015 (TNF-α 6h) and 0.651 ± 0.063 (TNF-α 12h). As reported before for other physical quantities, also in this case, no statistically significant difference was determined between the two cell lines.
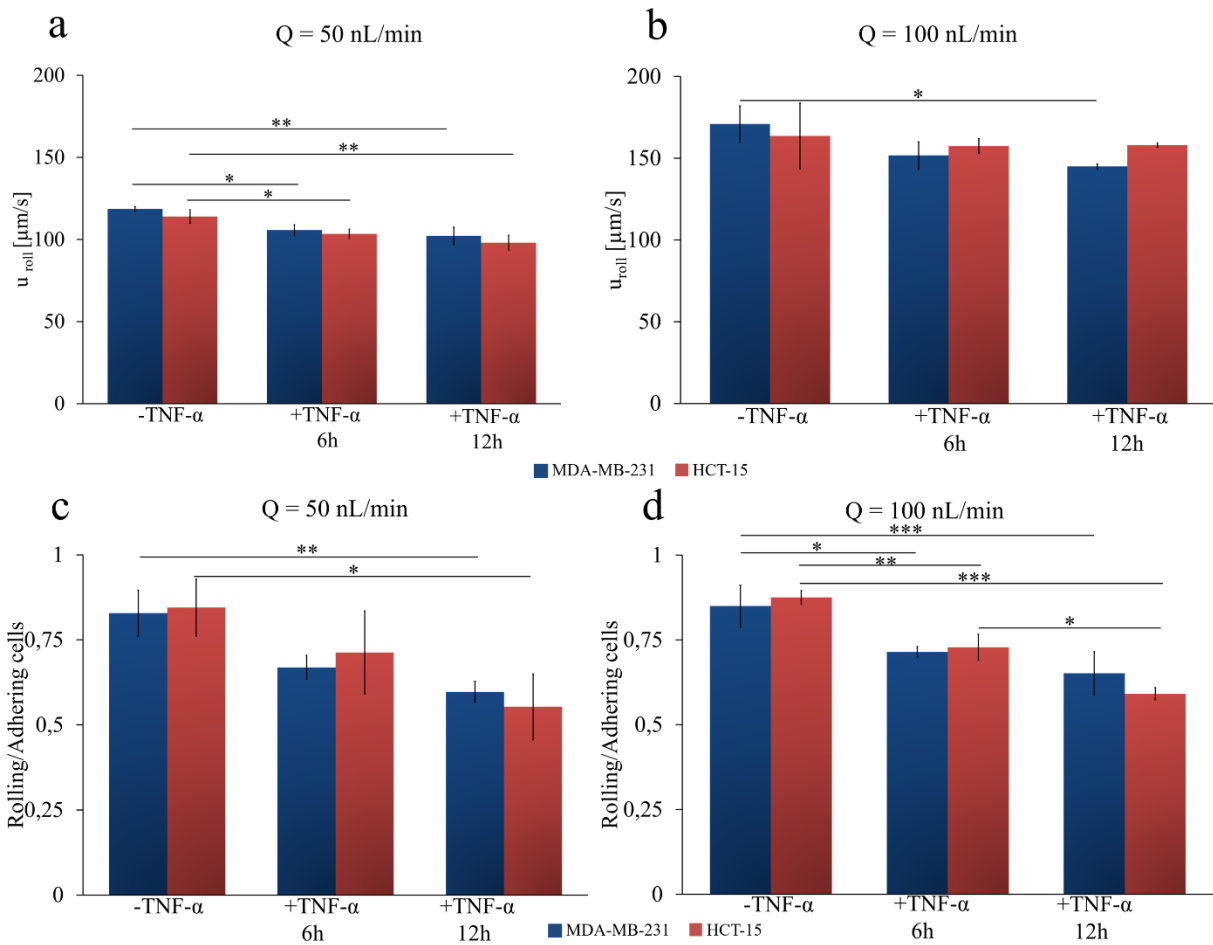
Figure 3.5. Cancer cell rolling on inflamed endothelial cells under dynamic conditions. (.a,.b) Rolling velocity of colon cancer HCT-15 (red column) and breast cancer MDA-MB-231 (blue column) at 50 nL/min and 100 nL/min on a confluent layer of HUVEC. (**.c, .d**) Ratio between the number of rolling and adhering cancer cells (HCT-15 - red column; breast cancer MDA-MB-231 - blue column) on a confluent layer of HUVEC at 50 nL/min and 100 nL/min. HUVECs are not stimulated with TNF-α (-TNF-α) or stimulated with 25 ng/mL of TNF-α for 6h (+TNF-α 6h) or 12h (+TNF-α 12h). (Data are plotted as mean $\pm$ SD. n = 3. Statistical analysis ANOVA. * symbol denotes statistically significant difference p<0.01; ** symbol denotes statistically significant difference p<0.001; *** symbol denotes statistically significant difference p<0.0001).

Cancer cell adhesion on inflamed endothelial cells under whole blood flow. Leukocyte recruitment at inflamed tissues has a number of similarities with the colonization at distant sites of CTCs. In particular, just like for leukocytes, CTCs tend to transiently interact with the blood vessel

walls engaging specific receptor molecules, then adhere and spread over the endothelial cells and, eventually, cross the vascular barrier relocating in the extravascular space. Adhesion molecules are over-expressed in postcapillary venules during an inflammatory process.[155-157]. Moreover, it is well recognized that leukocyte rolling and adhesion on the inflamed vascular endothelium is modulated by the presence of red blood cells (RBCs). Specifically, experimental observation and simulations have shown that the deformability and shape of RBCs allow them to concentrate within the core of blood vessels leaving a so-called 'cell free layer' next to the vessel walls.[158-161] Leukocytes, which are two-times larger and far less abundant than RBCs, tend to be pushed laterally in the cell free layer by the fast moving RBCs. This process, known as 'margination', should also affect the vascular behavior of CTCs.

In this section, cancer cell rolling and adhesion over a monolayer of HUVECs is analyzed in the presence of whole blood. The single-channel microfluidic chip was again covered by a confluent monolayer of HUVECs, which were unstimulated or stimulated with TNF-α (12h only), and cancer cells re-suspended in whole blood were directly injected at two different flow rates (Q = 50 and 100 nL/min). Whole blood, freshly drawn from rats, contained all the cell and molecular components of blood, including red blood cells, platelets, leucocytes and plasma proteins which may all contribute, at different extents, to cancer cell rolling and adhesion.[126-127] A fixed hematocrit of 40% was considered. Results for eight different working conditions are provided in **Figure.3.6b** and **d**, which are for Q = 50 and 100 nL/min, respectively. As previously, breast cancer cells are identified by blue bars whereas colon cancer cells are associated with red bars. On the left hand side (**Figure.6a** and **c**), representative fluorescent microscopy images are shown for unstimulated HUVECs (- TNF-α), and 12h-stimulated HUVECs (+TNF-α 12h). The results unequivocally showed that blood cells favor the adhesion of circulating tumor cells to the vascular walls, especially in the case of unstimulated endothelium. In **Figure.3.6b** and **d**, the normalized number of adhering cells is reported. At Q = 50 nL/min, the normalized number of adhering HCT-15 and MDA-MB-231 cells was 25.33 ± 4.762 and

18.19 ± 1.269 #/m^2 in control experiments, 35.68 ± 10.99 and 46.96 ± 13.18 #/m^2 after 12 hours of TNF-a stimulation, respectively. At Q =100 nL/min, the normalized number of adhering HCT-15 and MDA-MB-231 cells was 26.04 ± 9.90 and 17.59 ± 6.129 #/m^2 in control experiments, 30.12 ± 4.011 and 23.04 ± 4.406 #/m^2 after 12 hours of TNF-α stimulation, respectively. Notably, even under these conditions, no statistically significant difference in cell adhesion was detected between breast and colon cancer cells. Interestingly, a statically significant difference was measured only between untreated and TNF-α treated endothelial cells at the lowest flow rate (Q = 50 nL/min, in **Figure.3.6b**). At highest flow rates, the absolute number of adhering cells reduces and twelve hours TNF-α stimulation is insufficient to induce a statistically significant increase in cell deposition.

A direct comparison in terms of CTC vascular adhesion between whole blood flow and physiological solution is now needed. **Figure.3.6e** and **f** collect all the data required for this comparison. Within an unstimulated microvascular network, the presence of blood cells does dramatically increase CTC adhesion (**Figure3..6e**). For Q = 50 nL/min, the density of firmly adhering CTCs grows from about 10 to 20 #/m^2 moving from physiological solution to whole blood flow. A slightly larger increase is observed for Q = 100 nL/min. Differently, within an inflamed microvascular network, the presence of blood cells does not significantly affect CTC adhesion (**Figure.3.6f**). The density of firmly adhering CTCs is around 40 #/m^2 at 50 nL/min and reduces to about 30 #/m^2 at 100 nL/min, with and without RBCs. This could be interpreted as, under the current conditions, the density of adhering CTCs on the inflamed endothelium has reached saturation and the presence of RBCs cannot further foster cell deposition. Also, RBC-CTC collisions could limit any further increase in cell deposition. Indeed, additional experiments would be needed to support this hypothesis. Interestingly, a direct comparison of the data presented in **Figure.3.6e** and **f** would lead one to infer that, at higher flow rates (100 nL/min), the density of firmly adhering CTCs on the inflamed and normal vasculature is comparable when a whole blood flow is considered. Again, this could be due to a balance between

shear stresses and cell-cell collisions. Indeed, this is not observed at low flow rates (50 nL/min), where adhesion is higher on inflamed endothelium.
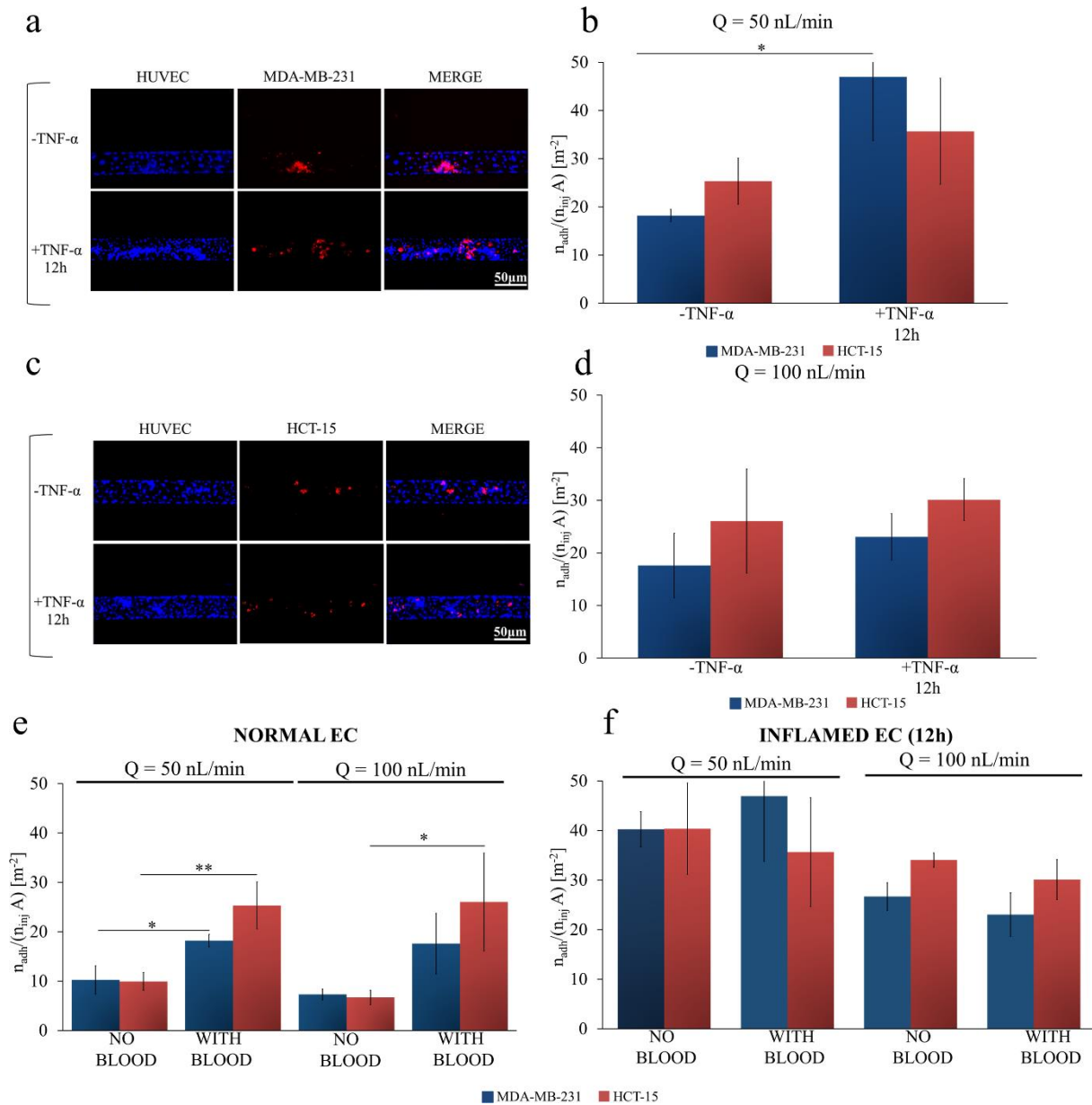

Figure 3.6. Cancer cell adhesion on inflamed endothelial cells under whole blood flow. a. Representative fluorescence microscopy images of breast cancer cells MDA-MB-231 (cell membrane labeled in red with CM-DIL) flowing in whole blood and interacting, in a single-channel microfluidic chip, with a confluent monolayer of HUVECs (cell nuclei stained in blue with DAPI). **b.** Normalized number of adhering cancer cells on a HUVEC monolayer of colon cancer HCT-15 (red column) and breast cancer MDA-MB-231 (blue column) at a flow rate (50 nL/min), with and without stimulation with TNF-α (25ng/mL) in the presence of whole blood

(hematocrit: 40%). **c.** Representative fluorescence microscopy images of colon cancer cells HCT-15 (cell membrane labeled in red with CM-DIL) flowing in whole blood interacting, in a single-channel microfluidic chip, with a confluent monolayer of HUVECs (cell nuclei stained in blue with DAPI). **d.** Normalized number of adhering cancer cells on a HUVEC monolayer of colon cancer HCT-15 (red column) and breast cancer MDA-MB-231 (blue column) at high flow rate (100 nL/min), with and without stimulation with TNF-α (25ng/mL) in the presence of whole blood (hematocrit: 40%). (**e., f.**) Normalized number of adhering colon cancer HCT-15 (red column) and breast cancer MDA-MB-231 (blue column) on a HUVEC monolayer, without (**f.**) and with (**e.**) stimulation of TNF-α (25ng/mL) for 12h at a flow rate of 50 nL/min and 100 nL/min, with and without whole blood (hematocrit: 40%). (Data are plotted as mean $\pm$ SD. n = 3. Statistical analysis ANOVA: * symbol denotes statistically significant difference $p < 0.05$; ** symbol denotes statistically significant difference $p < 0.01$ ($n_{inj} = 10^6$ cells and $A = 1.22 \square 10^{-6}$ m^2)).

This data confirms that blood cells facilitate the vascular adhesion of CTCs, just like for leukocytes, and open up to the following two considerations: CTCs would tend to adhere throughout the microvasculature, on both inflamed and not inflamed endothelial cells, thus increasing the likelihood of finding proper conditions for colonization; in microfluidic experiments, neglecting the role of blood cells could dramatically underestimate the adhesion propensity of CTCs.

Predicting cancer cell adhesion and rolling on inflamed endothelial cells. In order to predict CTC vascular behavior under different flow and adhesion conditions, a computational model was employed based on previous works by the authors.[145, 162-163] In this model, cancer cells were considered as rigid and deformable circular objects exposed to a Poiseuille flow and capable of interacting with vascular walls (endothelial cells) via specific ligand-receptor bonds (**Figure.3.7a**). Simulations were performed in a rectangular computational domain, with height H (= 42 µm) and length 10H, resembling the longitudinal cross section of the single channel in the microfluidic chip.
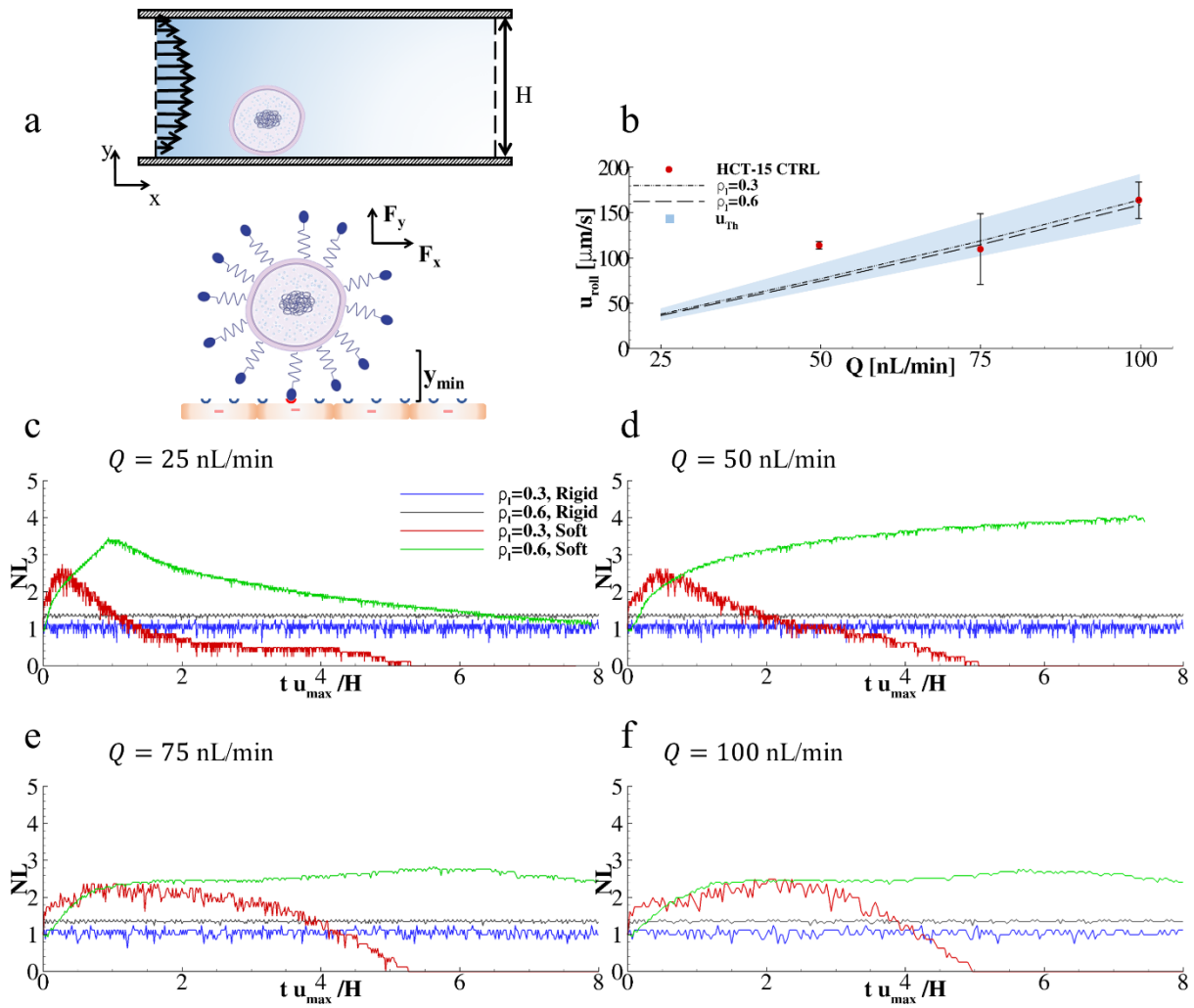
Figure 3.7. Predicting cancer cell adhesion and rolling on inflamed endothelial cells. **a.** Schematic diagram presenting the computational problem with a close-up depicting ligand-receptor interactions at the interface between cancer (up) and endothelial (lower) cells. **b.** Rolling velocities of cancer cells under four different flow rates (Q = 25, 50, 75, and 100 nL/min) and two ligand-receptor bond concentrations (ρ_l = 0.3 and 0.6). (Solid lines are simulated values; Dots are experimental values; dashed lines are theoretical values). **c, d, e, f.** Variation of the number of active ligand-receptor bonds over time, under four different flow rates (Q = 25, 50, 75, and 100 nL/min), two ligand-receptor bond concentrations (ρ_l = 0.3 and 0.6), and for soft and rigid cancer cells. Nl is the number of closed bonds in each time step. This number is computed as the ratio between the current number of closed bonds over the number of closed bonds in the initial configuration."

The diameter of cancer cells was fixed to d= 15 µm, as quantified via bright field microscopy (**Figure.3.8**). The ratio between the number of ligands decorating the surface of cancer cells and the number of receptors expressed on the endothelium is ρ_l. Two different ratios ρ_l were considered, namely 0.3 and 0.6. These assumed ligand densities return a good agreement between the experimental and numerical predictions for the cell rolling velocity over three different flow rates.
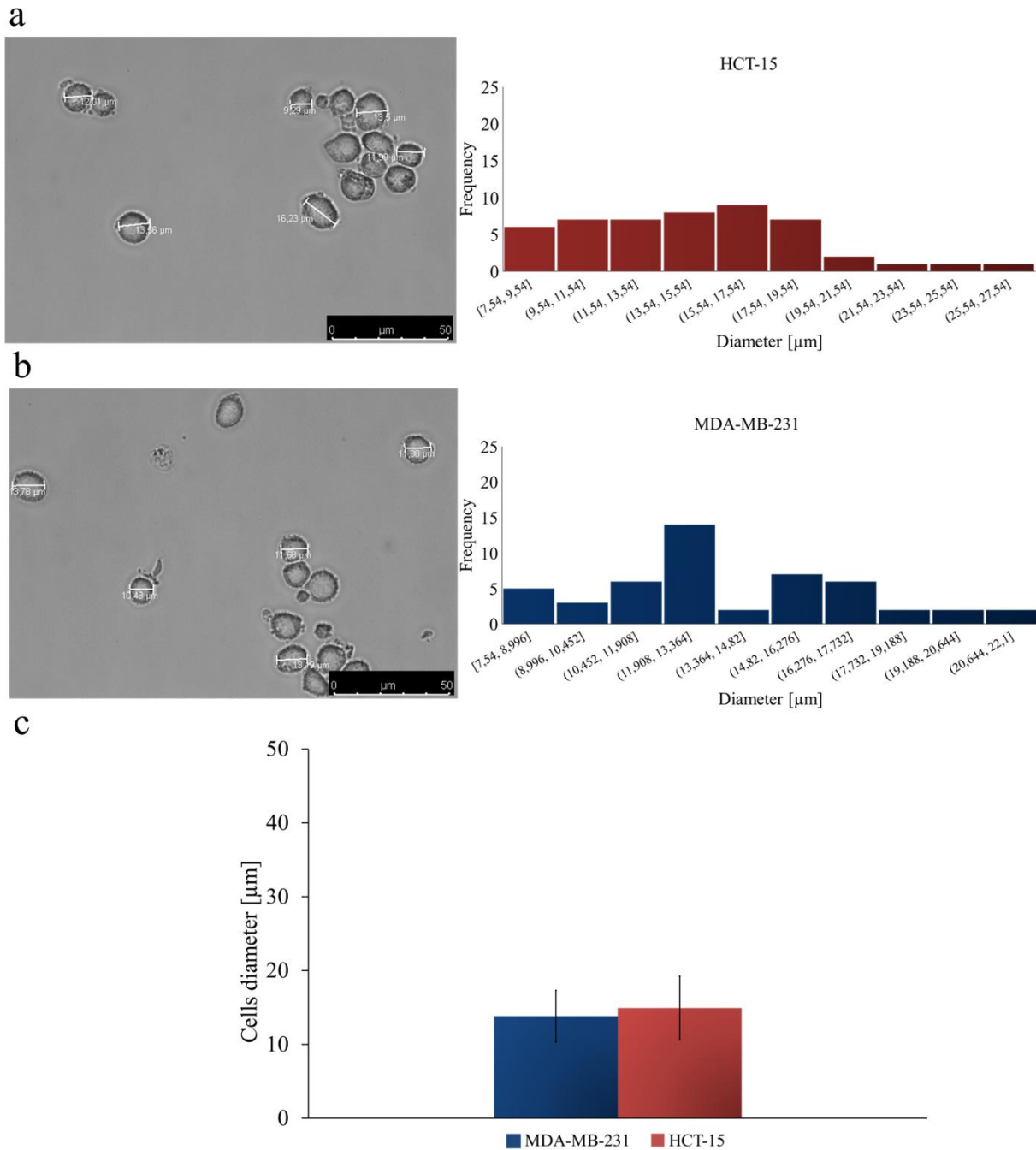

Figure 3.8.Cancer cell diameter of colon cancer HCT-15 (red column) and breast cancer MDA-MB-231 (blue column). a. Representative microscopy images of HCT-15 cells (left) along with the counted diameter

frequency (right). **b.** Representative microscopy images of MDA-MB-231 cells (left) along with the counted diameter frequency (right). Scale bar of 50 µm. **c**. Average diameters for colon cancer HCT-15 (red column) and breast cancer MDA-MB-231 (blue column). Data are plotted as mean $\pm$ SD.

At first, cancer cells were assumed to be rigid, which is indeed the simplest possible hypothesis. Then, simulations were performed for estimating the rolling velocities of cancer cells over the vascular wall as a function of four different flow rates, namely Q = 25, 50, 75, and 100 nL/min; and two ρ_l ratios, namely 0.3 and 0.6. The resulting data are shown in **Figure.3.7b** (lines) where a direct comparison with the corresponding experimental data is also included (blue dots for HCT-15 cells). From the simulations, the cell rolling velocity was predicted to grow quasi-linearly with the flow rate Q (R^2 = 0.998 and 0.994 for ρ_l = 0.3 and 0.6, respectively) and slightly decrease with an increase in ρ_l = 0.3. Overall, the predicted rolling velocities were found to be in good agreement with the experimental data for Q = 100 nL/min, returning a relative error smaller than 0.74% and 3.10% for ρ_l = 0.3 and 0.6, respectively. A larger difference was observed at low flow rates, Q = 50 nL/min, where the relative error increased to about 43.01% and 52.07% for ρ_l = 0.3 and 0.6, respectively. This might be due to the fact that this flow rate is very close to the lower limit for the syringe pump used in the experiments. Note that an increase in ρ_l from 0.3 to 0.6 was associated with only a 3.5% decrease in rolling velocity. This is also in agreement with the experimental data of **Figure.3.5a** and **b** documenting a modest variation in u_{roll} with vascular inflammation.

Although the 'rigid cell' approximation quite accurately modeled the rolling behavior of cancer cells, it could not predict their firm vascular adhesion. Therefore, in a second set of simulations, the cancer cell was considered as a deformable capsule characterized by the dimensionless capillary number Ca = 10^{-2}. These data are plotted in **Figures.3.7c** and **f** for four different flow rates (Q = 25, 50, 75, and 100 nL/min); two ligand-receptor densities (ρ_l=0.3 and 0.6). Also, a direct comparison between rigid and soft cells is provided. Soft cells exhibited more complex vascular adhesion patterns. For ρ_l=0.3, soft cells were observed to establish an initial adhesive contact with the endothelial surface resulting

in partial cell deformation and increase in the number of ligand-receptor bonds. However, after reaching a maximum, the adhesive interactions were not sufficient to counteract the dislodging hydrodynamic forces and, consequently, the number of close bonds reduced tending eventually to zero. For ρ_l=0.6, a larger number of ligand-receptor bonds could be formed leading to stronger adhesive interactions. This is indeed observed in the plots of **Figure.3.7c** and **f**. Also, for sufficiently high flow rates (Q ≥ 50 nL/min), partially adhering soft cells were deformed and pushed down to the wall thus maximizing their adhesive surface and interface forces and leading to a 2 to 3-times higher number of ligand-receptor bonds as compared to the corresponding rigid cell cases (**Figure.3.7e** and **f**). Notably, simulations predicted that rigid cells would roll over the endothelium with a rolling velocity decreasing with an increasing surface density of ligands (black and blue lines in **Figure.3.7c** and **f**). Differently, deformable cells would, for low ligand surface densities, transiently adhere, detach and move away from the wall pushed by hydrodynamic lift forces (red lines in **Figure.3.7c** and **f**); whereas, for high ligand surface densities, deformable cells would firmly adhere, deform under flow and increase the surface of adhesion as documented by the growth of the number of the engaged ligand-receptor bonds. (green lines in **Figure.3.7c** and **f** and **Figure.3.9**). Although the present simulations can quite accurately predict the rolling velocities of circulating cancer cells, it should be emphasized that only a fully 3D model, including deformable RBCs and CTCs, could realistically predict the vascular behavior of cancer cells.[164-165]

a

Rigid cell with $\rho_l = 0.3$

b

Soft cell with $\rho_l = 0.3$

c

Soft cell with $\rho_l = 0.6$
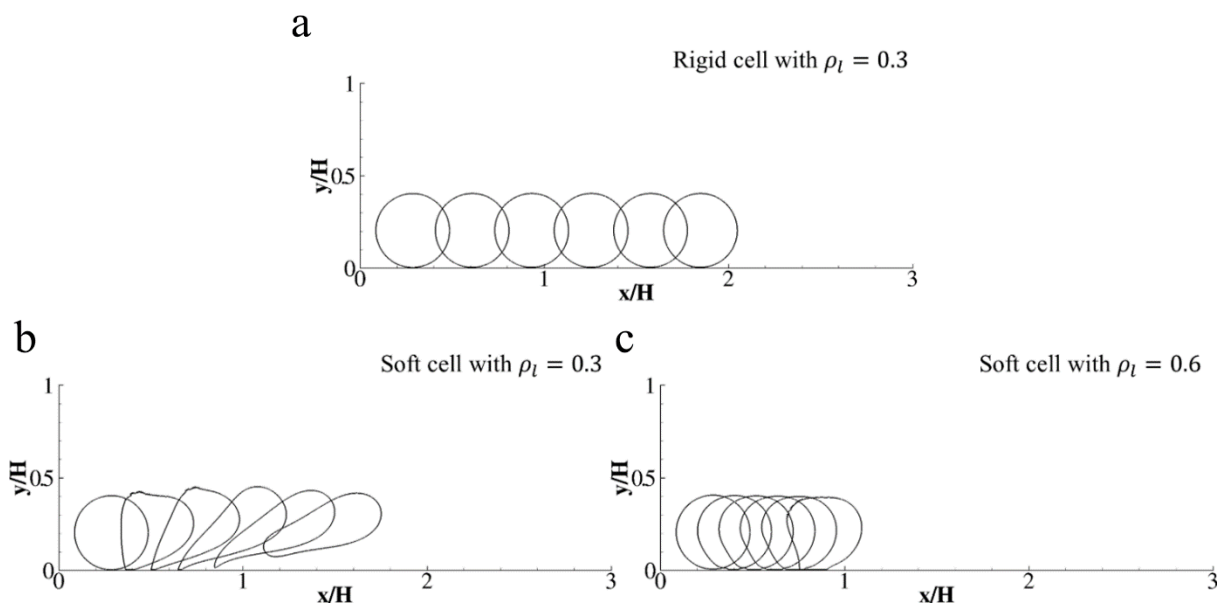
Figure 3.9. Soft and rigid cells interacting with the endothelial wall at Q=25nL/min. a. Configurations of a rigid cell rolling on the vascular wall decorated with $\rho_l = 0.3$ for different time points, tu_{max}/H=0.0, 1.5, 3.0, 4.5, 6.0, and 7.5. **b, c.** Configurations of a soft cell interacting with the vascular wall decorated with $\rho_l = 0.3$ and $\rho_l = 0.6$ for different time points, tu_{max}/H=0.0, 1.5, 3.0, 4.5, 6.0, and 7.5.

3.5 CONCLUSIONS

A microfluidic chip was used to analyze the vascular transport of circulating tumor cells under different biophysical conditions. The surface density of adhering cells and the velocity of rolling cells were quantitatively characterized over a confluent endothelial monolayer as a function of the level of inflammation (no TNF-α; TNF-α stimulation for 6h; TNF-α stimulation for 12h); flow rate (50 and 100 nL/min); and working fluid (physiological solution and whole blood, at 40% hematocrit). Two different types of cancer cells – colorectal HCT-15 and breast cancer MDA-MB-231 cells – were considered.

It was confirmed that vascular inflammation facilitates cell adhesion in a way proportional to TNF-α stimulation, whereas high flow rates are associated with lower cell deposition. Rolling velocities are only slightly affected by vascular inflammation and grow proportionally with the flow rate. As compared to a physiological solution, flowing cancer cells in whole blood enhances their firm deposition on healthy endothelium rather than on the inflamed vasculature, for all tested conditions. No statistically significant difference is observed for adhesion and rolling between HCT-15 and MDA-MB-231 cells.

These results would imply that neglecting the contribution of whole blood in the analysis of cancer cell dynamics can significantly underestimate their vascular deposition. Furthermore, it can be concluded that whole blood flow supports cancer cell deposition and facilitates metastatization over the entire microvasculature.

4. *Two-Channel Compartmentalized Microfluidic Chip for Real-Time Monitoring of the Metastatic Cascade*

4.1 INTRODUCTION

It is well accepted that metastases and disease recurrence are the main causes of death in cancer patients.[166] The ability of malignant cells to enter the blood stream, abandoning the primary tumor mass; disseminate through the vascular network, searching for a new homing tissue; adhere to the vascular walls, resisting hemodynamic forces; extravasate at a distant site, opening the endothelial barrier; and, eventually, migrate away from the blood vessels, infiltrating a new tissue; is crucial in the formation of metastatic niches[115, 167-168]. This stepwise sequence of events is regulated by a multitude of biophysical and biochemical processes, including alterations of cell polarity, cytoskeletal and nuclear architecture, and expression of membrane receptors. For instance, the intravasation of tumor cells is supported by the well-known epithelial-to-mesenchymal transition (EMT), which involves the disruption of intercellular adhesion, cell polarity and the overexpression of specific cell-matrix adhesion molecules.[2, 169] Inside the vascular network, tumor cells, which are then called circulating tumor cells (CTCs), can interact and cluster with blood cells, such as platelets, to elude immune surveillance and enhance longevity in the blood stream. Also, CTCs can interact with the vascular walls establishing transient and firm adhesion events with the endothelial cells, mimicking what leukocytes do at sites of inflammation[168]. The small fraction of tumor cells surviving the vascular environment can progressively infiltrate the new homing tissue and modify the local microenvironment to create suitable conditions for engraftment and proliferation. Although the mechanisms are yet to be fully elucidated, establishing metastatic niches is not a random process but is affected by the local microenvironment, vascular architecture as well as by the type and location

of the original malignant mass.[1, 170-173]

Different microscopy techniques, including conventional confocal fluorescent microscopy and intravital video microscopy, have been employed to monitor the fate of individual cancer cells and the progressive formation of metastatic niches. In this context, non-mammalian model organisms, such as zebrafishes and drosophilas, and small rodents, such as mice and rats, have been used to recapitulate the metastatic evolution of different tumor types.[174-175] Non-mammalian model organisms allow conventional confocal microscopy to follow in vivo the dynamics of individual CTCs. Also, through genetic modification, these models can be efficiently used to test specific biological hypotheses. For instance, drosophilas and zebrafishes have been used to elegantly reveal the pivotal role of matrix metalloproteinase secretion and tumor microenvironment in supporting cancer cell migration and spreading to distant organs.[176-178] Although more demanding in terms of equipment and animal handling, intravital microscopy techniques have been developed by multiple laboratories to observe the vascular dynamics of CTCs and tissue infiltration in real time. For instance, Winkler and collaborators focused on the formation of brain metastases by observing the evolution of individual CTCs over a time window ranging from minutes to months.[120, 179] The group of Robert Hoffman has developed preclinical models of cancer metastasis, optical probes and microscopy techniques for assessing single cancer cell dynamics in different organs, including the lungs[180], pancreas[181] and prostate.[182] Solid protocols have been also developed to image the formation and evolution of clusters of CTCs.[183] Although animal models offer a more authentic representation of the key biophysical and biochemical features regulating cancer metastases, it is difficult to control, accurately and independently, the many governing parameters. For this reason, systematic analyses on the temporal and spatial evolution of CTCs can be efficiently performed solely using in vitro assays.

Cell migration across biological barriers has been traditionally studied using a Boyden chamber assay, which was originally employed for mimicking leukocyte chemotaxis and, then, applied to study tumor cell invasion.[184] In this system, a porous membrane separates two different compartments, which

contain the cells and media of interest. Despite its simplicity, the Boyden chamber assay does not allow one to monitor in real time cell migration from one chamber to the other, given the difference in focal planes; and, more importantly, cannot support fluid flow, which affects cell dynamics, cytoskeletal architecture and receptor expression. In order to address these limitations, microfluidic-based assays have been developed over the last few years with diverse applications. For instance, cell infiltration was studied by Chaw and colleagues, who fabricated a multi-step microfluidic device where cells are forced to squeeze within tiny and long orifices filled with extracellular matrices.[185] A similar approach was also employed by others to study cancer cell migration under chemical gradients and electric fields.[186] The group of Roger Kamm realized a microfluidic platform comprising a central and two lateral channels, separated by an intermediate chamber, to study cancer cell migration, invasion and extravasation.[136, 187-189] Other groups mostly focused on CTC adhesion to endothelial cells under flow, upon stimulation by specific chemokines and pro-inflammatory molecules.[139, 190] Yet, an experimental set-up for reproducing the entire series of events in the metastatic cascade is missing.

For this research project, a compartmentalized microfluidic device is proposed, which comprises two micro-channels running in parallel and connected by a micro-membrane realized in the lateral walls (**Figure.4.1**). Differently from a Boyden chamber, the device allows one to monitor simultaneously the dynamics of cells within the two different compartments and across the micro-membrane. This is microfabricated to include a series of pillars forming openings smaller than 3 μm, which separate the two channels into two different compartments. Endothelial cells are deposited in the vascular compartment forming a confluent layer over the micro-membrane, whereas an extracellular matrix enriched with different cell types is deposited within the tissue compartment. The device can be used for studying cell intravasation, vascular circulation and adhesion, extravasation and infiltration, thus covering in full the metastatic cascade.

4.2 MATERIAL AND METHODS

Fabrication of the double microfluidic chip

A silicon (Si) wafer (4"- P doped - <100> - $10 \div 20$ Ω/cm^2 – 525 µm thick, from Si-Mat) was used for the fabrication of the master template. A 60 nm thick layer of (Cr 99.95%, Kurt J. Lesker Company) was evaporated onto the silicon wafer and used as mask. AZ5214E (Microchem) was used as a resist and the solvent AZ726MF (Microchem) as a developer. The impressed pattern was transferred from the resist to the chromium mask by using a commercial Cr etchant (Chrome etch 18, OSC OrganoSpezialChemie GmbH). Before the replica process with polydimethylsiloxane (PDMS), an anti-stiction layer of 1H,1H,2H,2H-Perfluoro-octyl-trichloro-silane (125ul, Alfa Aesar) was deposited by vapor phase on the silicon template. PDMS replicas were produced by using a pre-polymer solution of Sylgard 182 (Dow Corning). Biopsy punches (OD = 1 mm, Miltex) were used to create fluidic ports in the reservoirs and glass coversheets (No. 1.5H, Deckaläser) were used to close the microstructures. The microfluidic chips were prepared according the protocol previously described by the authors [191]. Briefly, the negative pattern of the chip was transferred onto a silicon wafer by using optical lithography and Inductive Coupled Plasma-Reactive Ions Etching (SI 500, SENTECH Instruments GmbH). Since the etching rate of the ICP–RIE process is aspect-ratio dependent, a double lithographic step was used to obtain homogeneous microstructures. First, the micro-pillars were etched of few microns; second, micro-pillars with channels and reservoirs were further excavated to reach a depth of 50 µm. PDMS replicas were produced by using a base and curing agent mixing with a ratio (w/w) $10:1$. The solution was casted on the silicon template and baked in an oven at 60 °C overnight for 15 h. PDMS replicas underwent an oxygen (O_2) plasma treatment (Pressure = 0.5 mBar, Power = 20 W, Time = 20 s; Plasma System Tucano, Gambetti) and bonded to glass coversheets. The resulting microfluidic chip has a rectangular cross section with a width w= 210 µm, height h= 50 µm, and a port-to port length l= 2.7 cm as shown in **Figure.4.1a**. The pillars membrane has a length l=500 µm and a width w= 25 µm. Between each pillar there is a gap

of about 3 μm.

Electron microscopy imaging

Microfluidic chips were analyzed by Scanning Electron Microscope (JSM-6490LV, JEOL and Helios Nanolab 650, FEI Company™). SEM images were acquired after cutting the chip bonded on the glass slide with a blade, then cells were fixed with 0.2% of Glutaraldehyde in cacodylate 0.1 M buffer solution and dried with ethanol solution. The PDMS was pretreat with 15 nm of gold and then imaged by secondary electrons imaging (SEI) mode. Low magnification and high magnification SEM images were obtained with accelerating voltage of 15 and 5 kV, respectively.

Permeability experiments in the microfluidic chip

Microfluidic chips were autoclaved at 120 °C for sterilization. Then they were dried to remove the water from channels and placed in an incubator overnight (37 °C, humidity > 95%). Matrigel 8-12 mg/mL was put in ice to maintain the solution in liquid form (Sigma Aldrich), then it was mixed with Eagle's minimum essential medium (EMEM) (ATCC©, USA) to yield a final matrix concentration of 4-6 mg/mL. Afterwards, the matrigel matrix was introduced in the extravascular channel and gelation occurred in 5 minutes at 37 °C. 50 ng/mL of TNF-α were introduced in the matrigel to induce a gradual release of the pro-inflammatory molecule from the extravascular to the vascular compartment. Next, the vascular channel was filled with 20 μg/mL of fibronectin solution (Sigma Aldrich) and incubated for 1h at 37°C. Human Umbilical Vein Endothelial Cells (HUVEC) were cultured in endothelial growth medium according to the manufacturer's guidelines (cells and culture media were purchased from PromoCell, USA). Before seeding into the microfluidic chip, HUVECs were cultured, washed, detached, counted and concentrated at $6x10^6$ cell/mL. Cells were used up to passage 6 (P6). For both the vascular and the extravascular compartments, micropipette tips were filled with 200 μm of culture media on the inlet side, whereas the tips on the left side were left empty.

Media was changed every day. Routinely, chips were used 2 days after seeding.

The vascular channel was connected to a syringe pump (Harvard Pump 11 Elite, Harvard Apparatus) by a polyethylene tubing (BTPE-50, Instech). During the permeability tests, 40 kDa FITC-Dextran (Sigma Aldrich) was added up to a concentration of 0.5 µg/mL. For all the experiments, solutions were flowed at a physiological shear strain, $\sigma = 20$ s^{-1}, that corresponds to a flow rate of 100 nL/min. Dextran permeability was detected using a fluorescent inverted microscope (Leica 6000). The analysis of Dextran permeability was done by ImageJ software using two ROIs, one fixed in the vascular channel and the other in the extravascular channel. The formula is reported in **Figure.2b**. Briefly, the equation $P = \frac{(I_f - I_i)w}{(I_i - Ib)\Delta t}$ was used, where P is the diffusive permeability (µm/s), I_f is the total fluorescent intensity in the two ROIs at the final analyzed frame, I_i is the total fluorescent intensity in the two ROIs at the initial analyzed frame. I_b is the total fluorescent intensity in the extravascular ROI at the initial analyzed frame. ΔT is the time difference between the analyzed frame, and w is the width of the vascular channel.

Cancer cell intravasation model

MDA-MB-231 cells were used at 1.5×10^7 cell/mL embedded in the matrigel solution and introduced in the extravascular channel. After the gellification of the matrigel, the vascular channel was filled with 20 µg/mL of fibronectin solution and incubated for 1h at 37°C. Then HUVECs were inserted at 6×10^6 cells/mL. Cancer cells were imaged a 3, 6, 21, 24 and 30h using a fluorescent microscope (Leica, objective 10x). Any cancer cell with its full body in the vascular compartment was considered an intravasated cell. Time-lapse movies were acquired for the whole duration of the experiment, while the syringe pump was flowing media into the vascular compartment at Q= 50 nL/min.

Cancer cell transport and adhesion under flow model

After sterilization, microfluidic chips were dried and placed in incubator. The vascular channel was filled with 20 μg/mL of fibronectin solution and incubated for 1h at 37°C. Then HUVECs were inserted at $6x10^6$ cells/mL. Then the extravascular channel was filled with matrigel matrix and 50 ng/mL of TNF-α. After reaching cell confluency, the chip was placed on the stage of an epi-fluorescence inverted microscope for the adhesion experiments. The working fluid was injected into the chip using a syringe pump 33 Dual (Harvard apparatus). After the trypsinization, the cancer cells were incubated for 30 min with CM-DiI, at 37°C (0.5%, Thermofisher) according to the manufacture's protocol. Then, the cells were washed 3 times with PBS 1x (GIBCO) to remove the excess dye. Finally, the cells were re-suspended in the EMEM medium without FBS, that could interfere with the cell adhesion parameters, at $1x10^6$ cells/mL. After each rolling experiment, a washing with PBS was performed to remove the non-adherent cancer cells from the endothelium. Tumor cells were introduced via a syringe pump on the HUVEC monolayer The inlet port of the chip was connected to the syringe pump through a polyethylene tube (BTPE-60, Instech Laboratories). The interaction of tumor cells with HUVECs was recorded for 15 consecutive minutes for each experiment. Two flow rates Q were imposed via the syringe pump, namely, 50 and 100 nL/min. [192].

Cancer cell extravasation model

Vascular channel was filled with 20 μg/mL of fibronectin solution and incubated for 1h at 37°C, HUVECs were inserted at $6x10^6$ cells/mL. Extravascular channel was filled with a solution of matrigel, FITC-Dextran 4 kDa and TNF-α 100 μg/mL (final concentration). Then after reaching cell confluency, tumor cells MDA-MB-231 were infused on the endothelial cells by using syringe pump at flow rate of 50 nL/min for 15 minutes to permit the firm adhesion of cancer cells on the endothelium. The extravasated cancer cells were imaged at Leica microscope at 3, 6, 21, 24 and 30h.

Any cancer cell with its full body in the extravascular compartment was considered an extravasated cell. Time lapse movies were acquired for the whole duration of the experiment, while the syringe pump was flowing media into the vascular compartment at Q= 50 nL/min.

Cancer cell invasion model

Both microfluidic channels of the device were filled with a matrigel matrix, one was filled with $1.5x10^7$ MDA-MB-231 cancer cells and the other with FITC-Dextran 4 KDa and TNF-α 50 ng/mL (final concentration). The migrating cancer cells were imaged at Leica microscope at 3, 6, 21, 24 and 30h. Any cancer cell with its full body in the opposite compartment was considered a migrating cell. Time lapse movies were acquired for the whole duration of the experiment, while micropipettes tips were filled with 200 μl of cells growth media for both compartments.

Cell tracking

For the intravasation, extravasation and invasion processes there are fully movie during 30h (imaged every 4 minutes) of the cell movement acquired at NIKON center. During the experiments devices were kept under controlled conditions (5% CO_2 and 37°C), using an Oko lab Cage Incubation System mounted at time-lapse microscope. Movies were acquired for the whole duration of the flow (objective 20x). Cell dynamics were detected using time-lapse imaging equipped with an on-stage incubator (Eclipse Ti-E, Nikon) and A sCMOS camera (Andor Zyla) was used to acquire images and movies. The confocal fluorescent images into different channels were obtained using *Split- Channels* and recombining the images using *Merge Channels*.

Immunofluorescence staining and image acquisition

At the end of the experiments, both vascular and extravascular channels were carefully washed with PBS (Invitrogen) and fixed with 4% paraformaldehyde (PFA) (ChemCruz, Santa Cruz,

Biotechnologies, USA) for 15 minutes at room temperature. After washing twice with PBS, channels were filled with a 0.3% Triton X in PBS solution for 10 min at 4°C to allow cellular membrane permeation. Next, cells were incubated with 20% goat serum in PBS solution for 30 min at 4°C and then human endothelial Cadherins were targeted for 2 hours using anti-human VE-Cadherin antibody (Ms anti-human Ve-cadherin, 1:100, Abcam). Afterwards, devices were incubated with green fluorescent labeled secondary antibody (anti-mouse 488, 1:500, Abcam) for 50 min at 4 °C. Cell nuclei were stained with DAPI (5 mg/mL, Invitrogen) while F-Actin cytoskeleton filaments were stained in green by the use of phalloidin according to supplier (Alexa Fluor® phalloidin, life technologies). Images were acquired using confocal microscope (Nikon A1).

4.3 RESULTS AND DISCUSSION

The compartmentalized microfluidic device. A custom designed polydimethylsiloxane (PDMS) microfluidic device was used to reproduce the key steps in the metastatic process. The device consists of two parallel channels divided by a permeable membrane of rounded pillars (**Figure.4.1**). The channels present a total length of 2.7 cm (from inlet to outlet), a height of 50 µm and a width of 210 µm. The equivalent hydraulic diameter of the channels is comparable in size to large capillaries, arterioles and venules. The permeable membrane is placed in the center of the channels and is 500 µm long. The separation distance between the two channels, across the pillar membrane, is equal to~ 3 µm, which is sufficient to compartmentalize the two channels while still allowing molecules and cells to diffuse through. Therefore, the two compartments can be independently filled at the occurrence with different matrices (collagen, matrigel, hyaluronic acid, and combinations thereof) and cells (endothelial, cancer, stromal, immune cells and so on). In **Figure.4.1a,** a schematic of the microfluidic devices is presented together with electron microscopy images revealing the details of the micro-membrane. Specifically, the first electron micrograph shows the central portion of the device with the arrays of pillars constituting the micro-membrane. The second electron micrograph returns the shape and separation distance between adjacent pillars within the micro-membrane. These are slender structures, with an aspect ratio larger than 2.5, presenting a rounded shape to enhance lateral mechanical stability. In **Figure.4.1b,** two representative confocal fluorescent images document the compartmentalization of the device in two different channels. On the left, endothelial cells (HUVECs) confluently cover the upper, lower and lateral walls of the vascular channel (cell nuclei in blue – DAPI; VE-cadherin in green – FITC). On the right, breast cancer MDA-MB-231 cells populate a matrigel matrix deposited in the extravascular channel (cell membrane stained in red – CM-DiI). Notice that the endothelial cells adhere over the entire exposed surface in the vascular compartment allowing the formation of a pervious vessel with a tubular shape, whose permeability can be modulated at the micro-membrane. Additional details on the membrane and channels' cross

sections are provided by the electron micrographs of **Figure.4.1c**. In the right image, cells can be observed distributed within the channels, whereas the left image offers a detailed view of the micropillars in the membrane.
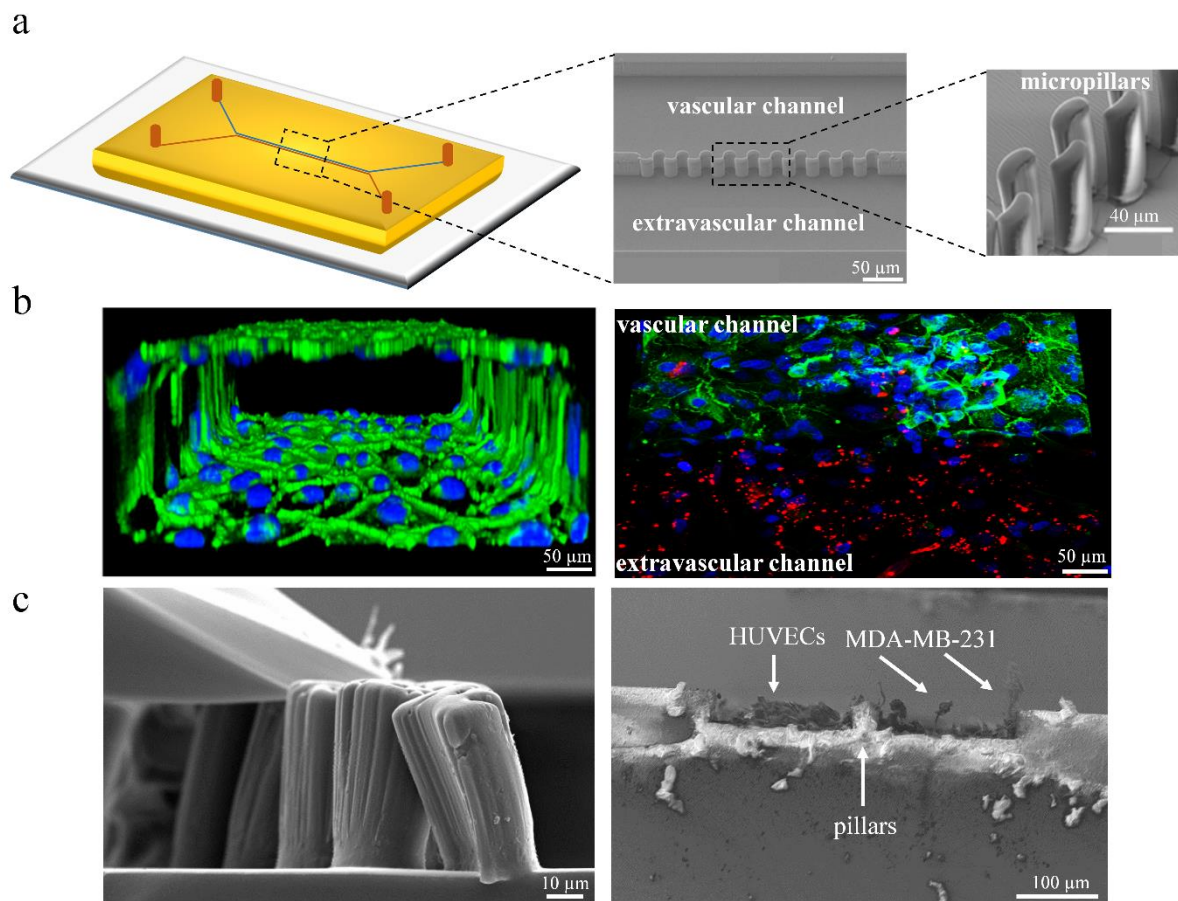

Figure 4.1. The compartmentalized microfluidic device. a. Schematic of the double channel chip (length = 2.7 cm, width = 210 µm; height = 50 µm) with the vascular channel in blue and the extravascular channel in red (left); scanning electron microscopy micrographs showing the extravascular and vascular channels; and the micro-membrane made out of micropillars, (right). **b.** Representative confocal fluorescent images of a confluent HUVEC monolayer in the vascular compartment (left) and MDA-MB-231 breast cancer cells mixed in a matrigel layer in the extravascular compartment (right). Cell nuclei are stained in blue with DAPI, VE-Cadherin proteins are stained in green, cellular membrane is stained in red with CM-DIL. **c.** Scanning electron

microscopy micrographs showing details of the micro-membrane and its pillars (left), and cross section of the vascular channel filled with HUVECS and extravascular compartment filled with MDA-MB-231 cells (right).

Vascular permeability at the micro-membrane. In order to test the functionality of the endothelial barrier, the vascular channel was seeded with endothelial cells while the other channel was filled with matrigel to mimic the extracellular matrix. Endothelial cells spontaneously cover the walls, including the permeable micro-membrane. The diffusion of a green fluorescent tracer (FITC–Dextran 40 kDa) from the vascular to the extravascular compartment was analyzed to retrieve values for the vascular permeability P, under different operating conditions. Specifically, endothelial cells were stimulated with the pro-inflammatory molecule TNF-α to modulate intercellular adhesion and, thus, vascular permeability. The fluorescent images in **Figure.4.2a** document the permeation of the tracer in the extravascular space at 3 different time points, namely 5, 15 and 30 min post infusion. Dextran molecules were observed to flow into the vascular channel, permeate across the micro-membrane, and diffuse into the matrigel matrix. The diffusion of the fluorescent molecule is inversely proportional to the tightness of the endothelial junctions, which are loosened by the treatment with TNF-α. In the absence of endothelial cells (no HUVECs), the tracer easily flows into the extravascular compartment returning permeability values as high as 9.25 ± 3.96 µm/s. On the contrary, the presence of a continuous endothelial layer dramatically reduces the vascular permeability of the 40 kDa tracer to 1.01 ± 0.34 µm/s.
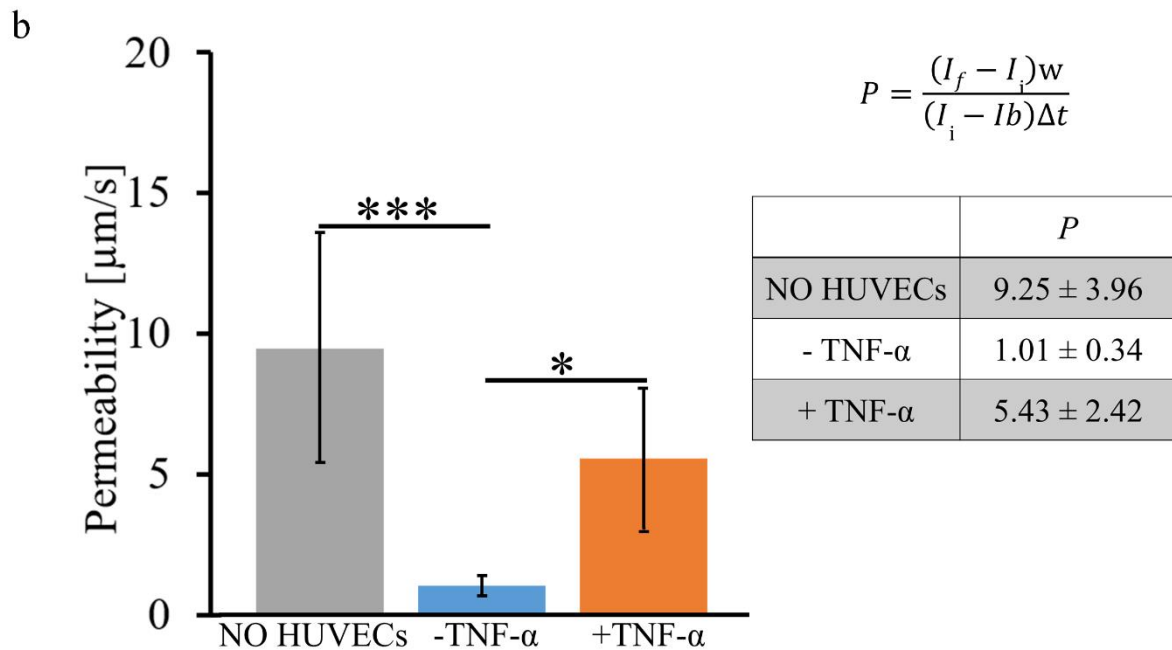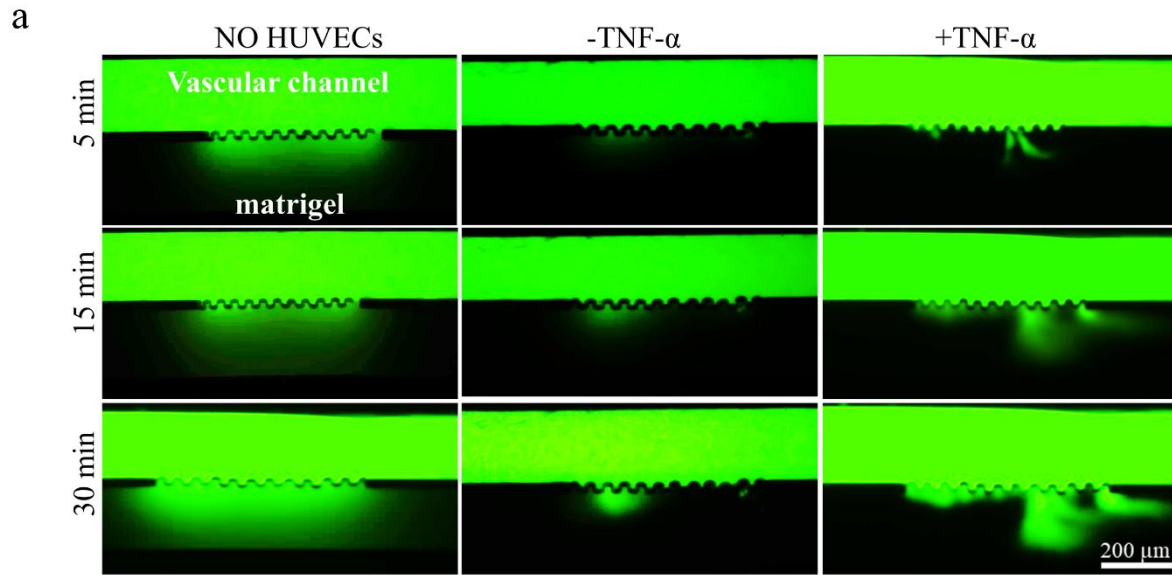
Figure 4.2. Vascular permeability at the micro membrane. a. Representative fluorescent images of free FITC-Dextran (40 kDa) diffusing (Q = 100 nL/min) in the vascular channel with an healthy (- TNF-α); inflamed endothelium (+ TNF-α) and with no endothelial cells (NO HUVECs) (TNF-α treatments were performed at 50 ng/mL for 12h). **b.** Vascular permeability coefficients. Formula for calculating the permeability (right). Data are plotted as mean + SD, n = 5. Statistical analysis ANOVA. * denotes statistically significant difference p<0.05. *** denotes statistically significant difference p<0.01.

Furthermore, the stimulation with TNF-α, which was added in the extravascular compartment at 50 ng/mL, affects the tight junctions (**Figure.4.3**) of the endothelial cells and increases the permeability of the tracer up to 5.43 ± 2.42 µm/s.
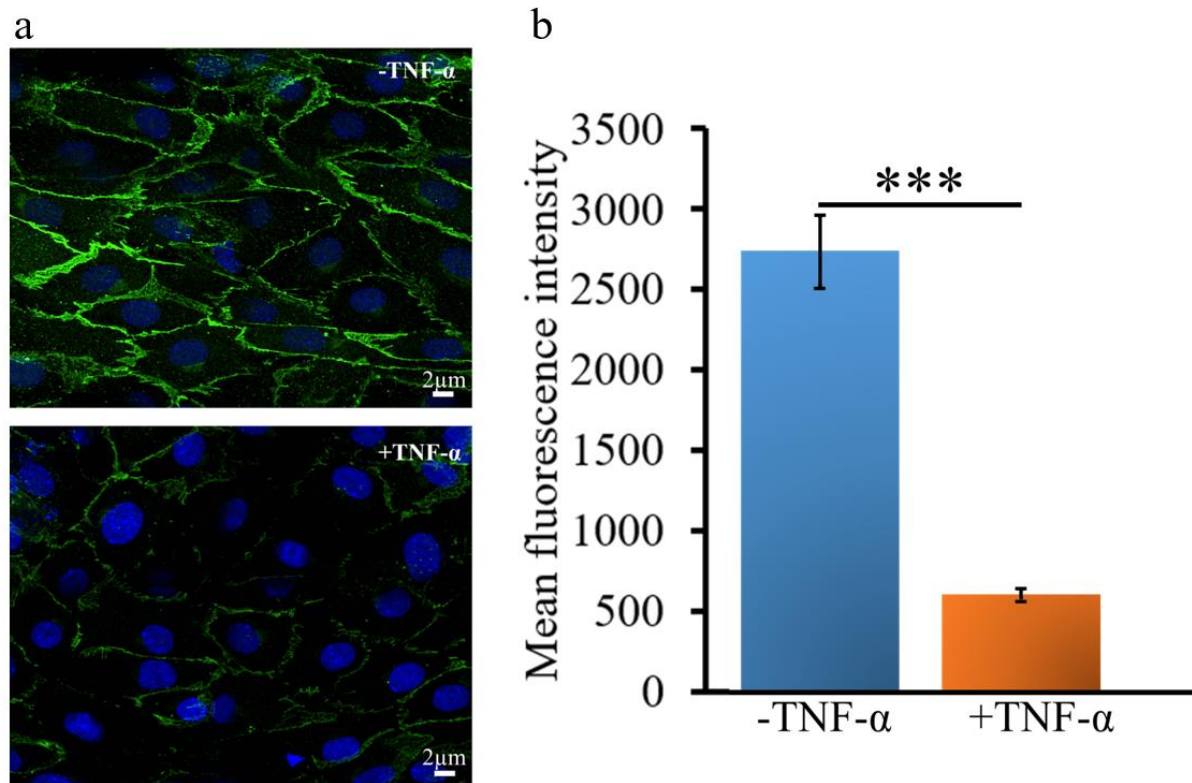
Figure 4.3. VE-cadherin molecules expression on HUVEC cells. a. VE-Cadherin immunostaining in unstimulated (-TNF-α - top image) and stimulated conditions (+TNF-α – bottom image). Nuclei were stained in blue using DAPI, VE-Cadherin adhesion molecule is shown in green. **b.** Mean fluorescence intensity of the VE-Cadherin expression for the two different conditions. Data are plotted as mean + SD, n = 4. Statistical analysis T test. *** denotes statistically significant difference p<0.0001.

Note that the TNF-α concentration is low enough to avoid any toxic and irreversible effect on the cells but sufficient to alter adhesive molecules expression (**Figure.4.4**).

Figure 4.4. Visualization of ICAM-1 adhesion molecules in the microfluidic chip. **a.** Confocal fluorescent microscopy images of the chip with a confluent layer of HUVECs, under unstimulated 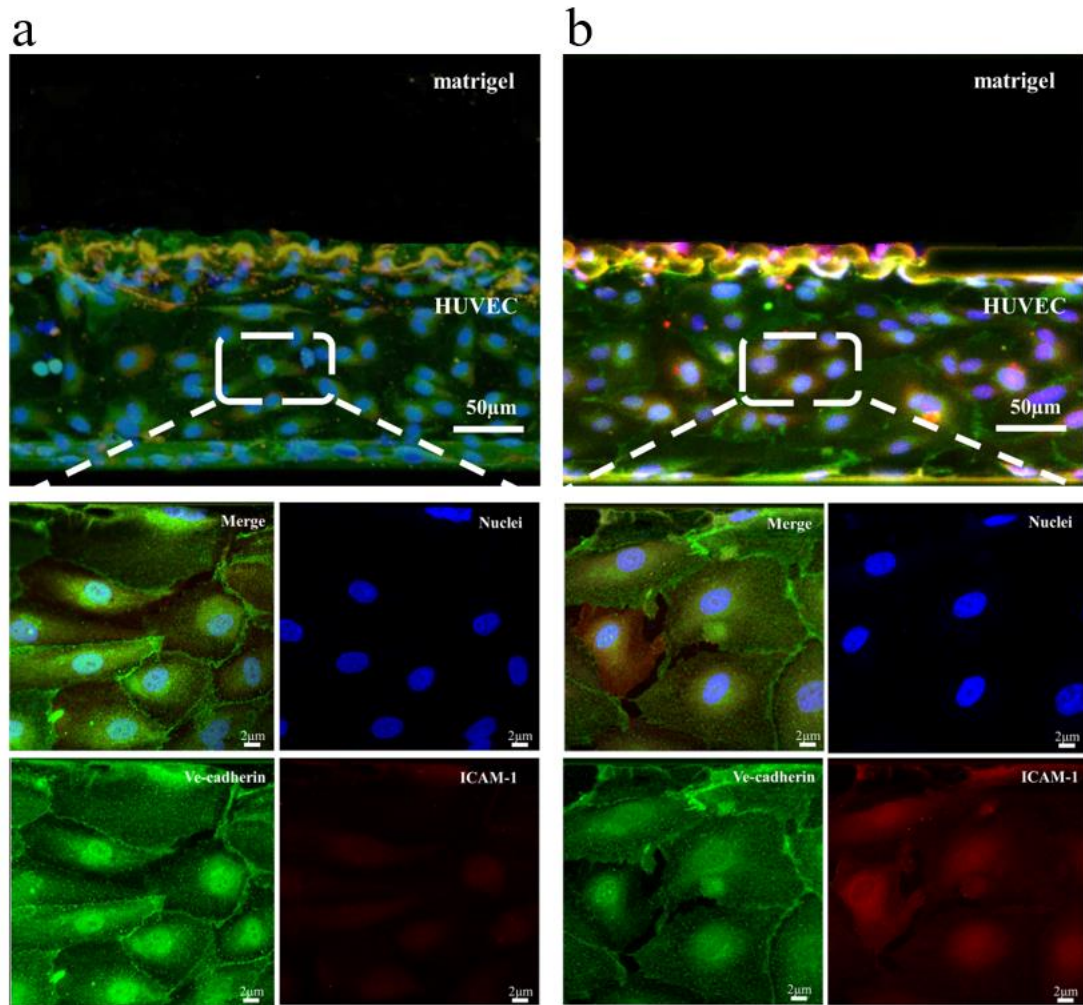conditions (-TNF-α) (top). Confocal fluorescent images into different channels (60 x magnification) were obtained using Split-Channels and then recombining the images using Merge-Channels (bottom). Nuclei stained in blue with DAPI, VE-Cadherin immunostaining in green, ICAM-1 immunostaining in red. **b.** Representative confocal fluorescent microscopy image of chip with a confluent layer of HUVECs, under stimulated conditions (+ TNF-α,) (top). Confocal fluorescent images into different channels (60 x magnification) were obtained using *Split-Channels* and recombining the images using *Merge-Channels* (bottom). Nuclei stained in blue with DAPI, VE-Cadherin immunostaining in green, ICAM-1 immunostaining in red.

In all cases, the obtained values are slightly higher with respect to in vivo data, but are in line with in vitro data reported by other authors.[193] The chart in **Figure.4.2b** gives the permeability values as well as the formula employed to extract these values from the experimental data. Indeed, these results

demonstrate the ability to modulate the vascular permeability in the device by properly stimulating confluent endothelial cells.

Permeability experiments were also conducted at lower flow rates, namely 50 nL/min (**Figure.4.5**). Importantly, only a minor difference in permeability was observed for the two different flow rates.

$$P = \frac{(I_f - I_i)\text{w}}{(I_i - Ib)\Delta t}$$

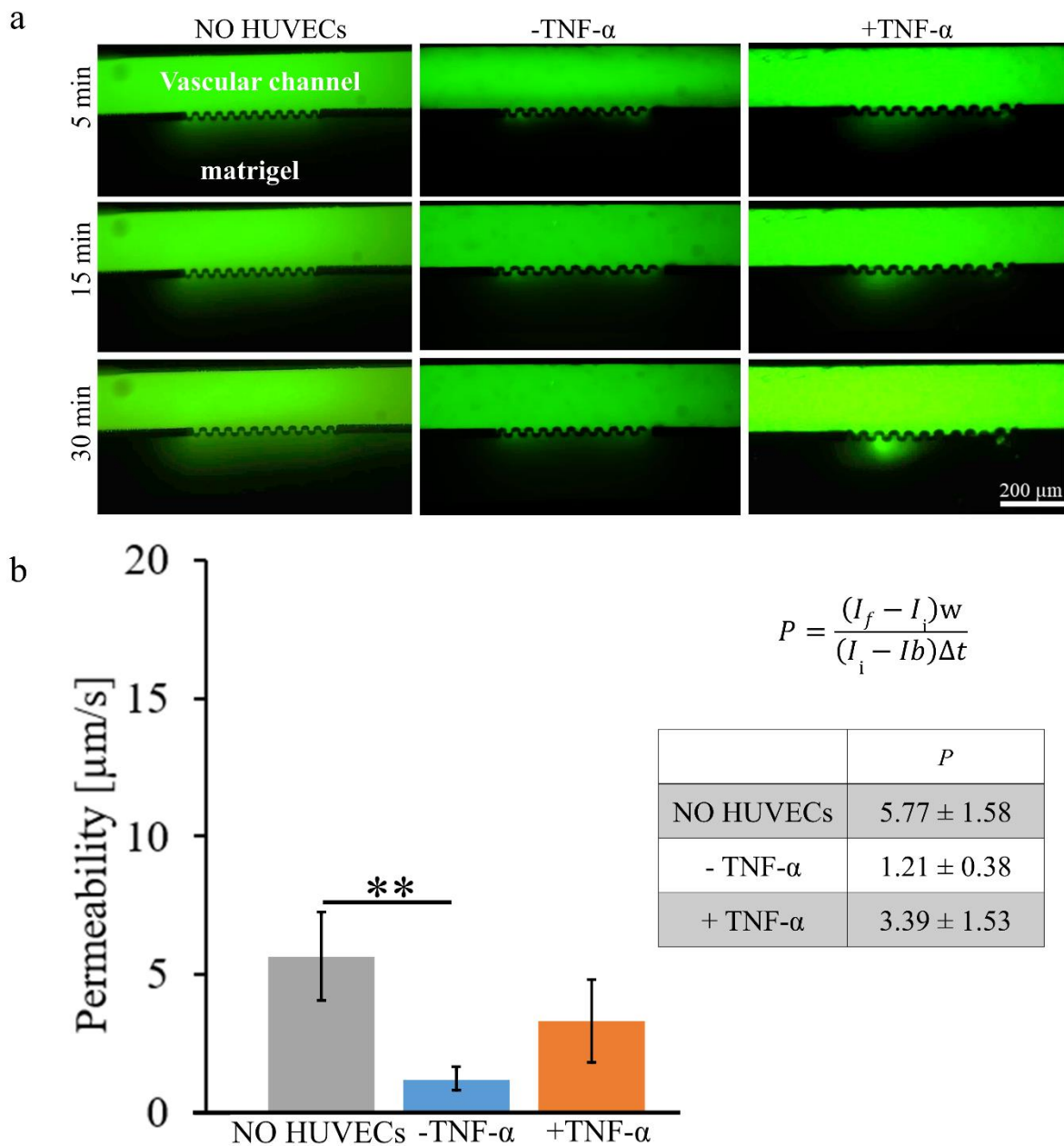|	P
NO HUVECs	5.77 ± 1.58
- TNF-α	1.21 ± 0.38
+ TNF-α	3.39 ± 1.53

Figure 4.5. Vascular permeability at the micro-membrane at Q = 50 nL/min. a. Representative fluorescent images of free FITC-Dextran (40 kDa) diffusing (Q = 50 nL/min) in the vascular channel with an healthy (-TNF-α); inflamed endothelium (+ TNF-α) and with no endothelial cells (NO HUVECs) (TNF-α treatments

were performed at 50 ng/mL for 12h). **b.** Vascular permeability coefficients. Formula for calculating the permeability (right). Data are plotted as mean + SD, n = 5. Statistical analysis ANOVA. ** denotes statistically significant difference p<0.05.

Modeling the intravasation of cancer cells. After assessing the vascular permeability of the device under different flows conditions and TNF-α stimulations (**Figure.4.6**), the transport of breast cancer cells (MDA-MB-231) across the endothelialized micro-membrane into the vascular compartment was considered.

$$P = \frac{(I_f - I_i)w}{(I_i - Ib)\Delta t}$$

	P
NO HUVECs	9.25 ± 3.96
+ TNF-α (12h)	5.42 ± 2.42
- TNF-α (3h)	4.47 ± 0.43
- TNF-α (6h)	2.02 ± 1.11
- TNF-α (12h)	1.01 ± 0.34
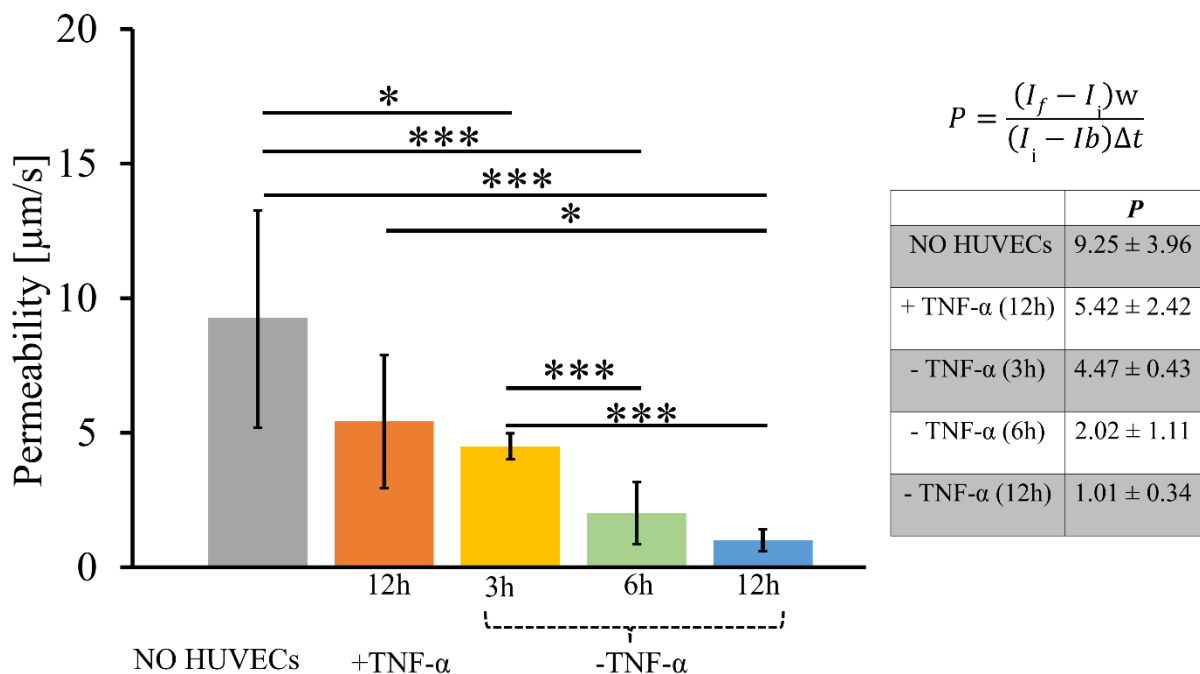
Figure 4.6. Vascular permeability at the micro-membrane at Q = 100 nL/min. Vascular permeability coefficients for FITC-Dextran (40 kDa) in the vascular channel on healthy HUVECs (- TNF-α) 12 h after seeding; 3h post HUVEC seeding; 6h post HUVEC seeding; on inflamed endothelium (+ TNF-α) 12h after seeding and with no endothelial cells (NO HUVECs) (TNF-α treatments were performed at 50 ng/mL for 12h). The formula for calculating the permeability coefficients (right). Data are plotted as mean + SD, n = 5. Statistical analysis ANOVA. * denotes statistically significant difference p<0.05. *** denotes statistically significant difference p<0.001 (Q = 100 nL/min).

Tumor cells were mixed with matrigel and infused into the extravascular compartment, whereas endothelial cells were seeded and cultured in the vascular channel. During the whole experiment, cell culture medium was continuously infused on the vascular side with a flow rate of Q = 50 nL/min, which is typical for microvascular flow.[194] Despite the high density of matrigel, the fresh medium and nutrients in the vascular channel were sufficient to attract cancer cells. Intravasation events were observed over time and were only accounted for when the whole cell body was found in the vascular compartment. **Figure.4.7a** presents a schematic of the model and fluorescent microscopy images at the two compartments taken at 0, 6, 21, 24 and 30 h post cell seeding. These images document a progressive infiltration of the breast cancer cells (cell membrane in red – CM-DiI) into the vascular compartment, which is confluently covered by endothelial cells (cell nuclei in blue – DAPI). It should be noted that in some of the microfluidic chips a small number of HUVECs migrated into the extravascular compartment. Indeed, HUVECs feel the presence of cancer cells and their cytokines, and respond to their biological stimuli by migrating into extravascular channel.
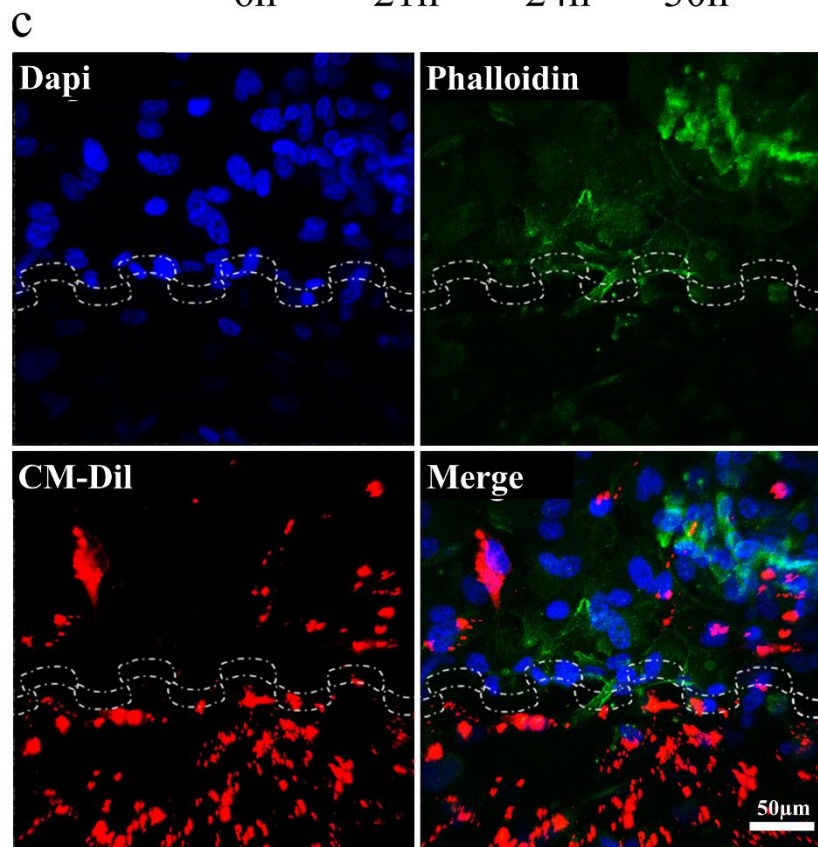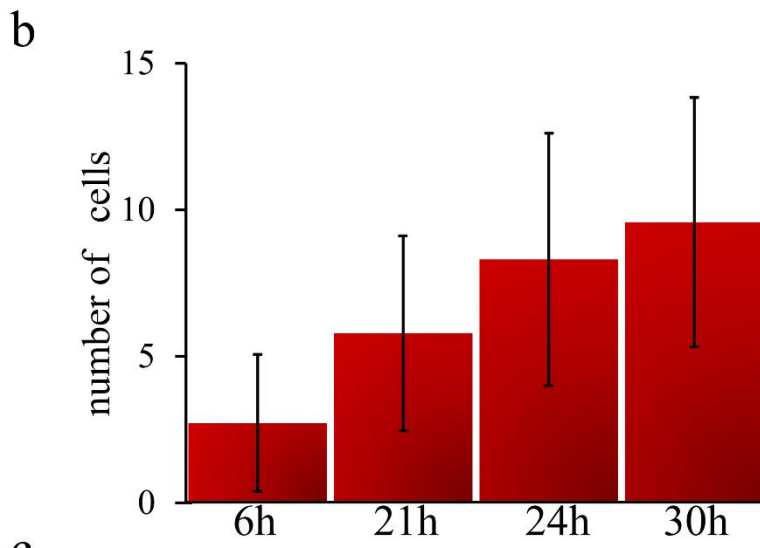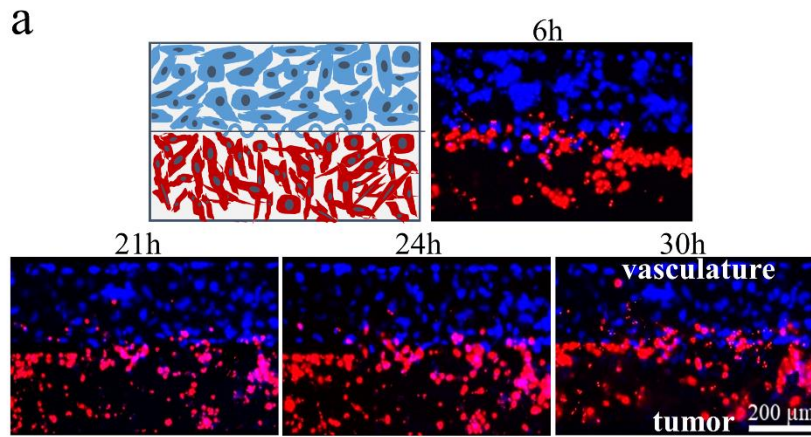
a

6h

21h   24h   30h

vasculature

tumor   200 μm

b

c

Dapi   Phalloidin

CM-Dil   Merge

50μm

Figure 4.7. Modeling the intravasation of cancer cells. a. A schematic (top left) of the model and fluorescent microscopy images of the two compartments, taken at 6, 21, 24 and 30h. The images depict cancer cells (cell membrane labeled in red with CM-Dil) intravasated from the extravascular compartment filled with a matrigel matrix to the vascular compartment covered by a confluent layer of HUVECs (cell nuclei stained in blue with DAPI). **b.** Quantification of the number of intravasated cancer cells up to 30h. Data are plotted as mean + SD, n=8. **c.** Confocal fluorescent images into different channels were obtained using *Split-Channels* and recombining the images using *Merge-Channels*. HUVECs nuclei are stained in blue with DAPI, F-Actin is stained in green with phalloidin.

Moreover, matrigel does contain 5.0-7.5 ng/mL of vascular endothelial growth factor (VEGF) and traces of matrix metalloproteinases (MMP) that could contribute to this process. The number of MDA-MB-231 was calculated by observing the tumor cells for 30h at the time-lapse microscope. This shows tumor cells migrating into the matrigel matrix, crossing the endothelial barrier, and reaching the vascular compartment. In **Figure.4.8** the trajectory and velocity of an individual intravasated tumor cell are reported. The analysis was performed with a time-lapse microscope returning an average speed of about 0.008 µm/sec, and a total variation in speed from 0.0005 to 0.018 µm/sec.
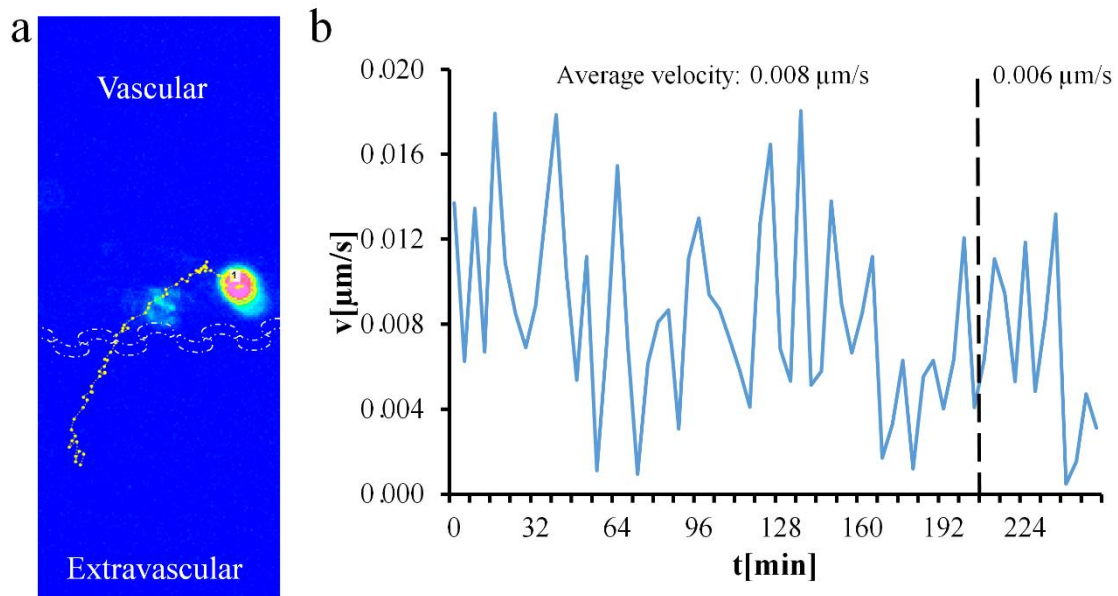
Figure 4.8. Cancer cell intravasation: single cell tracking and instantaneous velocity a. Trajectory of a breast cancer cell MDA-MB-231 moving from the extravascular compartment, filled with a matrigel matrix, across the micro-membrane, to the vascular compartment filled with a confluent monolayer of HUVECs. The tracking is performed via time lapse microscopy. **b.** Cancer cell velocity over time during intravasation calculated by time lapse microscopy. The dashed black line indicates when the micro-membrane is crossed by the cell.

In **Figure.4.9** details on the morphology of intravasating cancer cells are provided. As compared to HUVECs, the migrating cancer cells appear elongated.
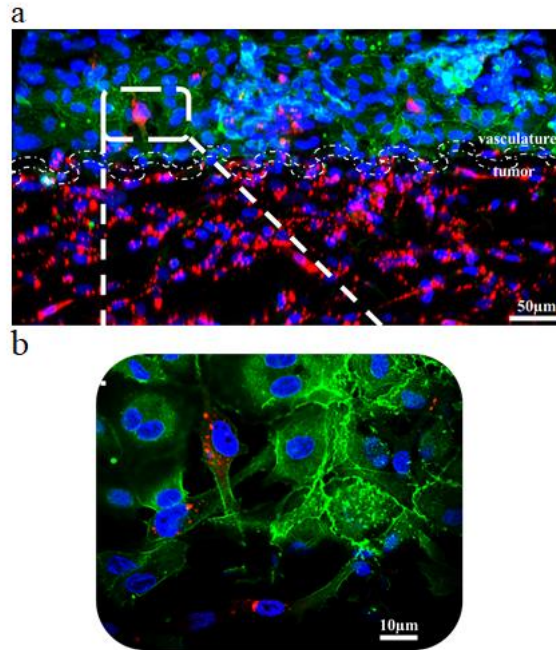
Figure 4.9. Cancer cell intravasation a. Confocal fluorescent microscopy image showing breast cancer cells (MDA-MB-231, red) intravasating from the extravascular compartment, filled with a matrigel matrix, to the vascular compartment, filled with a confluent HUVEC monolayer. **b.** Magnified image at 60 x showing tumor cells (red) in an elongated shape, infiltrating the HUVEC monolayer. (Breast cancer cells have the membrane labeled in red with CM-DiI. Nuclei are stained in blue with DAPI. F-Actin is stained in green).

In **Figure.4.7b**, the number of intravasated tumor cells is plotted at specific time points, returning the averaged values 2.70 ± 2.31 at 6h; 5.77 ± 3.30 at 21h; 8.28 ± 4.30 at 24h; 9.55 ± 4.24 at 30h. In **Figure.4.7c** and in **Figure.4.9,** confocal fluorescent images of the device depict the intravasated cancer cells (red) across the micro-membrane. MDA-MB-231 cells are stained in red with CM-DiI, the nuclei of the HUVECs are stained in blue with DAPI and the F-Actin filaments of both cells are stained in green with Alex Fluor 488 phalloidin (for **Figure.4.9** notice that nuclei of both HUVECs and MDA-MB-231 are stained in blue with DAPI). It should be here emphasized that similar images and data on cell migration velocity could have not been taken in a Boyden chamber assay.

Modeling vascular transport and adhesion of cancer cells. After intravasation into the vascular compartment, tumor cells are transported by the blood flow until vascular adhesion occurs at secondary sites. To model this process, MDA-MB-231 cells were infused in the endothelialized vascular channel at 50 and 100 nL/min. To modulate the adhesion propensity of the cancer cells, HUVECs were either treated with 50 ng/mL of TNF-α (inflamed endothelium) or left in their basal state (no inflammation). The stimulation with TNF-α enhances the expression of specific molecules, such as the vascular cell adhesion, proteins and integrins that mediate cell adhesion. As in the previous section, TNF-α (50 ng/mL) was added in the extravascular compartment, mimicking an inflammatory stimulus originating deep in the tissue and eventually reaching the endothelial barrier. **Figure.4.10a** reports representative fluorescent images showing breast cancer cells (red – CM-DiI) adhering onto HUVECs (blue – DAPI), under the two tested flow rates. The number of adhering cancer cells was quantified and normalized by the total number of injected cells ($n_{inj} = 10^6$) and the area of the region of interest (ROI) (**Figure.4.10b**). At low flow rates, the number of adhering cancer cells was equal to 12.94 ± 4.47 for unstimulated conditions (-TNF-α) and 29.75 ± 4.19 for stimulated conditions (+TNF-α). At higher flow rates, the number of adhering cancer cells decreased to 8.38 ± 3.14 for unstimulated conditions (-TNF-α) and 21.00 ± 4.38 for stimulated conditions (+TNF-α). As expected, CTCs would adhere on the inflamed endothelium almost 3-times more than on the healthy vasculature. Differently, CTCs would more stably roll on the healthy endothelium rather than on the inflamed vasculature.
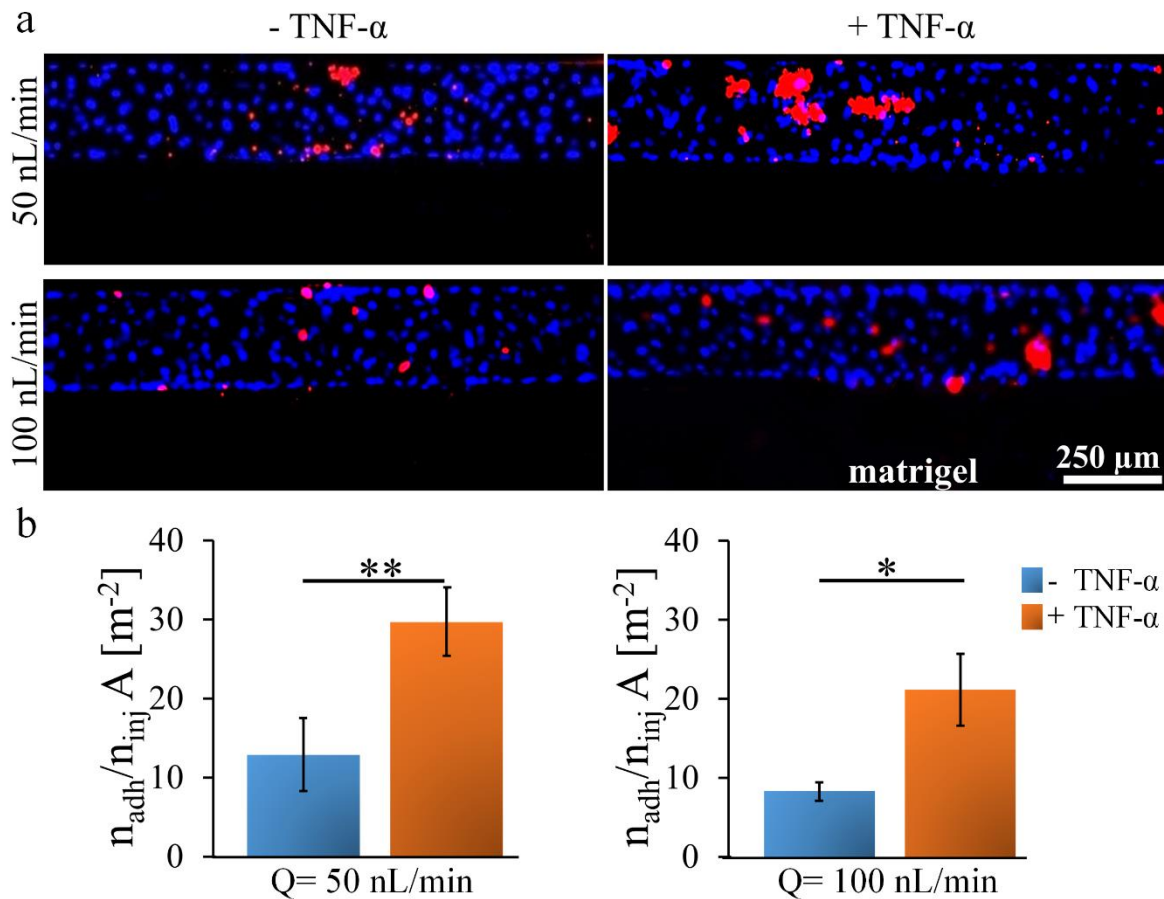
Figure 4.10. Modeling the vascular transport and adhesion of cancer cells. a. Representative fluorescent microscopy images depicting breast cancer cells (cell membrane labeled in red with CM-DIL) adhering over a confluent HUVEC monolayer (cell nuclei stained in blue with DAPI). HUVECs are either inflamed for 12h with TNF-α (50 ng/mL) (+ TNF-α) or not inflamed (- TNF-α). **b.** Normalized number of adhering cancer cells for flow rate Q = 50 nL/min (bottom left) and Q = 100 nL/min (bottom right). Data are plotted as mean + SD, n=3. Statistical analysis ANOVA. * denotes statistically significant difference p<0.05. ** denotes statistically significant difference p<0.01.

Modeling the extravasation of cancer cells. After establishing stable adhesion with the blood vessel walls, tumor cells can migrate towards the extravascular space infiltrating the healthy tissue.[195] MDA-MB-231 cell extravasation from the vascular compartment was evaluated tracking cells for 30h on a time-lapse microscope. In this configuration, tumor cells are required to cross the endothelial barrier.

As such, HUVECs (blue – DAPI) were seeded in the vascular compartment to form a confluent cell layer, while MDA-MB-231 (red – CM-DiI) were infused in the same compartment at 50 nL/min. The extravascular channel was filled with a mix of matrigel, TNF-α and FITC-Dextran (4 kDa). The Dextran 4 kDa tracer was included to monitor the transport of small molecules, such as TNF-α, from the tissue to the vascular compartment. The transmigration of MDA-MB-231 into the matrigel matrix was then observed over time. Representative fluorescent microscopy images of the extravasated cancer cells are shown in **Figure.4.11a** at different time points. **Figure.4.11b** reports the absolute number of extravasated cells, namely, 1.42 ± 0.78 at 3h, 2.42 ± 0.97 at 6h, 3.71 ± 0.75 at 21h, 4.42 ± 1.39 at 24h, 5.00 ± 1.91 at 30h.

a

3h 6h

21h 24h 30h

matrigel

200 μm

b

c

Dapi Phalloidin

CM-Dil Merge

50μm
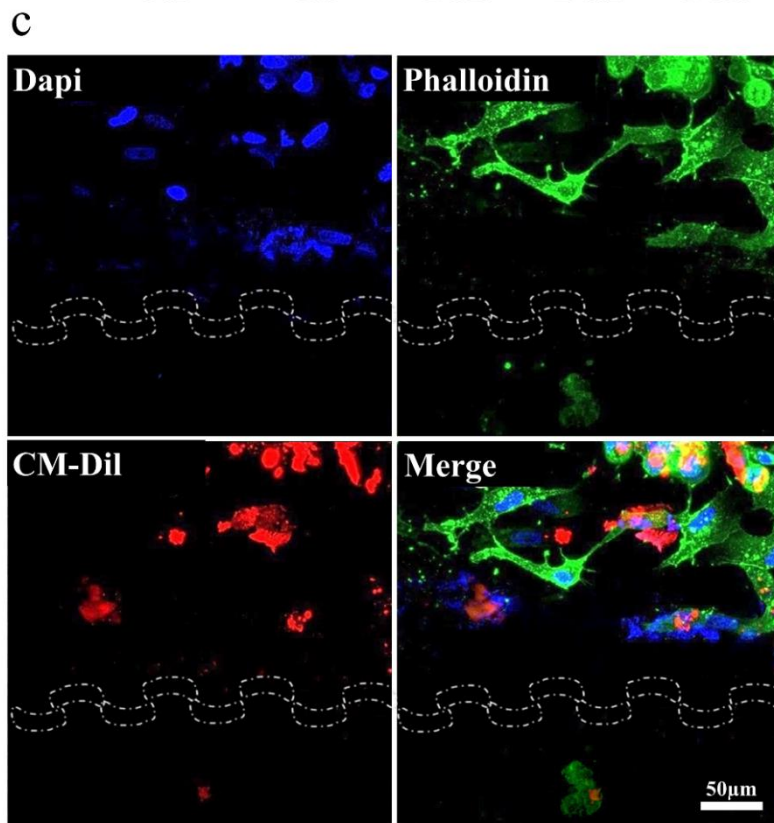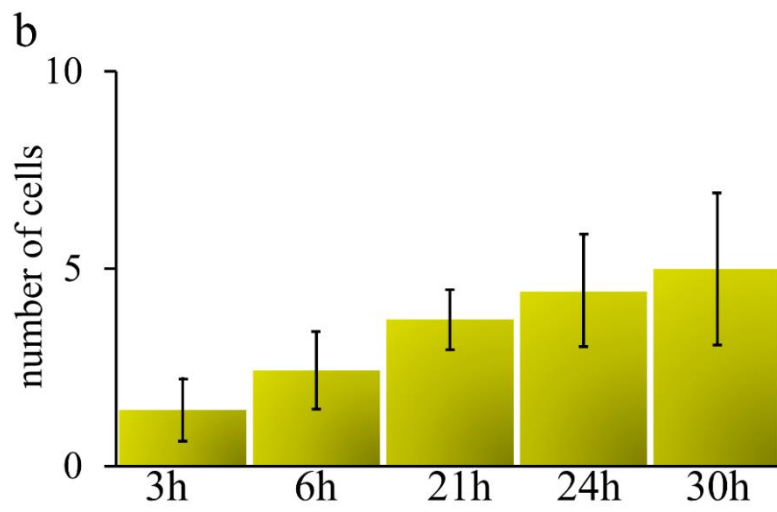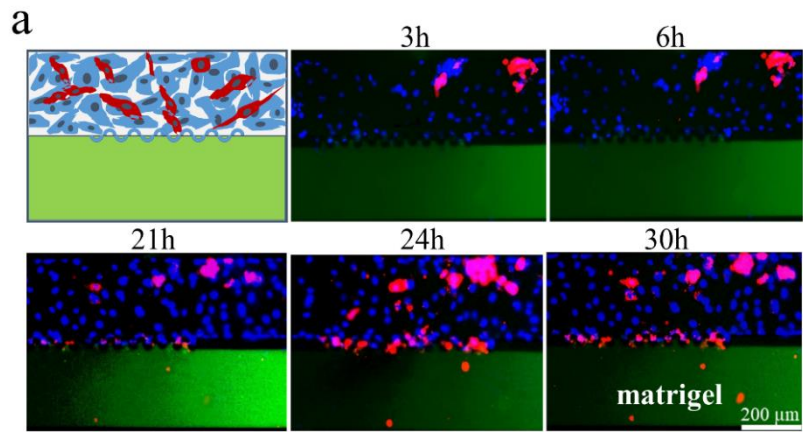
Figure 4.11. Modeling the extravasation of cancer cells. A schematic (top left) of the model and fluorescent microscopy images of the two compartments taken at 3, 6, 21, 24 and 30h. Images depict cancer cells (cell membrane labeled in red with CM-Dil) infiltrating from the vascular compartment, filled with HUVECs (cell nuclei stained in blue with DAPI), to the extravascular compartment filled with matrigel. **b.** Quantification of the number of extravasated cancer cells up to 30h. Data are plotted as mean + SD, n=8. **c.** Confocal fluorescent images into different channels were obtained using *Split- Channels* and recombining the images using *Merge-Channels*. HUVECs nuclei are stained in blue with DAPI, F-Actin is stained in green with phalloidin.

In **Figure.4.12,** the trajectory and the velocity of an individual extravasated tumor cell are reported. The analysis was performed with a time-lapse microscope. The average speed of the tumor cell is 0.002 µm/sec, with an overall variation between 0.013 and 0 µm/sec.
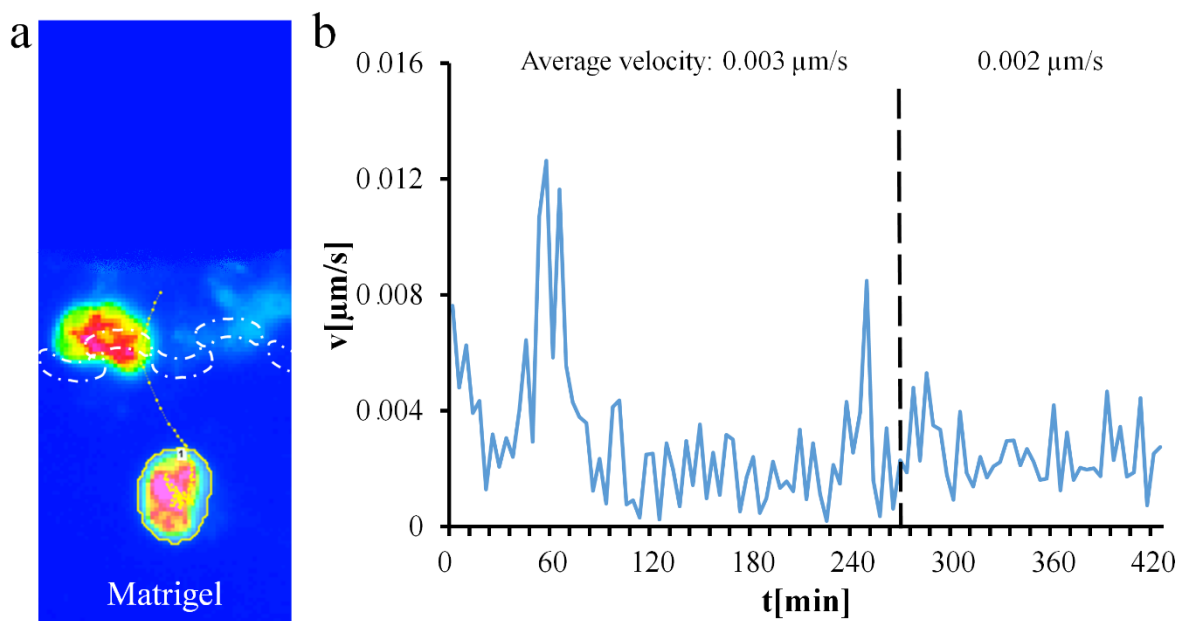
Figure 4.12. Cancer cell extravasation: single cell tracking and instantaneous velocity a. Trajectory of a breast cancer cell MDA-MB-231 moving from the vascular compartment, filled with a confluent HUVEC monolayer, across the micro-membrane, to the extravascular compartment, filled with a matrigel matrix. The tracking is performed via time lapse-microscopy. **b.** Cancer cell velocity over time during extravasation

calculated by time lapse-microscopy. The dashed black line indicates when the micro-membrane is crossed by the cell.

Figure.4.12c and **Figure.4.13** report confocal fluorescent images of the device depicting the extravasated cancer cells across the micro-membrane. MDA-MB-231 cells are stained in red with CM-DiI, the nuclei of the HUVECs are stained in blue with Dapi and the F-Actin filaments of both cells are stained in green with Alexa Fluor 488 phalloidin (for **Figure.4.13** notice that nuclei of both HUVECs and MDA-MB-231 are stained in blue with DAPI).
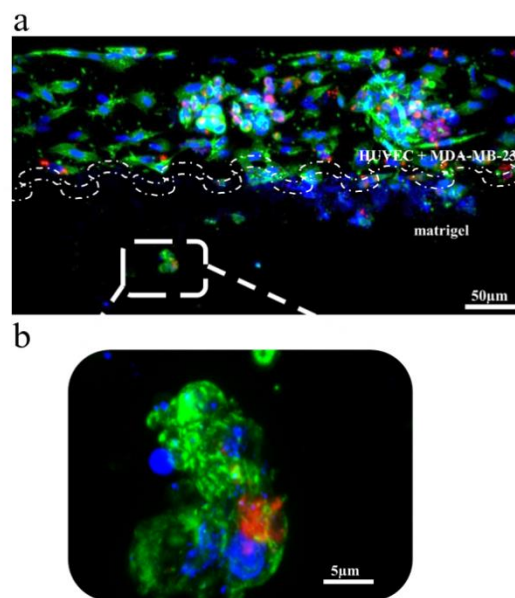
Figure 4.13. Cancer cell extravasation. a. Confocal fluorescent microscopy image showing breast cancer cells (MDA-MB-231, red) extravasating from the vascular compartment, filled with a confluent HUVEC monolayer, to the extravascular compartment filled with a matrigel matrix. **b.** Magnified image at 60 x showing tumor cells (red), infiltrating the extravascular compartment. Breast cancer cells have the membrane labeled in red with CM-DiI. Nuclei are stained in blue with DAPI. F-Actin is stained in green.

Modeling the tissue invasion of cancer cells. After extravasation, cancer cells colonize the secondary sites by penetrating deeper into the tissue and forming metastatic niches. In this step, cancer

cells interact with local microenvironment, including stromal cells, that would facilitate invasion by releasing chemokines, MMPs and other molecules[196].

To model this step of the metastasis cascade, the device was filled with a mix of matrigel, TNF-α and FITC-Dextran 4 kDa in one channel, and MDA-MB-231 cells embedded in matrigel in the other channel. Cancer cell migration from one side to the other was evaluated by tracking cells for up to 30h, using a time-lapse microscope. **Figure.4.14a** shows the schematic of the chip and representative fluorescent images taken using an inverted microscope. The absolute number of migrating cells was charted in **Figure.4.14b** returning the values at 0.50 ± 0.81 at 3h, 2.42 ± 1.30 at 6 h, 10.42 ± 3.78 at 21h, 12.71 ± 4.03 at 24h and 14.71 ± 3.13 at 30 h.

a

3h 6h

21h 24h 30h

matrigel

matrigel 200 μm

b

number of cells

20

15

10

5

0

3h 6h 21h 24h 30h

c

Dapi Phalloidin

CM-Dil Merge

50μm
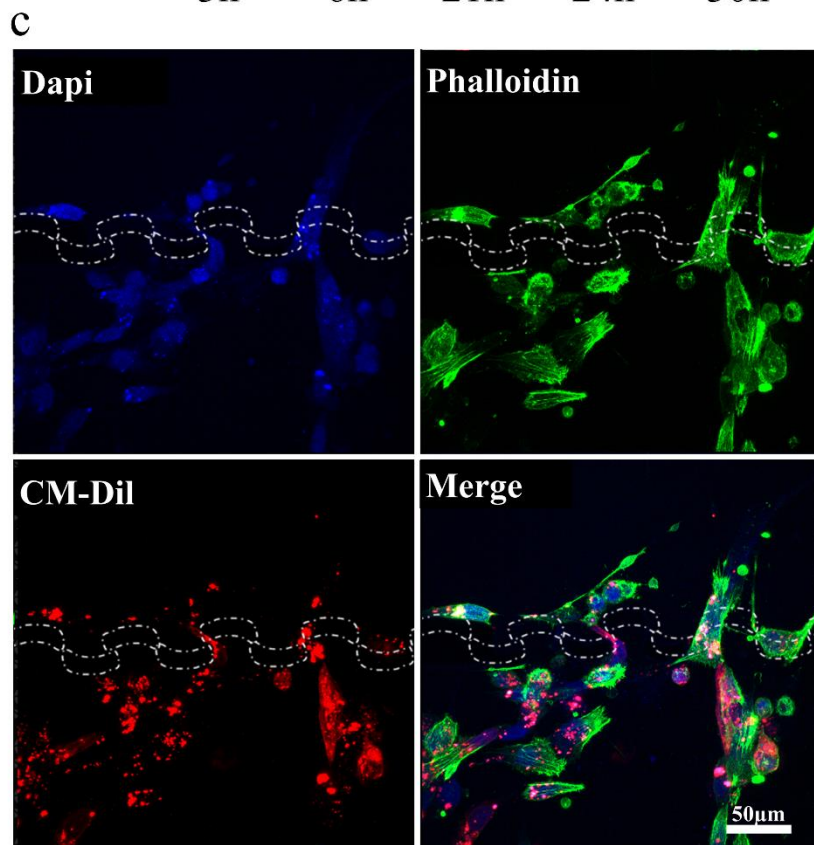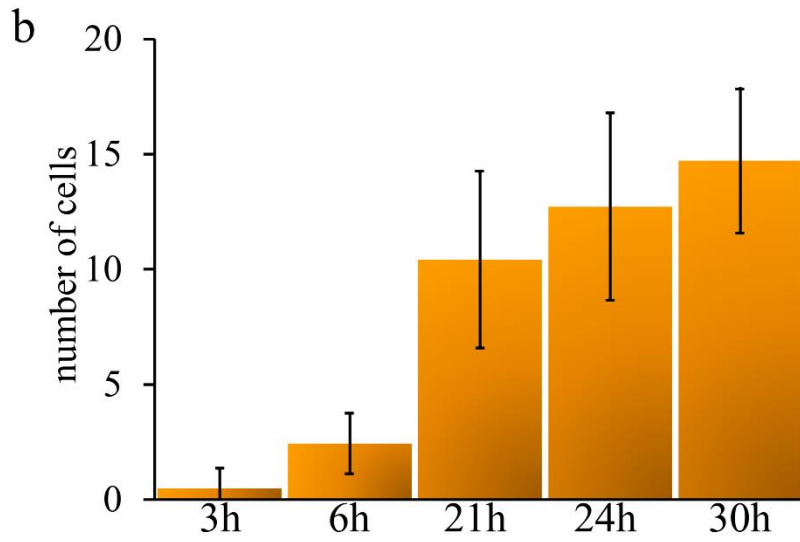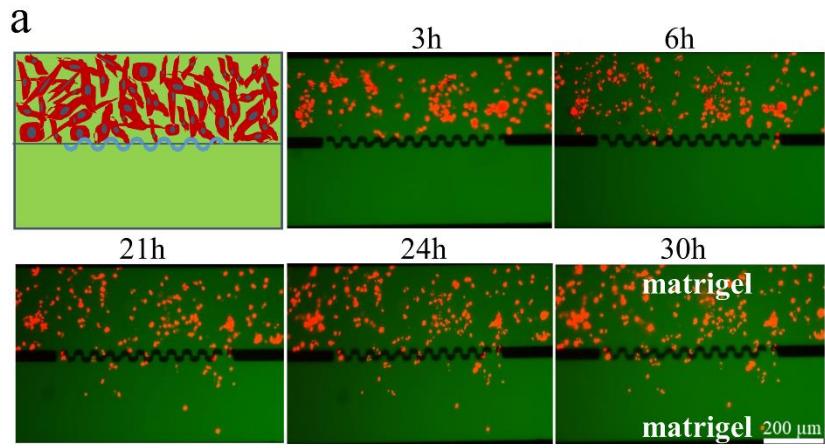
Figure 4.14. Modeling the tissue invasion of cancer cells. **a.** A schematic (top left) of the model and fluorescent microscopy images of the two compartments taken at 3, 6, 21, 24 and 30h. The images depict cancer cells (cell membrane labeled in red with CM-Dil) embedded in a matrigel matrix moving from one to the other compartment. **b.** Quantification of the number of migrated cancer cells up to 30h. Data are plotted as mean + SD, n=8. **c.** Confocal fluorescent images of the different channels were obtained using *Split-Channels* and recombining the images using *Merge-Channels*. Nuclei are stained in blue with DAPI, F-Actin is stained in green with phalloidin.

In **Figure.4.15**, the trajectory and velocity of an individual tumor cell are reported. The average cell speed is 0.005 µm/sec, with a total variation ranging between 0.011 and 0 µm/sec. Cancer cells move along the TNF-α gradient crossing the channels from one side to the other through the permeable micro-membrane. Indeed, for this study, no endothelial cells were included. A drop of cell culture medium was added to the inlet and to the outlet ports to prevent matrigel drying.
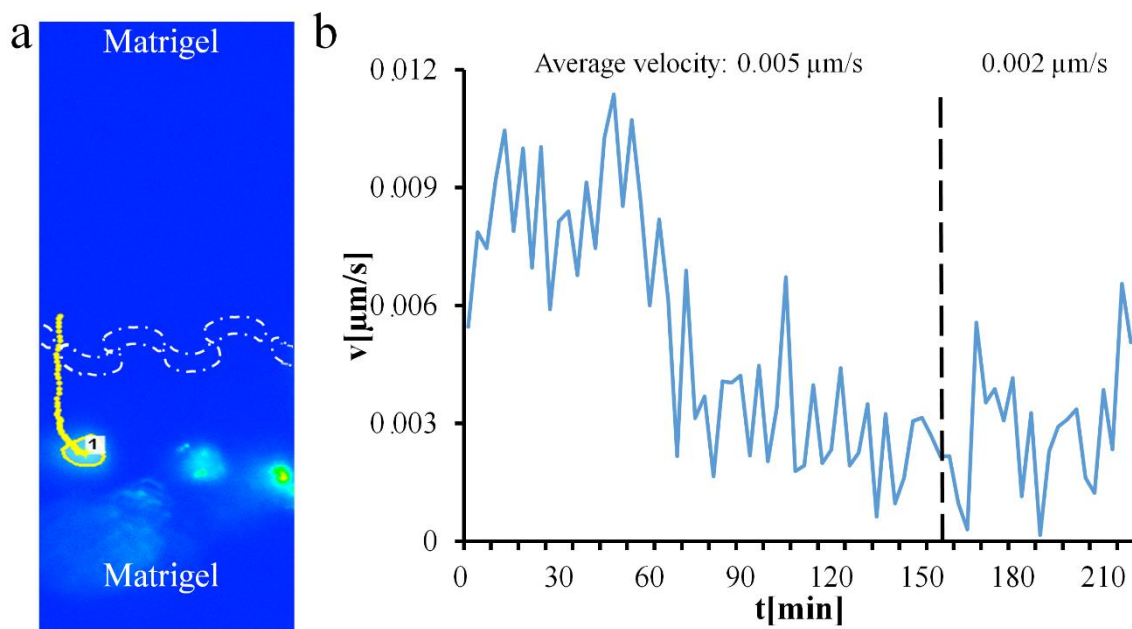
Figure 4.15. Cancer cell invasion: single cell tracking and instantaneous velocity a. Trajectory of a breast cancer cell MDA-MB-231 moving from a compartment, filled with a matrigel matrix, across the micromembrane, to the other compartment, filled with a matrigel matrix. The tracking is performed via time

lapse-microscopy. **b.** Cancer cell velocity over time during invasion calculated by time lapse-microscopy. The dashed black line indicates when the micromembrane is crossed by the cell.

Figure.4.14c and **Figure.4.16** report confocal fluorescent images depicting the migrating cancer cells across the micro-membrane. MDA-MB-231 cells are stained in red with CM-DiI, the nuclei are stained in blue with DAPI and the F-Actin filaments are stained in green with Alex Fluor 488 phalloidin.
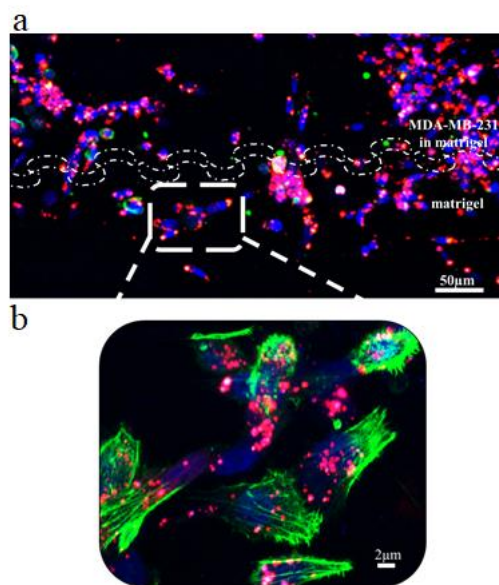
Supporting Figure 4.16. Cancer cell invasion. a. Confocal fluorescent microscopy image showing breast cancer cells (MDA-MB-231, red) migrating from a compartment, to the other compartment, both filled with a matrigel matrix. **b.** Magnified image at 60 x showing tumor cells (red) in an elongated shape, infiltrating the other compartment. Breast cancer cells have the membrane labeled in red with CM-DiI. Nuclei are stained in blue with DAPI. F-Actin is stained in green.

4.4 CONCLUSION

A compartmentalized microfluidic chip has been realized comprising two channels acting as the vascular compartment, coated by a confluent layer of endothelial cells, and the tissue compartment, filled by a matrigel matrix enriched with breast cancer cells. A micro-membrane, made out of an array of rounded pillars, separates the two channels and realizes the chip compartmentalization. Multiple key steps in the cancer metastasis process – intravasation, vascular transport and adhesion, extravasation and tissue invasion – have been reproduced in this compartmentalized microfluidic chip under controlled conditions. Importantly, as the two channels rest on the same plane, the trans-membrane dynamics of molecules and individual cancer cells can be monitored in real-time over several hours, using time-lapse fluorescent microscopy. This allows one to accurately quantify the rates of cell intravasation, adhesion, extravasation and invasion as well as to extract relevant information on cell morphology and biophysics.

No specific biological and biophysical information on organs and vascular districts were included in this version of the work as the main focus is on demonstrating the ability to control in real-time key steps in the metastatic cascade. Nonetheless, the size of the vascular chamber can be readily modified during the fabrication process and the flow rate can be accurately modulated by programming a syringe pump. By tuning these two parameters, the flow conditions in different vascular districts can be readily reproduced. As such, four conditions can be, for instance, recapitulated in vitro, as those found in 5 – 10 µm capillaries, with a mean blood velocity of 0.01 cm/sec; 10 – 50 µm arterioles, with a mean blood velocity of 0.6 cm/sec; 10 – 70 µm venules, with a mean blood velocity of 0.8 cm/sec; and 2 mm collecting lymphatic vessels, with a mean blood velocity of 10 cm/sec. Furthermore organ specific conditions can be integrated by using different types of endothelial cells within the vascular chamber, and multi-cellular mixture in the extravascular chamber. Considering flow conditions of venules, arterioles or large capillaries, in this work, MDA-MB-231 cells were observed to migrate towards the vascular compartment with a rate of about 8 cells per day. This process is

relatively rapid, with an average cell velocity of 0.5 µm/min. Notice, however, that the total number of cancer cells dispersed within the tissue compartment (matrigel matrix) and potentially available for intravasation is equal to about 4,000. In other words, the intravasation process is characterized by a low efficiency with only 0.2% of the tumor cells migrating from the malignant mass towards the vasculature each day. Indeed, this number can be affected by a variety of factors including the initial cell density. On the other hand, it was observed that cell extravasation requires stimulation with the pro-inflammatory molecule TNF-α, which favors the opening of the endothelial barrier and acts as a chemoattractant on tumor cells. Still, the rate of cell deposition within the extravascular space is of only 4 cells per day. This step in the metastatic cascade is even less efficient than intravasation and average cell velocities of about 0.1 µm/min were measured. TNF-α was also used for studying the invasion of cancer cells deep into the tissue. In this case, a migration rate of 12 cells per day over a 400 µm long region is observed. Is it important to highlight that these values of cancer cell velocity are in agreement with other in vitro and in vivo data available in literature as documented in the **Table.4.1**.

	Invasion Velocity (µm/h)	Extravasation Velocity (µm/h)	Intravasation Velocity (µm/h)	
MDA-MB-231 cells[197-199]	86.4		−	*in vivo*
	13-31	−	−	*in vitro*
	37.5-72	−	_	*in vitro*
MDA-MB-435 cells[200]	−	75.6	_	*in vivo*
Murine pancreatic cells[201]	14.04	−	−	*in vivo*
MTLn3 cells[202]	−	−	204	*in vivo*
MTC cells[202]	−	−	222	*in vivo*
HEp3 cells[203]	−	−	20-40	*in vitro*
Present work	18	7.2	28.8	*in vitro*

Table 4.1. Velocity of different cancer cells during the metastatic steps. Average velocity for invasion, extravasation and intravasation of MDA-MB-231 cells, MDA-MB-435, murine pancreatic, MTLn3, MTC and HEp3 cancer cells, in vitro and in vivo.

This quantitatively data on cell migration average speed, confirms that cancer metastasis is a highly inefficient process and specific conditions and stimuli are needed to support it. Intravasation, vascular adhesion, extravasation and invasion are all affected by a variety of biophysical and biochemical stimuli, including the local hemodynamic conditions, vascular permeability, expressions of adhesion molecules, availability of pro-inflammatory stimuli chemoattractant molecules, density and type of the extracellular matrix. The proposed two-channel compartmentalized microfluidic chip allows one to control accurately all the above parameters and provide a useful tool to systematically characterize the metastatic process dissect new biological mechanism or identify new anticancer therapies.

5. *Study T cell infiltration in a 3D microfluidic pancreatic tumour model*

5.1 INTRODUCTION

Pancreatic ductal adenocarcinoma (PDAC) is one of the most aggressive tumour showing a poor prognosis, with limited treatment options and a patient survival of less than 5%[204]. Compared to other solid tumors, PDAC shows a marked resistance to conventional forms of chemotherapy and often it develops without early symptoms making its diagnosis very difficult, limiting the treatment capacity. Several risk factors have been identified, such as smoking, obesity, diabetes or family's cancer cases, but only in few patients these factors are identifiable[205]. One of the most widely used drug for this tumor is gemcitabine applied as a monotherapy[206]. More recently, the use of gemcitabine has been combined with Folfirinox and nab-paclitaxel[207], prolonging the survival of patients by only a few months. The best option is the early tumour surgical resection, as therapeutic treatments fail for the presence of metastases and high local recurrence[208]. Therefore, developing novel therapeutic strategies for this fatal disease is urgently needed.

In the pancreatic tumour microenvironment there is a huge proliferation of stromal cells such as tumour associated macrophages (TAMs), regulatory T cells (T_{regs}), mast cells and pancreatic stellate cells (PSc) that support tumour growth, while immune cells such as natural killer (NK) and T CD8$^+$ are down regulated[209]. Only at early stage of the disease, it is possible to find several immune cell populations in an active state in the tumour microenvironment (TME), then they are mostly deactivated or exhausted in order to inhibit anti-tumour function[210]. Cytotoxic T lymphocytes, also known as T CD8$^+$, can kill tumour cells using perforin and granzyme. In patients affected by pancreatic carcinoma, analysis in peripheral blood shown a great reduction in circulating CD8$^+$ T cells with lower perforin levels compared to healthy controls[211]. Immunohistochemistry analyses on pancreatic carcinoma samples showed that higher levels of tumour infiltrating CD4$^+$ and CD8$^+$ T cells

are associated with longer survival[212]. However, PDAC cells express programmed cell death receptor ligand (PD-L1), which binds to PD-1 expressed on activated T cells[213]. Normally, PD-L1 works as immune checkpoint protein, ensuring that, by binding PD-1, healthy cells are not harmed and that the immune system is activated only at the appropriate time, avoiding autoimmune responses[214]. The expression of PDL-1 on PDAC cells leads to the T cells exhaustion or their death and, consequently, promotes the tumour progression[215]. Another T cell subset, the $CD4^+$ T helper cells, plays an important role, secreting several cytokines that modulate T and B cells function. Again, in patients with pancreatic cancer, peripheral blood levels of T $CD4^+$ cells are reduced compared to healthy controls[215]. Investigating on the T cell infiltration in PDAC, and understanding how to restore the functionality of exhausted T cells is one of the main therapeutic goals to defeat this type of cancer.

Another key component in the pancreas are PSc, involved in the maintenance of tissue homeostasis[216]. During a pancreatic lesion, the quiescent PSc are activated and transformed into cells similar to myofibroblasts that secrete proteins of the extracellular matrix, generating fibrosis. Indeed, PDAC is characterized by a desmoplastic reaction that lead to an increase in the proliferation of α-smooth muscle actin (α-SMA)-positive fibroblasts. This reaction makes pancreatic cancer impenetrable to pharmaceutical treatments, as well as to the immune system, thus favouring its progression[204-217]. PSCs also release cytokines, including CXCL12 which may lead to the reduction of $CD8^+$, $CD4^+$, NK and T_{regs} cells migration[216]. The release of Galectin-1 by PSc may also cause $CD8^+$ T cell immunosuppression and apoptosis[218]. These data point out the importance of understanding the role of pancreatic stellate cells in pancreatic cancer immunotherapy.

In recent years, the immunotherapy has shown a significant promise where other approaches have failed[219]. There are 3 types of immunology-based therapies: (i) therapeutic vaccines to stimulate the immune system to produce T-cells and tumor-specific B cells[220]; (ii) adopted therapy, where T $CD8^+$ cells, expanded *ex vivo*, are injected into the tumor to kill cancer cells[221]; and (iii) immune checkpoint inhibitors, that unfortunately are ineffective in PDAC[222]. Therefore, despite the innumerable advances

in these applications, still there are hurdles to overcome to achieve a successful therapy. Fast reproducible models are needed to improve the preclinical studies. Murine models are complex, expensive and time-consuming, and the *in vitro* 2D tumor models, as already described, fail to mimic the structure of the native 3D tissue or the surrounding tumor microenvironment. Once again, 3D *in vitro* models overcome the disadvantages of animal models in terms of scalability, cost and ease of use, and offer the possibility of studying the role of TME in a more physiological condition than the simple 2D approach. For example, cancer cells grown in 3D hydrogels represent a way to study interactions with lymphocytes[223] in a condition more comparable to the *in vivo* microenvironment. Among the 3D models, microfluidic devices are those that can best reproduce the conditions necessary to study dynamic processes such as cell adhesion, cell migration and cell-cell interactions, CCL21 and CCL19 2D chemotaxis of T cells [224], or the chemotaxis of tumor cells and immune cells in 3D collagen gel. Microfluidic devices were also used to study melanoma growth in the presence of the immune system cells[106]. Bai et al., instead, investigate the role of macrophages in lung adenocarcinoma doing studies on modelling and screening of different therapeutic approaches. This microfluidic platform was key to identify the role of each subtype of macrophages in lung tumor aggregate dispersion[225]. Arcangeli's group has developed a microfluidic platform that, in combination with dielectrophoresis, allowed to culture different pancreatic ductal adenocarcinoma human cell lines maintaining cell vitality, morphological appearance and growth characteristics that more closely resemble 3D cultures[226]. As a result, 3D microfluidic tumour models would be useful in the screening of immunotherapy strategies in a more physiologically relevant TME and with control over the spatial cellular organization.

My research project in collaboration with Adriani's group in Singapore, focused on a 3D multicellular microfluidic assay to analyze the T cell infiltration across the vasculature in a pancreatic adenocarcinoma model, recapitulating key features of the immune microenvironment, such as chemical gradients, vascular flow and trans-endothelial migration. The device used consist of a three

channel microfluidic chip composed by 3D gel region, flanked by 2 media channels connected by a series of trapezoidal pillars (**Figure.5.1**). The two lateral compartments are used to simulate the vascular and stromal environment respectively. Indeed, the central channel is coated by cancer cells embedded in a collagen matrix, reproducing the malignant tissue. The trapezoidal pillars allow the separation of the different compartments, still maintaining a connection between them.

5.2 MATERIAL AND METHODS

Cells type

Human Umbilical Vein Endothelial cells HUVECs were purchased from Lonza, used until passage 6, cultured in a T25 and T75 flasks in the Endothelial growth media EGM, until reaching the 70% confluency. Pancreatic ductal adenocarcinoma cells PANC-1 and pancreatic stellate cells (PSc) were purchased from Lonza and cultured in DMEM media with 1% Pen/Strept, 1% Glutamax and 10% FBS. Cells were used until passage 20.

AIM chip technology

The AIM chip is a commercialized device by AIM Biotech (www.aimbiotech.com). The chip is made by Polydimethylsyloxane (PDMS), and consists of two lateral channels and a central region divided by an array of trapezoidal pillars. The devices presents a height (h) of 250 µm and a width (w) of 25 mm.

Collagen gel preparation and cells seeding

The collagen gel was prepared mixing 10x PBS with phenol red (Life technologies), 0.5 M NaOH (Sigma Aldrich), sterile deionized water (Thermo Water purifying System) and Collagen type I from rat tail (Corning Life Science). The final collagen concentration used was 3 mg/mL. $1x10^6$ PANC-1 cells, embedded in a collagen matrix, were seeded in the central chamber of the device. To avoid the drying of the gel, 6 mL of sterile water was added into the reservoirs of the AIM holders. After the collagen jellification occurred after 30 minutes at 37 ˚C, the media channel were hydrated adding 20 µL of cell culture media and then coated with 50 µg/mL fibronectin, injected in one of the two lateral channel and incubated for 1h at 37 ˚C. Then, $3x10^6$ GFP$^+$ HUVECs were introduced in the same compartment to form a full endothelial monolayer.

PSc cells ($1x10^6$) were introduced in the opposite lateral channel, and medium was changed daily.

Panc-1 cells were stained in orange with the Cell Tracker Orange dye CMRA.

Immunofluorescence staining and image acquisition

At the end of the experiments, each compartment was washed with PBS and fixed with 4% paraformaldehyde (PFA) (Sigma Aldrich) for 15 minutes at room temperature. After washing twice with PBS, channels were filled with a 0.1% Triton X-100 (Sigma Aldrich) in PBS solution for 10 min at room temperature to allow cellular membrane permeation. Next, cells were incubated with BSA 3% (Life technologies) for 2h at room temperature and then human endothelial Cadherins were targeted overnight (4 ℃) using anti-human VE-Cadherin antibody (Ms anti-human Ve-cadherin, 1:100, Enzo technology). Afterwards, devices were incubated with red fluorescent dye-labeled secondary antibody (anti-mouse 647, 1:500, Enzo technology) for 1h at room temperature. Cell nuclei were stained with DAPI (5 mg/mL, Invitrogen). Images were acquired using confocal microscope (Olympus).

Permeability experiments in the AIM chip

During the permeability tests, 70 kDa FITC-Dextran (Sigma Aldrich) was added up to a concentration of 100 µg/mL. For all the experiments, devices were previously fixed in PFA 4%. Dextran permeability was detected using a fluorescent inverted microscope (EVOS). The analysis of Dextran permeability was done by ImageJ software using six adjacent ROIs, three from the vascular channel and the other three from the gel channel. Briefly, to estimate the permeability, it was used the equation

$$P = \frac{(I_f - I_i)w}{(I_i - I_b)\Delta t}$$

where P is the diffusive permeability (µm/s), I_f is the total fluorescent intensity in the two ROIs at the final analyzed frame, I_i is the total fluorescent intensity in the two ROIs at the initial analyzed frame. I_b is the total fluorescent intensity in the extravascular ROI at the initial analyzed frame. Δt is the time difference between the analyzed frame, and w is the width of the vascular channel.

Isolation of human T cells

T cells were obtained collecting human blood from healthy donors into standard blood tubes. Peripheral blood mononuclear cells (PBMCs) were isolated by density gradient centrifugation (Ficoll-Paque™). The platelets were removed by density gradient separation, and then the pellet was resuspend in a buffer solution and centrifuged. Then, a positive selection for the T cells, using a CD3$^+$ magnetic beads, was performed. Shortly, the CD3$^+$ cells were magnetically labeled with CD3$^+$ Microbeads, and then the cell suspension was loaded onto a MACS® Column (Mylteni) which was placed in the magnetic field of a MACS Separator. The magnetically labeled CD3$^+$ cells were retained on the column. The unlabeled cells run through the column and this cell fraction was depleted of CD3$^+$ cells. After removal of the column from the magnetic field, the retained CD3$^+$ cells were eluted as the positively selected cell fraction.

T cell activation with dynabeads

At the occurrence, T cells were activated with CD3/CD28 dynabeads (Thermofisher). Dynabeads were resuspended in a 1 mL vial, vortex for 30 sec and transferred in a desired volume. (1.25 µl for 10^5 cells). Then, the vial was placed in a magnetic field for 1 min and the supernatant was discarded. Dynabeads were added to the purified population of T cells for 5 days at 37˚C in a T75 flask with 30 U/ml of IL-2 in RPMI medium. After 3 days of incubation the viable cell density were adjusted by adding fresh complete medium (RPMI+ IL-2). After 5 days, dynabeads were removed using the magnetic field and finally T cells were inserted in the AIM chip.

T cells seeding

T cells were collected from the culture flasks and were stained in blue with Violet tracker (Cell Tracker dye). 30 µl of T cell suspension (8 x 10^6 cell/mL) were added in the vascular channel filled

with HUVECs; 20 µl of media were removed from the opposite outlet to allow the movement of the T cells in the gel channel where pancreatic cancer cells were seeded. Then chips were maintained in incubator at 37˚C for 24 and 48 h before the image acquisition made by Opera Phenix. The images were analyzed by IMARIS software.

Fluorescence activated cell sorting

Cell suspension was adjusted at the concentration of 1×10^6 cell/mL in cold FACS buffer. Conjugated primary antibodies (1:500) were added to the cell suspension for 20 min at 4 ºC in the dark. Then, cells were washed once by 5 min centrifugation and resuspended in 200 µl of PFA 2% for 40 min at room temperature in the dark. Cells were washed using FACS buffer and kept in the dark until the analysis was performed. Finally, cells were incubated with anti-human mABs for CD4 (APC 780), CD8 (PE), CD3 (APC, FITC), and PD1 (Texas Red), from Thermofisher. Cell fluorescence was measured using a Fortessa LSR BD and data analyzed using Flowjo software.

5.3 RESULTS AND DISCUSSION

Pancreatic tumor model and vascular permeability modeling. To study the T cell infiltration process in the PDAC, a microfluidic chip provided by *Biotech* (**Figure.5.1a** and **b**) was used. Briefly, AIM device is composed of three parallel channels, whose height is 120 μm, separated by 100 μm. Panc-1 cells were seeded in the central compartment, 1 mm wide, completely embedded into 3D collagen type I matrix. Lateral channels have a width of 500 μm and were seeded with endothelial cells (HUVECs) to form a biomimetic blood vessel, and pancreatic stellate cells (PSc) to mimic the structure of the exocrine region of the pancreas (**Figure.5.1c**).

To characterize the function of the endothelial barrier, after 2 days from the HUVECs seeding, 70 kDa fluorescein isothiocyanate dextran (RFP-dextran) was injected in the vascular channel and the diffusion of the tracer into the gel compartment was analyzed to evaluate for the vascular permeability P.
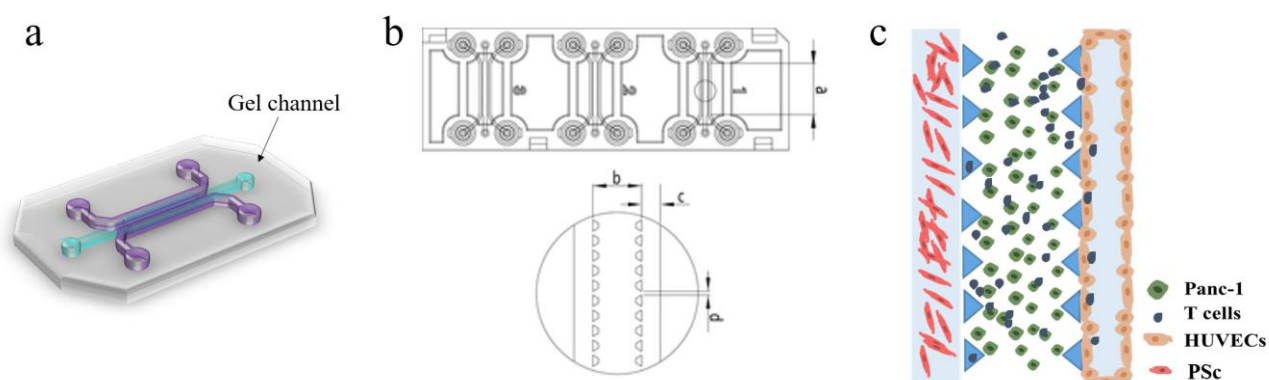
Figure 1. Microfluidic pancreatic tumor model. a. Schematic representation of AIM chip; **b.** Image of AIM slide (75 mm x 25mm) bringing 3 chips. a: length of the channel; b: width of the channel; c: width of the media channels; d: gap between posts. **c.** PDAC schematic showing 3D gel region flanked by 2 media channels, divided by a trapezoidal pillars, Panc-1 cells (green), T cells (blue), HUVECs cells (pink) and Fibroblasts (red).

Representative confocal fluorescent images of the endothelial cells forming a vessel are reported in **Figure.5.2a**. The fluorescent images in **Figure.5.2b** document the permeation of the tracer in the

extravascular space at 3 different time points, namely 5, 15 and 30 min post infusion. The obtained permeability values is 0.27 ± 0.17 µm/s.
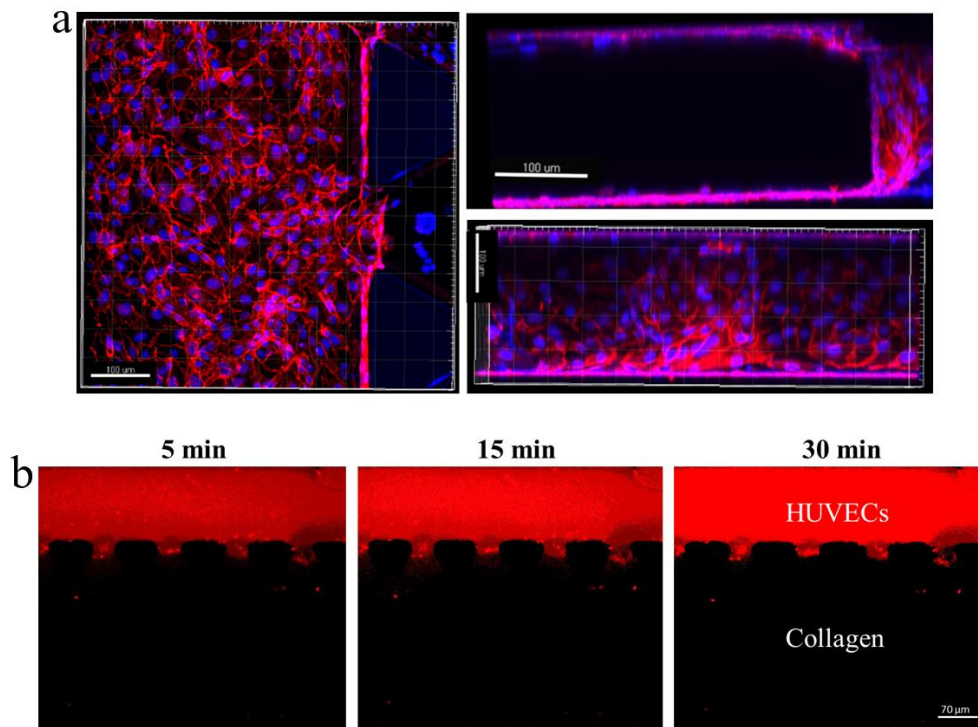
$$P = \frac{(I_f - I_i)w}{(I_i - Ib)\Delta t} = 0.27 \pm 0.17 \ \mu m/s$$

Figure 5.2. Microfluidic vascular model. **a.** Confocal Z stack images depicting VE-cadherin and DAPI staining to show the confluency of the endothelial monolayer. Scale bar is 100 µm. **b.** Characterization of endothelial permeability. Representative fluorescent images of free RFP-Dextran (70 kDa) diffusing in the vascular channel covered with a confluent HUVEC monolayer. At the bottom, it is indicated the formula used to estimate the vascular permeability. Scale bar is 70 µm.

The permeability value is in line with *in vitro* data reported by other authors[100], and demonstrate the ability to modulate the vascular permeability in the AIM chip.

T cell infiltration in PDAC tumor. As to perform their antitumor function T cell have to migrate from blood into tissues, the AIM chip was used to assess the ability of T cell to infiltrate within

PDAC. The 3D microdevice was seeded in the central chamber with Panc-1 cells embedded in a collagen type I matrix, while the side channels were covered by HUVECs cells, forming a confluent monolayer and pancreatic stellate cells. T cells collected from human blood of healthy donors were injected into the vascular lateral channel, covered by HUVECs, in contact with the collagen region. T cell activation was obtained stimulating them with dynabeads. These polystyrene spherical particles are covered with antibodies against CD3, a key signaling component of the T cell receptor (TCR) complex, and CD28 receptors, which provides a costimulatory signal essential for functional activation. Dynabeads were first developed by Professor John Ugelstad and can be used for the positive or negative selection of different samples from biological material[227]. In this specific case, T cell were positive selected from human peripheral blood mononuclear cell (PBMC) and cultured for 5 days in RPMI medium with IL-2 and dynabeads. For each experiment, T cell population was divided in T cell activated and T cell not activated, indicating cells not stimulated with dynabeads. The activation of T cells was verified by flow cytometry using as activation marker the PD-1 molecule, in comparison to T cell stimulated with dynabeads for 5h (**Figure.5.3**).

PD-1

■ T cell without dynabeads (5h)
■ T cell activated with dynabeads (5h)
■ T cell activated with dynabeads (5 days)
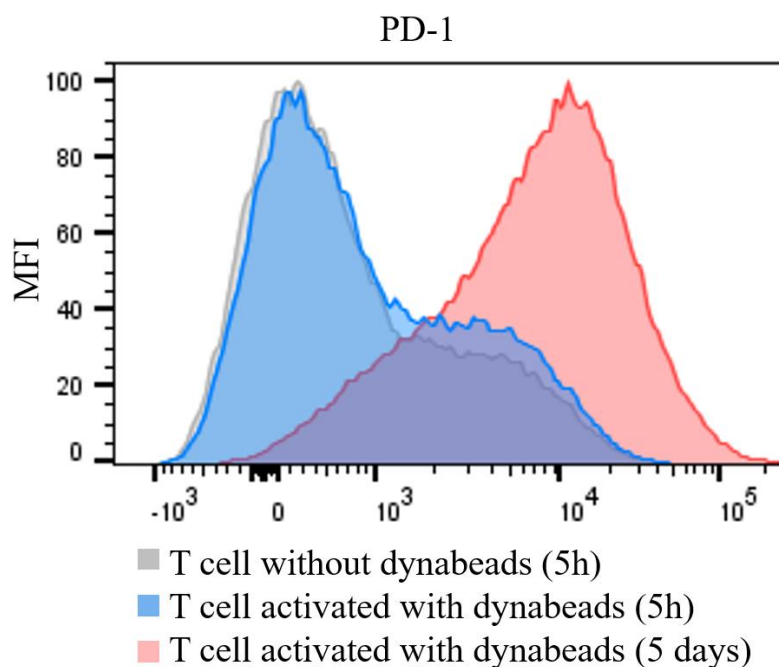
Figure.5.3. T cell activation status. PD-1 expression on T cells not activated (without dynabeads) and T cell activated with dynabeads, maintained in culture for 5 hours or 5 days in RPMI medium and IL-2 (30 U/mL). Average geometric mean fluorescence intensity (MFI) of PD-1 is reported. Data are representative of three independent experiments.

The following antigens were used as markers for detecting each T cell subset: CD3, CD4, CD8 (data not shown). Both T cell populations, activated and not activated, were injected into the HUVEC compartment after the monolayer formation at 8×10^6 cell/ml.

To better clarify the more relevant factors involved in T cells infiltration in the pancreatic tumor microenvironment, the T cell infiltration was quantitatively evaluated as a function of the level of T cells activation status, presence of endothelial barrier, and tumor microenvironment. Therefore, the analyses were performed in in six different experimental conditions:

1. Tumour (Panc-1 cells seeded in the collagen gel, PSC and HUVECs seeded in the side channels);

2. No PSc (Panc-1 seeded in the collagen gel and HUVECs in a lateral channel);

3. No HUVEC (Panc-1 cells seeded in the collagen gel and PSc seeded in a lateral channel);

4. Only Panc-1 (Panc-1 cells seeded in the collagen gel);

5. Only PSc (PSc seeded in one lateral channel);

6. PSc + H (HUVECs and PSc seeded in the side channels, while the central chamber was filled only with collagen).
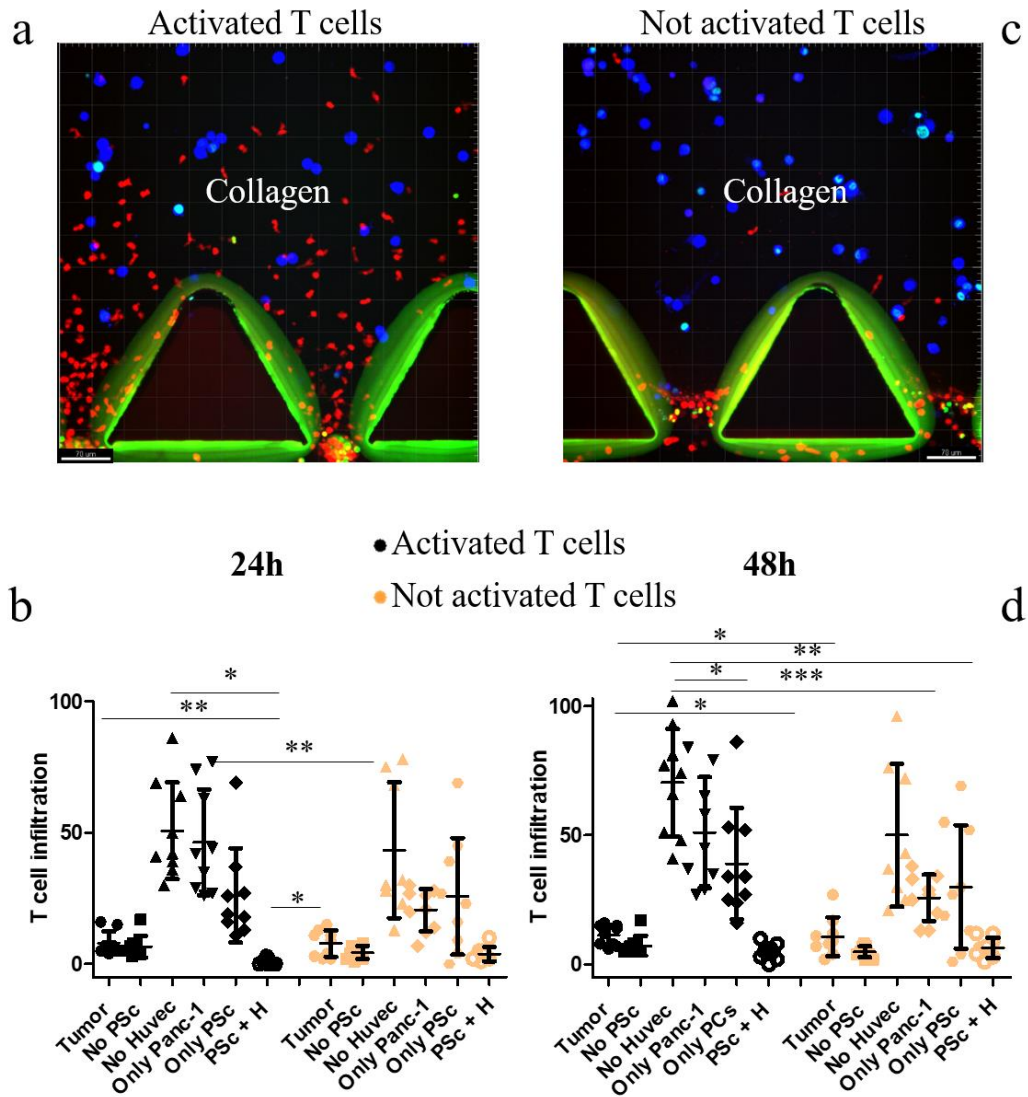
Figure 5.4. T cell infiltration in PDAC model. a. Representative confocal microscopy images of activated T cells (labeled in red with CTV) infiltrating in the central channel filled with Panc-1 cells (stained in blue with CMRA) embedded in a collagen gel. **b.** Absolute number of adhering infiltrating T cell (after 24h from their injection) with and without stimulation with dynabeads for 5 days. **c.** Representative confocal microscopy images of T cells not activated (labeled in red with CTV) infiltrating in the central channel filled with Panc-1 cells (stained in blue with CMRA) embedded in a collagen gel. **d.** Absolute number of adhering infiltrating T cell (after 48h from their injection) with and without stimulation with dynabeads for 5 days. (Statistical analysis ANOVA: *** symbol denotes statistically significant difference p < 0.0001; ** symbol denotes statistically significant difference p < 0.001. (n = 2).

Via confocal microscopy, the number of infiltrating T cells, in the gel compartment, was quantified after 24 and 48h from injection in nine different regions of interest (ROIs) along the channel.

Results as number of T cells infiltrated in a collagen gel after 24 and 48h from their injection are provided in **Figure.5.4b** and **d**, respectively. On the left hand side, **Figure.5.4a and c**, representative confocal microscopy images are shown for activated and not activated T cells. Significant differences arose when considering T cell infiltration after stimulation with dynabeads and not stimulated T cells. At 24 h, the absolute number of infiltrating T cells was, respectively, 8.111 ± 4.343 and 7.778 ± 5.069 in "tumor" condition, 6.667 ± 4.153 and 4.444 ± 2.506 in "No PSc condition"; 50.78 ± 18.40 and 43.38 ± 25.88 in "No Huvec" condition; 46.33 ± 20.07 and 20.56 ± 8.033 in "only Panc-1" condition; 26.22 ± 17.95 and 25.78 ± 22.19 in "only PSc" condition; 1.000 ± 1.118 and 3.778 ± 2.728 in "PSc + H" condition. At 48 h, the absolute number of infiltrating T cells was, respectively, 9.952 ± 1.803 and 10.24 ± 2.841 in "tumor" condition, 29.09 ± 2.219 and 28.54 ± 5.038 in "No PSc condition"; 40.37 ± 9.205 and 40.26 ± 3.521 in "No Huvec" condition; 9.952 ± 1.803 and 10.24 ± 2.841 in "only Panc-1" condition; 9.952 ± 1.803 and 10.24 ± 2.841 in "only PSc" condition; 9.952 ± 1.803 and 10.24 ± 2.841 in "PSc + H" condition. As compared to the not activated T cells, T cell infiltrate more when stimulated with dynabeads. Maximum infiltration is observed for all the conditions in which the HUVEC monolayer is not present, confirming the stability of the endothelial barrier formed in the device. Conversely, in all the conditions with empty vascular channel the number of infiltrating T cell increases. Maximum infiltration is reported in the "No Huvec" condition with stimulated T cells, indicating that both Panc-1 cells and pancreatic stellate cells are able to modulate the T cells recruitment into PDAC.

5.4 CONCLUSION AND FUTURE DEVELOPMENTS

The results obtained with the AIM-chip platform indicate that this device can be efficiently used for characterizing the T cell infiltration in the pancreatic tumor, as well as other type of solid tumors, reproducing a more realistic 3D tumor model over classical 2D platforms. Moreover, it was able to recapitulate key features of the immune microenvironment, such as vascular flow and trans-endothelial migration. The 3D microfluidic *in vitro* tumor microenvironment (TME) more closely mimics the physiological *in vivo* setting as the Panc-1 cells are in a 3D matrix and T cells migrate from a blood vessel toward the tumor mass. AIM chip technology could not only help to characterize the immune-cancer cell interactions that have recently become interesting therapeutic targets, but also help in testing the efficacy of novel immunotherapies.

This technology could pave the way to go deeper in the study of the key factors involved in pancreatic tumor progression and survival. For instance, it would be very interesting to characterize the activation and exhaustion markers on T cells infiltrated in the tumor mass, in order to explain why some T cells fail to infiltrate into tumor mass and, consequently, to exert a proper immune surveillance.

By checking for the presence of immune inhibitory cytokines released from HUVEC cells or PSc, it could be possible to understand the immune regulatory potential of endothelial cells and PSc in protecting the tumor against T cell infiltration. Finally, the chip could help in understanding the behavior of naïve T cells that reach the tumor channel, enriched also with antigen-presenting cells (APC).

6. CONCLUDING REMARKS

The last decades have been distinguished for important progress in cancer treatment, also based on the characterization of its intricate metastasis formation mechanism and on the role of immune system in its development. The previous information obtained in 2D models have been integrated into more complex 3D models, and with the emerging of microfluidics, novel devices can now better reproduce the interaction among tumor cells, immune cells and the microenvironment. Several chips have been designed to mimic the extravascular environment incorporating 3D matrix (collagen, matrigel, hyaluronic acid), allowing the analysis of the cellular dynamics, the cellular movements and cell deformability. Significant progresses have been made since the development of soft lithography techniques, which allow the realization of micrometric structures made of polymeric materials such as poly-dimethyl-siloxane (PDMS), one of the most commonly used materials for the fabrication of microfluidic devices, like the ones I used in my studies.

In my first project using a single channel microfluidic chip, I studied the vascular transport of circulating tumor cells under different biophysical conditions, as level of inflammation, flow rate, and working fluid (physiological solution and whole blood). The obtained results suggest that, within microvascular networks, blood rheology and inflammation contribute similarly to CTC deposition, thereby facilitating the formation of metastatic niches along the entire network, including the healthy endothelium. In microfluidic-based assays, neglecting blood rheology would significantly underestimate the metastatic potential of cancer cells.

In the second work, I was able to mimic all the key steps of the metastatic cascade, using a microfluidic chip presenting two channels connected via an array of pillars to form a permeable micromembrane. One channel acted as a vascular compartment, by the coating of a fully confluent monolayer of endothelial cells, whereas the other channel was filled with a mixture of matrigel and breast cancer cells. The vascular permeability was modulated by inducing pro-inflammatory conditions in the tissue

compartment, which transiently opened up the tight junctions of endothelial cells, demonstrating that the proposed chip could efficiently replicate *in vitro*, under controlled biophysical and biochemical conditions, the multiple key steps in the cancer metastatic cascade.

In the last part of this thesis is reported the use of a microfluidic platform to study the interactions between tumor and immune cells, that is an highly dynamic process and it is critical for the success of cancer immunotherapies. Specifically, I studied the process of T cell infiltration in pancreatic tumor, using a PDMS customized microfluidic chip, comprising two lateral compartments, one mimicking the vasculature and the other filled with stromal cells (pancreatic stellate cells), and one central chamber, used to mimic the malignant tissue. This microfluidic device prove to be useful in the study of T cell migration toward the tumor.

In conclusion, microfluidics provided a great advancement in the biomedical field. Indeed, these devices make possible to study all the steps involved in tumor metastatization, as well as immune system migration toward tumor mass. In addition, microfluidic devices allow the study of tumor spheroids as well as of more complicate multi-cellular system, dissecting the role and contribution of each one of them in this process. Importantly, only microfluidics could take into account the big role of the fluid flows in dynamic processes that involve the passage in and out of the vasculature. These steps forward could efficiently allow the screening of therapeutic molecules and drugs, also regarding their targeting and distribution within the engineered tissue. The data obtained could grant the ability to choose the best drug for the treatment of the analyzed specimen, in a real personalized medicine approach, and thus could be rapidly translated in the clinics, improving patients' life.

LIST OF PUBBLICATIONS

G. Palazzolo, **H. Mollica**, V. Lusi, M. Rutigliani, M. Di Francesco, R. Cruz Pereira, M. Filauro, L. Paleari, A. DeCensi, P. Decuzzi. «*Modulating the distant spreading of patient derived colorectal cancer cells via aspirin and metformin*». Cancer Letters (submitted), February **2020**

Daniele Di Mascolo, Serena Varesano, Roberto Benelli, **Hilaria Mollica**, Annalisa Salis, Maria Raffaella Zocchi, Paolo Decuzzi and Alessandro Poggi "Nanoformulated Zoledronic Acid Boosts Vδ2 T Cell Immunotherapeutic Potential in Colorectal Cancer". Cancers, December **2019**

H. Mollica, R. Palomba, R. Primavera, & P. Decuzzi "Two-Channel Compartmentalized Microfluidic Chip for Real-Time Monitoring of the Metastatic Cascade". ACS Biomaterials Science & Engineering, July **2019**

M. Colasuonno, A.L. Palange, R. Aid, M. Ferreira, **H. Mollica**, R. Palomba, M. Emdin, M. Del Sette, C. Chauvierre, D. Letourneur , P. Decuzzi. "Erythrocyte-Inspired Discoidal Polymeric Nanoconstructs Carrying Tissue Plasminogen Activator for the Enhanced Lysis of Blood Clots". ACS Nano, November **2018**

H. Mollica, A. Coclite, M.E. Miali, R.C. Pereira, L. Paleari, C. Manneschi, A. De Censi, P. Decuzzi.*"Deciphering the relative contribution of vascular inflammation and blood rheology in metastatic spreading".* Biomicrofluidics, May **2018**.

Coclite, **H. Mollica**, S. Ranaldo, G. Pascazio, M.D. De Tullio, P. Decuzzi. *"Predicting different adhesive regimens of circulating particles at blood capillary walls".* Microfluidics and Nanofluidics, October **2017**.

AWARDS AND CONFERENCES
Poster Section at Engineering Conferences International, Albufeira, Portugal, 5-9 June 2018.
H. Mollica, Roberto Palomba, R.C. Pereira, C. Manneschi, P. Decuzzi "*A microfluidic platform with permeable walls for the analysis of vascular and extravascular mass transport*"

First Prize winner 2017 – Poster Section at European Foundation for Clinical Nano-medicine, Basel Switzerland 7-10 May. **H. Mollica***, V. Lusi*, A. Cervadoro, M.E. Miali, M. Colasuonno, R.C. Pereira, C. Manneschi, P. Decuzzi "*Microfluidic chips for the vascular and extravascular transport analysis of molecules, nanoparticles and cells*"

REFERENCES

1. Paget, S., The distribution of secondary growths in cancer of the breast. *The Lancet* **1889,** *133* (3421), 571-573.

2. Gregory, P. A.; Bert, A. G.; Paterson, E. L.; Barry, S. C.; Tsykin, A.; Farshid, G.; Vadas, M. A.; Khew-Goodall, Y.; Goodall, G. J., The miR-200 family and miR-205 regulate epithelial to mesenchymal transition by targeting ZEB1 and SIP1. *Nature cell biology* **2008,** *10* (5), 593.

3. Steeg, P. S., Targeting metastasis. *Nature reviews cancer* **2016,** *16* (4), 201.

4. Sahai, E., Illuminating the metastatic process. *Nature reviews cancer* **2007,** *7* (10), 737.

5. Xu, J.; Lamouille, S.; Derynck, R., TGF-β-induced epithelial to mesenchymal transition. *Cell research* **2009,** *19* (2), 156.

6. Dongre, A.; Weinberg, R. A., New insights into the mechanisms of epithelial–mesenchymal transition and implications for cancer. *Nature reviews Molecular cell biology* **2019,** *20* (2), 69-84.

7. Lamouille, S.; Xu, J.; Derynck, R., Molecular mechanisms of epithelial–mesenchymal transition. *Nature reviews Molecular cell biology* **2014,** *15* (3), 178.

8. Fan, F.; Samuel, S.; Evans, K. W.; Lu, J.; Xia, L.; Zhou, Y.; Sceusi, E.; Tozzi, F.; Ye, X. C.; Mani, S. A., Overexpression of Snail induces epithelial–mesenchymal transition and a cancer stem cell–like phenotype in human colorectal cancer cells. *Cancer medicine* **2012,** *1* (1), 5-16.

9. Long, H.; Xiang, T.; Qi, W.; Huang, J.; Chen, J.; He, L.; Liang, Z.; Guo, B.; Li, Y.; Xie, R., CD133+ ovarian cancer stem-like cells promote non-stem cancer cell metastasis via CCL5 induced epithelial-mesenchymal transition. *Oncotarget* **2015,** *6* (8), 5846.

10. Rasheed, Z. A.; Yang, J.; Wang, Q.; Kowalski, J.; Freed, I.; Murter, C.; Hong, S.-M.; Koorstra, J.-B.; Rajeshkumar, N.; He, X., Prognostic significance of tumorigenic cells with mesenchymal features in pancreatic adenocarcinoma. *Journal of the National Cancer Institute* **2010,** *102* (5), 340-351.

11. Kong, D.; Banerjee, S.; Ahmad, A.; Li, Y.; Wang, Z.; Sethi, S.; Sarkar, F. H., Epithelial to mesenchymal transition is mechanistically linked with stem cell signatures in prostate cancer cells. *PloS one* **2010,** *5* (8), e12445.

12. Zhou, D.; Kannappan, V.; Chen, X.; Li, J.; Leng, X.; Zhang, J.; Xuan, S., RBP2 induces stem-like cancer cells by promoting EMT and is a prognostic marker for renal cell carcinoma. *Experimental & molecular medicine* **2016,** *48* (6), e238.

13. Singh, A.; Settleman, J., EMT, cancer stem cells and drug resistance: an emerging axis of evil in the war on cancer. *Oncogene* **2010,** *29* (34), 4741.

14. Chung, Y. C.; Wei, W. C.; Hung, C. N.; Kuo, J. F.; Hsu, C. P.; Chang, K. J.; Chao, W. T., Rab11 collaborates E-cadherin to promote collective cell migration and indicates a poor prognosis in colorectal carcinoma. *European journal of clinical investigation* **2016,** *46* (12), 1002-1011.

15. Gaggioli, C.; Hooper, S.; Hidalgo-Carcedo, C.; Grosse, R.; Marshall, J. F.; Harrington, K.; Sahai, E., Fibroblast-led collective invasion of carcinoma cells with differing roles for RhoGTPases in leading and following cells. *Nature cell biology* **2007,** *9* (12), 1392.

16. Khoo, B. L.; Lee, S. C.; Kumar, P.; Tan, T. Z.; Warkiani, M. E.; Ow, S. G.; Nandi, S.; Lim, C. T.; Thiery, J. P., Short-term expansion of breast circulating cancer cells predicts response to anti-cancer therapy. *Oncotarget* **2015,** *6* (17), 15578.

17. Lambert, A. W.; Pattabiraman, D. R.; Weinberg, R. A., Emerging biological principles of metastasis. *Cell* **2017,** *168* (4), 670-691.

18. Rapoport, A.; Abboud, C.; DiPersio, J., Granulocyte-macrophage colony-stimulating factor (GM-CSF) and granulocyte colony-stimulating factor (G-CSF): receptor biology, signal transduction, and neutrophil activation. *Blood reviews* **1992,** *6* (1), 43-57.

19. Chang, H. Y.; Sneddon, J. B.; Alizadeh, A. A.; Sood, R.; West, R. B.; Montgomery, K.; Chi, J.-T.; Van De Rijn, M.; Botstein, D.; Brown, P. O., Gene expression signature of fibroblast serum

response predicts human cancer progression: similarities between tumors and wounds. *PLoS biology* **2004,** *2* (2), e7.

20. Kang, Y.; Pantel, K., Tumor cell dissemination: emerging biological insights from animal models and cancer patients. *Cancer cell* **2013,** *23* (5), 573-581.

21. Aceto, N.; Bardia, A.; Miyamoto, D. T.; Donaldson, M. C.; Wittner, B. S.; Spencer, J. A.; Yu, M.; Pely, A.; Engstrom, A.; Zhu, H., Circulating tumor cell clusters are oligoclonal precursors of breast cancer metastasis. *Cell* **2014,** *158* (5), 1110-1122.

22. Aceto, N.; Toner, M.; Maheswaran, S.; Haber, D. A., En route to metastasis: circulating tumor cell clusters and epithelial-to-mesenchymal transition. *Trends in cancer* **2015,** *1* (1), 44-52.

23. Labelle, M.; Hynes, R. O., The initial hours of metastasis: the importance of cooperative host–tumor cell interactions during hematogenous dissemination. *Cancer discovery* **2012,** *2* (12), 1091-1099.

24. Palumbo, J. S.; Talmage, K. E.; Massari, J. V.; La Jeunesse, C. M.; Flick, M. J.; Kombrinck, K. W.; Jirousková, M.; Degen, J. L., Platelets and fibrin (ogen) increase metastatic potential by impeding natural killer cell–mediated elimination of tumor cells. *Blood* **2005,** *105* (1), 178-185.

25. Kopp, H.-G.; Placke, T.; Salih, H. R., Platelet-derived transforming growth factor-β down-regulates NKG2D thereby inhibiting natural killer cell antitumor reactivity. *Cancer research* **2009,** *69* (19), 7775-7783.

26. Baccelli, I.; Schneeweiss, A.; Riethdorf, S.; Stenzinger, A.; Schillert, A.; Vogel, V.; Klein, C.; Saini, M.; Bäuerle, T.; Wallwiener, M., Identification of a population of blood circulating tumor cells from breast cancer patients that initiates metastasis in a xenograft assay. *Nature biotechnology* **2013,** *31* (6), 539.

27. Kunkel, E. J.; Butcher, E. C., Chemokines and the tissue-specific migration of lymphocytes. *Immunity* **2002,** *16* (1), 1-4.

28. Reymond, N.; d'Agua, B. B.; Ridley, A. J., Crossing the endothelial barrier during metastasis. *Nature Reviews Cancer* **2013,** *13* (12), 858.

29. Al-Mehdi, A.; Tozawa, K.; Fisher, A.; Shientag, L.; Lee, A.; Muschel, R., Intravascular origin of metastasis from the proliferation of endothelium-attached tumor cells: a new model for metastasis. *Nature medicine* **2000,** *6* (1), 100.

30. Karrison, T. G.; Ferguson, D. J.; Meier, P., Dormancy of mammary carcinoma after mastectomy. *Journal of the National Cancer Institute* **1999,** *91* (1), 80-85.

31. Ghajar, C. M., Metastasis prevention by targeting the dormant niche. *Nature Reviews Cancer* **2015,** *15* (4), 238-247.

32. Ghajar, C. M.; Peinado, H.; Mori, H.; Matei, I. R.; Evason, K. J.; Brazier, H.; Almeida, D.; Koller, A.; Hajjar, K. A.; Stainier, D. Y., The perivascular niche regulates breast tumour dormancy. *Nature cell biology* **2013,** *15* (7), 807.

33. Balkwill, F.; Montfort, A.; Capasso, M., B regulatory cells in cancer. *Trends in immunology* **2013,** *34* (4), 169-173.

34. Coley, W. B., The treatment of malignant tumors by repeated inoculations of erysipelas: with a report of ten original cases. 1. *The American Journal of the Medical Sciences (1827-1924)* **1893,** *105* (6), 487.

35. Boon, T.; Cerottini, J.-C.; Van den Eynde, B.; van der Bruggen, P.; Van Pel, A., Tumor antigens recognized by T lymphocytes. *Annual review of immunology* **1994,** *12* (1), 337-365.

36. Galon, J.; Costes, A.; Sanchez-Cabo, F.; Kirilovsky, A.; Mlecnik, B.; Lagorce-Pagès, C.; Tosolini, M.; Camus, M.; Berger, A.; Wind, P., Type, density, and location of immune cells within human colorectal tumors predict clinical outcome. *Science* **2006,** *313* (5795), 1960-1964.

37. Mahmoud, S. M.; Paish, E. C.; Powe, D. G.; Macmillan, R. D.; Grainge, M. J.; Lee, A. H.; Ellis, I. O.; Green, A. R., Tumor-infiltrating CD8+ lymphocytes predict clinical outcome in breast cancer. *Journal of clinical oncology* **2011,** *29* (15), 1949-1955.

38. Eyles, J.; Puaux, A.-L.; Wang, X.; Toh, B.; Prakash, C.; Hong, M.; Tan, T. G.; Zheng, L.; Ong, L. C.; Jin, Y., Tumor cells disseminate early, but immunosurveillance limits metastatic

outgrowth, in a mouse model of melanoma. *The Journal of clinical investigation* **2010,** *120* (6), 2030-2039.

39.   Lopez-Soto, A.; Gonzalez, S.; Smyth, M. J.; Galluzzi, L., Control of metastasis by NK cells. *Cancer cell* **2017,** *32* (2), 135-154.

40.   Smyth, M. J.; Thia, K. Y.; Street, S. E.; Cretney, E.; Trapani, J. A.; Taniguchi, M.; Kawano, T.; Pelikan, S. B.; Crowe, N. Y.; Godfrey, D. I., Differential tumor surveillance by natural killer (NK) and NKT cells. *Journal of Experimental Medicine* **2000,** *191* (4), 661-668.

41.   Ishigami, S.; Natsugoe, S.; Tokuda, K.; Nakajo, A.; Che, X.; Iwashige, H.; Aridome, K.; Hokita, S.; Aikou, T., Prognostic value of intratumoral natural killer cells in gastric carcinoma. *Cancer* **2000,** *88* (3), 577-583.

42.   Cerwenka, A.; Lanier, L. L., Natural killer cell memory in infection, inflammation and cancer. *Nature Reviews Immunology* **2016,** *16* (2), 112.

43.   Keirsse, J.; Van Damme, H.; Van Ginderachter, J. A.; Laoui, D., Exploiting tumor-associated dendritic cell heterogeneity for novel cancer therapies. *Journal of leukocyte biology* **2017,** *102* (2), 317-324.

44.   Ondondo, B. O.; Gallimore, A.; Jones, E. G.; Godkin, A., Home sweet home: the tumor microenvironment as a haven for regulatory T cells. *Frontiers in immunology* **2013,** *4*, 197.

45.   Campbell, M. J.; Tonlaar, N. Y.; Garwood, E. R.; Huo, D.; Moore, D. H.; Khramtsov, A. I.; Au, A.; Baehner, F.; Chen, Y.; Malaka, D. O., Proliferating macrophages associated with high grade, hormone receptor negative breast cancer and poor clinical outcome. *Breast cancer research and treatment* **2011,** *128* (3), 703-711.

46.   Ghajar, C. M.; Bissell, M. J., Extracellular matrix control of mammary gland morphogenesis and tumorigenesis: insights from imaging. *Histochemistry and cell biology* **2008,** *130* (6), 1105.

47.   Acuff, H. B.; Carter, K. J.; Fingleton, B.; Gorden, D. L.; Matrisian, L. M., Matrix metalloproteinase-9 from bone marrow–derived cells contributes to survival but not growth of tumor cells in the lung microenvironment. *Cancer research* **2006,** *66* (1), 259-266.

48.   Ribatti, D.; Crivellato, E., Immune cells and angiogenesis. *Journal of cellular and molecular medicine* **2009,** *13* (9a), 2822-2833.

49.   Camerer, E.; Qazi, A. A.; Duong, D. N.; Cornelissen, I.; Advincula, R.; Coughlin, S. R., Platelets, protease-activated receptors, and fibrinogen in hematogenous metastasis. *Blood* **2004,** *104* (2), 397-401.

50.   Strasner, A., Fibroblast-recruited, tumor-infiltrating CD4+ T cells stimulate mammary cancer metastasis through RANKL-RANK signaling. AACR: 2011.

51.   Schumacher, D.; Strilic, B.; Sivaraj, K. K.; Wettschureck, N.; Offermanns, S., Platelet-derived nucleotides promote tumor-cell transendothelial migration and metastasis via P2Y2 receptor. *Cancer cell* **2013,** *24* (1), 130-137.

52.   Mehlen, P.; Puisieux, A., Metastasis: a question of life or death. *Nature Reviews Cancer* **2006,** *6* (6), 449.

53.   Young, E. W., Cells, tissues, and organs on chips: challenges and opportunities for the cancer tumor microenvironment. *Integrative Biology* **2013,** *5* (9), 1096-1109.

54.   Luca, A. C.; Mersch, S.; Deenen, R.; Schmidt, S.; Messner, I.; Schäfer, K.-L.; Baldus, S. E.; Huckenbeck, W.; Piekorz, R. P.; Knoefel, W. T., Impact of the 3D microenvironment on phenotype, gene expression, and EGFR inhibition of colorectal cancer cell lines. *PloS one* **2013,** *8* (3), e59689.

55.   Buchanan, C. F.; Voigt, E. E.; Szot, C. S.; Freeman, J. W.; Vlachos, P. P.; Rylander, M. N., Three-dimensional microfluidic collagen hydrogels for investigating flow-mediated tumor-endothelial signaling and vascular organization. *Tissue Engineering Part C: Methods* **2013,** *20* (1), 64-75.

56.   Kramer, N.; Walzl, A.; Unger, C.; Rosner, M.; Krupitza, G.; Hengstschläger, M.; Dolznig, H., In vitro cell migration and invasion assays. *Mutation Research/Reviews in Mutation Research* **2013,** *752* (1), 10-24.

57.   Madsen, C. D.; Hooper, S.; Tozluoglu, M.; Bruckbauer, A.; Fletcher, G.; Erler, J. T.; Bates, P. A.; Thompson, B.; Sahai, E., STRIPAK components determine mode of cancer cell migration and metastasis. *Nature cell biology* **2015,** *17* (1), 68.

58.   Pouliot, N.; Pearson, H. B.; Burrows, A., Investigating metastasis using in vitro platforms. In *Madame Curie Bioscience Database [Internet]*, Landes Bioscience: 2013.

59.   Smith, W.; Gamble, J.; Clark-Lewis, I.; Vadas, M., Interleukin-8 induces neutrophil transendothelial migration. *Immunology* **1991,** *72* (1), 65.

60.   Pignatelli, J.; Goswami, S.; Jones, J. G.; Rohan, T. E.; Pieri, E.; Chen, X.; Adler, E.; Cox, D.; Maleki, S.; Bresnick, A., Invasive breast carcinoma cells from patients exhibit MenaINV-and macrophage-dependent transendothelial migration. *Sci. Signal.* **2014,** *7* (353), ra112-ra112.

61.   Li, Y.-H.; Zhu, C., A modified Boyden chamber assay for tumor cell transendothelial migration in vitro. *Clinical & experimental metastasis* **1999,** *17* (5), 423-429.

62.   Tang, Z.; Geng, G.; Huang, Q.; Xu, G.; Hu, H.; Chen, J.; Li, J., Prognostic significance of tissue factor pathway inhibitor-2 in pancreatic carcinoma and its effect on tumor invasion and metastasis. *Medical Oncology* **2010,** *27* (3), 867-875.

63.   Yang, F.; Hu, M.; Lei, Q.; Xia, Y.; Zhu, Y.; Song, X.; Li, Y.; Jie, H.; Liu, C.; Xiong, Y., Nifuroxazide induces apoptosis and impairs pulmonary metastasis in breast cancer model. *Cell death & disease* **2015,** *6* (3), e1701.

64.   Lin, H. H.; Chiang, M. T.; Chang, P. C.; Chau, L. Y., Myeloid heme oxygenase-1 promotes metastatic tumor colonization in mice. *Cancer science* **2015,** *106* (3), 299-306.

65.   Fennema, E.; Rivron, N.; Rouwkema, J.; van Blitterswijk, C.; de Boer, J., Spheroid culture as a tool for creating 3D complex tissues. *Trends in biotechnology* **2013,** *31* (2), 108-115.

66.   LaBarbera, D. V.; Reid, B. G.; Yoo, B. H., The multicellular tumor spheroid model for high-throughput cancer drug discovery. *Expert opinion on drug discovery* **2012,** *7* (9), 819-830.

67.   Hirschhaeuser, F.; Menne, H.; Dittfeld, C.; West, J.; Mueller-Klieser, W.; Kunz-Schughart, L. A., Multicellular tumor spheroids: an underestimated tool is catching up again. *Journal of biotechnology* **2010,** *148* (1), 3-15.

68.   Mehta, G.; Hsiao, A. Y.; Ingram, M.; Luker, G. D.; Takayama, S., Opportunities and challenges for use of tumor spheroids as models to test drug delivery and efficacy. *Journal of Controlled Release* **2012,** *164* (2), 192-204.

69.   Friedrich, J.; Seidel, C.; Ebner, R.; Kunz-Schughart, L. A., Spheroid-based drug screen: considerations and practical approach. *Nature protocols* **2009,** *4* (3), 309.

70.   Fu, C.-Y.; Tseng, S.-Y.; Yang, S.-M.; Hsu, L.; Liu, C.-H.; Chang, H.-Y., A microfluidic chip with a U-shaped microstructure array for multicellular spheroid formation, culturing and analysis. *Biofabrication* **2014,** *6* (1), 015009.

71.   Anada, T.; Fukuda, J.; Sai, Y.; Suzuki, O., An oxygen-permeable spheroid culture system for the prevention of central hypoxia and necrosis of spheroids. *Biomaterials* **2012,** *33* (33), 8430-8441.

72.   Friedrich, J.; Eder, W.; Castaneda, J.; Doss, M.; Huber, E.; Ebner, R.; Kunz-Schughart, L. A., A reliable tool to determine cell viability in complex 3-d culture: the acid phosphatase assay. *Journal of biomolecular screening* **2007,** *12* (7), 925-937.

73.   Mueller-Klieser, W., Multicellular spheroids. *Journal of cancer research and clinical oncology* **1987,** *113* (2), 101-122.

74.   Xu, Z.; Gao, Y.; Hao, Y.; Li, E.; Wang, Y.; Zhang, J.; Wang, W.; Gao, Z.; Wang, Q., Application of a microfluidic chip-based 3D co-culture to test drug sensitivity for individualized treatment of lung cancer. *Biomaterials* **2013,** *34* (16), 4109-4117.

75.   Dark, G. G.; Hill, S. A.; Prise, V. E.; Tozer, G. M.; Pettit, G. R.; Chaplin, D. J., Combretastatin A-4, an agent that displays potent and selective toxicity toward tumor vasculature. *Cancer research* **1997,** *57* (10), 1829-1834.

76.   Nguyen-Ngoc, K.-V.; Cheung, K. J.; Brenot, A.; Shamir, E. R.; Gray, R. S.; Hines, W. C.; Yaswen, P.; Werb, Z.; Ewald, A. J., ECM microenvironment regulates collective migration and

local dissemination in normal and malignant mammary epithelium. *Proceedings of the National Academy of Sciences* **2012,** *109* (39), E2595-E2604.

77.   Tsuchida, T.; Yamada, A.; Yoshimura, K.; Kawamoto, K., Ultrastructural characterization of central neurocytomas using collagen gel culture. *Ultrastructural pathology* **1998,** *22* (3), 233-238.

78.   Miller, B. E.; McInerney, D.; Jackson, D.; Miller, F. R., Metabolic cooperation between mouse mammary tumor subpopulations in three-dimensional collagen gel cultures. *Cancer research* **1986,** *46* (1), 89-93.

79.   Brown, E. B.; Boucher, Y.; Nasser, S.; Jain, R. K., Measurement of macromolecular diffusion coefficients in human tumors. *Microvascular research* **2004,** *67* (3), 231-236.

80.   Ramanujan, S.; Pluen, A.; McKee, T. D.; Brown, E. B.; Boucher, Y.; Jain, R. K., Diffusion and convection in collagen gels: implications for transport in the tumor interstitium. *Biophysical journal* **2002,** *83* (3), 1650-1660.

81.   Yabushita, H.; Ohnishi, M.; Komiyama, M.; Mori, T.; Noguchi, M.; Kishida, T.; Noguchi, Y.; Sawaguchi, K.; Noguchi, M., Usefulness of collagen gel droplet embedded culture drug sensitivity testing in ovarian cancer. *Oncology reports* **2004,** *12* (2), 307-311.

82.   Novak, R.; Didier, M.; Calamari, E.; Ng, C. F.; Choe, Y.; Clauson, S. L.; Nestor, B. A.; Puerta, J.; Fleming, R.; Firoozinezhad, S. J., Scalable fabrication of stretchable, dual channel, microfluidic organ chips. *JoVE (Journal of Visualized Experiments)* **2018,** (140), e58151.

83.   Samatov, T. R.; Senyavina, N. V.; Galatenko, V. V.; Trushkin, E. V.; Tonevitskaya, S. A.; Alexandrov, D. E.; Shibukhova, G. P.; Schumacher, U.; Tonevitsky, A. G., Tumour-like druggable gene expression pattern of CaCo2 cells in microfluidic chip. *BioChip Journal* **2016,** *10* (3), 215-220.

84.   Stucki, A. O.; Stucki, J. D.; Hall, S. R.; Felder, M.; Mermoud, Y.; Schmid, R. A.; Geiser, T.; Guenat, O. T., A lung-on-a-chip array with an integrated bio-inspired respiration mechanism. *Lab on a Chip* **2015,** *15* (5), 1302-1310.

85.   Benam, K. H.; Villenave, R.; Lucchesi, C.; Varone, A.; Hubeau, C.; Lee, H.-H.; Alves, S. E.; Salmon, M.; Ferrante, T. C.; Weaver, J. C., Small airway-on-a-chip enables analysis of human lung inflammation and drug responses in vitro. *Nature methods* **2016,** *13* (2), 151.

86.   Maschmeyer, I.; Lorenz, A. K.; Schimek, K.; Hasenberg, T.; Ramme, A. P.; Hübner, J.; Lindner, M.; Drewell, C.; Bauer, S.; Thomas, A., A four-organ-chip for interconnected long-term co-culture of human intestine, liver, skin and kidney equivalents. *Lab on a Chip* **2015,** *15* (12), 2688-2699.

87.   Musah, S.; Dimitrakakis, N.; Camacho, D. M.; Church, G. M.; Ingber, D. E., Directed differentiation of human induced pluripotent stem cells into mature kidney podocytes and establishment of a Glomerulus Chip. *Nature protocols* **2018,** *13*, 1662-1685.

88.   Kasendra, M.; Tovaglieri, A.; Sontheimer-Phelps, A.; Jalili-Firoozinezhad, S.; Bein, A.; Chalkiadaki, A.; Scholl, W.; Zhang, C.; Rickner, H.; Richmond, C. A., Development of a primary human Small Intestine-on-a-Chip using biopsy-derived organoids. *Scientific reports* **2018,** *8* (1), 2871.

89.   Beckwitt, C. H.; Clark, A. M.; Wheeler, S.; Taylor, D. L.; Stolz, D. B.; Griffith, L.; Wells, A., Liver 'organ on a chip'. *Experimental cell research* **2018,** *363* (1), 15-25.

90.   Sieber, S.; Wirth, L.; Cavak, N.; Koenigsmark, M.; Marx, U.; Lauster, R.; Rosowski, M., Bone marrow-on-a-chip: Long-term culture of human haematopoietic stem cells in a three-dimensional microfluidic environment. *Journal of tissue engineering and regenerative medicine* **2018,** *12* (2), 479-489.

91.   Wang, Y. I.; Abaci, H. E.; Shuler, M. L., Microfluidic blood–brain barrier model provides in vivo-like barrier properties for drug permeability screening. *Biotechnology and bioengineering* **2017,** *114* (1), 184-194.

92.   Musah, S.; Mammoto, A.; Ferrante, T. C.; Jeanty, S. S.; Hirano-Kobayashi, M.; Mammoto, T.; Roberts, K.; Chung, S.; Novak, R.; Ingram, M., Mature induced-pluripotent-stem-cell-derived

human podocytes reconstitute kidney glomerular-capillary-wall function on a chip. *Nature biomedical engineering* **2017,** *1* (5), 0069.

93. Barrile, R.; van der Meer, A. D.; Park, H.; Fraser, J. P.; Simic, D.; Teng, F.; Conegliano, D.; Nguyen, J.; Jain, A.; Zhou, M., Organ-on-Chip Recapitulates Thrombosis Induced by an anti-CD154 Monoclonal Antibody: Translational Potential of Advanced Microengineered Systems. *Clinical pharmacology & therapeutics* **2018,** *104* (6), 1240-1248.

94. Chaudhuri, P. K.; Low, B. C.; Lim, C. T., Mechanobiology of tumor growth. *Chemical reviews* **2018,** *118* (14), 6499-6515.

95. Ma, Y.-H. V.; Middleton, K.; You, L.; Sun, Y., A review of microfluidic approaches for investigating cancer extravasation during metastasis. *Microsystems & Nanoengineering* **2018,** *4*, 17104.

96. van Duinen, V.; Trietsch, S. J.; Joore, J.; Vulto, P.; Hankemeier, T., Microfluidic 3D cell culture: from tools to tissue models. *Current opinion in biotechnology* **2015,** *35*, 118-126.

97. Turcotte, S.; Rosenberg, S. A., Immunotherapy for metastatic solid cancers. *Advances in surgery* **2011,** *45* (1), 341-360.

98. Hsu, T.-H.; Xiao, J.-L.; Tsao, Y.-W.; Kao, Y.-L.; Huang, S.-H.; Liao, W.-Y.; Lee, C.-H., Analysis of the paracrine loop between cancer cells and fibroblasts using a microfluidic chip. *Lab on a chip* **2011,** *11* (10), 1808-1814.

99. Li, R.; Hebert, J. D.; Lee, T. A.; Xing, H.; Boussommier-Calleja, A.; Hynes, R. O.; Lauffenburger, D. A.; Kamm, R. D., Macrophage-secreted TNFα and TGFβ1 influence migration speed and persistence of cancer cells in 3D tissue culture via independent pathways. *Cancer research* **2017,** *77* (2), 279-290.

100. Zervantonakis, I. K.; Hughes-Alford, S. K.; Charest, J. L.; Condeelis, J. S.; Gertler, F. B.; Kamm, R. D., Three-dimensional microfluidic model for tumor cell intravasation and endothelial barrier function. *Proceedings of the National Academy of Sciences* **2012,** *109* (34), 13515-13520.

101. Sun, Y.; Mao, X.; Fan, C.; Liu, C.; Guo, A.; Guan, S.; Jin, Q.; Li, B.; Yao, F.; Jin, F., CXCL12-CXCR4 axis promotes the natural selection of breast cancer cell metastasis. *Tumor Biology* **2014,** *35* (8), 7765-7773.

102. Jeon, J. S.; Bersini, S.; Gilardi, M.; Dubini, G.; Charest, J. L.; Moretti, M.; Kamm, R. D., Human 3D vascularized organotypic microfluidic assays to study breast cancer cell extravasation. *Proceedings of the National Academy of Sciences* **2015,** *112* (1), 214-219.

103. Chen, M. B.; Lamar, J. M.; Li, R.; Hynes, R. O.; Kamm, R. D., Elucidation of the roles of tumor integrin β1 in the extravasation stage of the metastasis cascade. *Cancer research* **2016,** *76* (9), 2513-2524.

104. Wu, X.; Newbold, M. A.; Haynes, C. L., Recapitulation of in vivo-like neutrophil transendothelial migration using a microfluidic platform. *Analyst* **2015,** *140* (15), 5055-5064.

105. Chen, M. B.; Whisler, J. A.; Fröse, J.; Yu, C.; Shin, Y.; Kamm, R. D., On-chip human microvasculature assay for visualization and quantification of tumor cell extravasation dynamics. *Nature protocols* **2017,** *12* (5), 865.

106. Kim, S. K.; Moon, W. K.; Park, J. Y.; Jung, H., Inflammatory mimetic microfluidic chip by immobilization of cell adhesion molecules for T cell adhesion. *Analyst* **2012,** *137* (17), 4062-4068.

107. Han, S.; Yan, J.-J.; Shin, Y.; Jeon, J. J.; Won, J.; Jeong, H. E.; Kamm, R. D.; Kim, Y.-J.; Chung, S., A versatile assay for monitoring in vivo-like transendothelial migration of neutrophils. *Lab on a chip* **2012,** *12* (20), 3861-3865.

108. Haessler, U.; Pisano, M.; Wu, M.; Swartz, M. A., Dendritic cell chemotaxis in 3D under defined chemokine gradients reveals differential response to ligands CCL21 and CCL19. *Proceedings of the National Academy of Sciences* **2011,** *108* (14), 5614-5619.

109. Wang, S.; Li, E.; Gao, Y.; Wang, Y.; Guo, Z.; He, J.; Zhang, J.; Gao, Z.; Wang, Q., Study on invadopodia formation for lung carcinoma invasion with a microfluidic 3D culture device. *PLoS One* **2013,** *8* (2), e56448.

110. Huang, C. P.; Lu, J.; Seon, H.; Lee, A. P.; Flanagan, L. A.; Kim, H.-Y.; Putnam, A. J.; Jeon, N. L., Engineering microscale cellular niches for three-dimensional multicellular co-cultures. *Lab on a Chip* **2009,** *9* (12), 1740-1748.

111. Hassell, B. A.; Goyal, G.; Lee, E.; Sontheimer-Phelps, A.; Levy, O.; Chen, C. S.; Ingber, D. E., Human organ chip models recapitulate orthotopic lung cancer growth, therapeutic responses, and tumor dormancy in vitro. *Cell reports* **2017,** *21* (2), 508-516.

112. Pavesi, A.; Tan, A. T.; Koh, S.; Chia, A.; Colombo, M.; Antonecchia, E.; Miccolis, C.; Ceccarello, E.; Adriani, G.; Raimondi, M. T., A 3D microfluidic model for preclinical evaluation of TCR-engineered T cells against solid tumors. *JCI insight* **2017,** *2* (12).

113. Brouzes, E.; Medkova, M.; Savenelli, N.; Marran, D.; Twardowski, M.; Hutchison, J. B.; Rothberg, J. M.; Link, D. R.; Perrimon, N.; Samuels, M. L., Droplet microfluidic technology for single-cell high-throughput screening. *Proceedings of the National Academy of Sciences* **2009,** *106* (34), 14195-14200.

114. Talmadge, J. E.; Fidler, I. J., AACR centennial series: the biology of cancer metastasis: historical perspective. *Cancer Res* **2010,** *70* (14), 5649-69.

115. Nguyen, D. X.; Bos, P. D.; Massague, J., Metastasis: from dissemination to organ-specific colonization. *Nat Rev Cancer* **2009,** *9* (4), 274-84.

116. Wirtz, D.; Konstantopoulos, K.; Searson, P. C., The physics of cancer: the role of physical interactions and mechanical forces in metastasis. *Nat Rev Cancer* **2011,** *11* (7), 512-22.

117. Joyce, J. A.; Pollard, J. W., Microenvironmental regulation of metastasis. *Nat Rev Cancer* **2009,** *9* (4), 239-52.

118. Fidler, I. J., Metastasis: quantitative analysis of distribution and fate of tumor emboli labeled with 125 I-5-iodo-2'-deoxyuridine. *J Natl Cancer Inst* **1970,** *45* (4), 773-82.

119. Chaffer, C. L.; Weinberg, R. A., A perspective on cancer cell metastasis. *Science* **2011,** *331* (6024), 1559-64.

120. Kienast, Y.; von Baumgarten, L.; Fuhrmann, M.; Klinkert, W. E.; Goldbrunner, R.; Herms, J.; Winkler, F., Real-time imaging reveals the single steps of brain metastasis formation. *Nat Med* **2010,** *16* (1), 116-22.

121. Schluter, K.; Gassmann, P.; Enns, A.; Korb, T.; Hemping-Bovenkerk, A.; Holzen, J.; Haier, J., Organ-specific metastatic tumor cell adhesion and extravasation of colon carcinoma cells with different metastatic potential. *Am J Pathol* **2006,** *169* (3), 1064-73.

122. Witz, I. P., The selectin-selectin ligand axis in tumor progression. *Cancer Metastasis Rev* **2008,** *27* (1), 19-30.

123. Burdick, M. M.; McCaffery, J. M.; Kim, Y. S.; Bochner, B. S.; Konstantopoulos, K., Colon carcinoma cell glycolipids, integrins, and other glycoproteins mediate adhesion to HUVECs under flow. *Am J Physiol Cell Physiol* **2003,** *284* (4), C977-87.

124. Barthel, S. R.; Gavino, J. D.; Descheny, L.; Dimitroff, C. J., Targeting selectins and selectin ligands in inflammation and cancer. *Expert Opin Ther Targets* **2007,** *11* (11), 1473-91.

125. Myung, J. H.; Gajjar, K. A.; Pearson, R. M.; Launiere, C. A.; Eddington, D. T.; Hong, S., Direct measurements on CD24-mediated rolling of human breast cancer MCF-7 cells on E-selectin. *Anal Chem* **2011,** *83* (3), 1078-83.

126. Gay, L. J.; Felding-Habermann, B., Contribution of platelets to tumour metastasis. *Nat Rev Cancer* **2011,** *11* (2), 123-34.

127. Borsig, L.; Wong, R.; Hynes, R. O.; Varki, N. M.; Varki, A., Synergistic effects of L- and P-selectin in facilitating tumor metastasis can involve non-mucin ligands and implicate leukocytes as enhancers of metastasis. *Proc Natl Acad Sci U S A* **2002,** *99* (4), 2193-8.

128. Solinas, G.; Marchesi, F.; Garlanda, C.; Mantovani, A.; Allavena, P., Inflammation-mediated promotion of invasion and metastasis. *Cancer Metastasis Rev* **2010,** *29* (2), 243-8.

129. Kim, S.; Takahashi, H.; Lin, W. W.; Descargues, P.; Grivennikov, S.; Kim, Y.; Luo, J. L.; Karin, M., Carcinoma-produced factors activate myeloid cells through TLR2 to stimulate metastasis. *Nature* **2009,** *457* (7225), 102-6.

130.   Hoshino, A.; Costa-Silva, B.; Shen, T. L.; Rodrigues, G.; Hashimoto, A.; Tesic Mark, M.; Molina, H.; Kohsaka, S.; Di Giannatale, A.; Ceder, S.; Singh, S.; Williams, C.; Soplop, N.; Uryu, K.; Pharmer, L.; King, T.; Bojmar, L.; Davies, A. E.; Ararso, Y.; Zhang, T.; Zhang, H.; Hernandez, J.; Weiss, J. M.; Dumont-Cole, V. D.; Kramer, K.; Wexler, L. H.; Narendran, A.; Schwartz, G. K.; Healey, J. H.; Sandstrom, P.; Labori, K. J.; Kure, E. H.; Grandgenett, P. M.; Hollingsworth, M. A.; de Sousa, M.; Kaur, S.; Jain, M.; Mallya, K.; Batra, S. K.; Jarnagin, W. R.; Brady, M. S.; Fodstad, O.; Muller, V.; Pantel, K.; Minn, A. J.; Bissell, M. J.; Garcia, B. A.; Kang, Y.; Rajasekhar, V. K.; Ghajar, C. M.; Matei, I.; Peinado, H.; Bromberg, J.; Lyden, D., Tumour exosome integrins determine organotropic metastasis. *Nature* **2015,** *527* (7578), 329-35.
131.   Hood, J. L.; San, R. S.; Wickline, S. A., Exosomes released by melanoma cells prepare sentinel lymph nodes for tumor metastasis. *Cancer Res* **2011,** *71* (11), 3792-801.
132.   Kaplan, R. N.; Riba, R. D.; Zacharoulis, S.; Bramley, A. H.; Vincent, L.; Costa, C.; MacDonald, D. D.; Jin, D. K.; Shido, K.; Kerns, S. A.; Zhu, Z.; Hicklin, D.; Wu, Y.; Port, J. L.; Altorki, N.; Port, E. R.; Ruggero, D.; Shmelkov, S. V.; Jensen, K. K.; Rafii, S.; Lyden, D., VEGFR1-positive haematopoietic bone marrow progenitors initiate the pre-metastatic niche. *Nature* **2005,** *438* (7069), 820-7.
133.   Shiozawa, Y.; Pedersen, E. A.; Havens, A. M.; Jung, Y.; Mishra, A.; Joseph, J.; Kim, J. K.; Patel, L. R.; Ying, C.; Ziegler, A. M.; Pienta, M. J.; Song, J.; Wang, J.; Loberg, R. D.; Krebsbach, P. H.; Pienta, K. J.; Taichman, R. S., Human prostate cancer metastases target the hematopoietic stem cell niche to establish footholds in mouse bone marrow. *J Clin Invest* **2011,** *121* (4), 1298-312.
134.   Provenzano, P. P.; Eliceiri, K. W.; Keely, P. J., Multiphoton microscopy and fluorescence lifetime imaging microscopy (FLIM) to monitor metastasis and the tumor microenvironment. *Clin Exp Metastasis* **2009,** *26* (4), 357-70.
135.   Bersini, S.; Jeon, J. S.; Dubini, G.; Arrigoni, C.; Chung, S.; Charest, J. L.; Moretti, M.; Kamm, R. D., A microfluidic 3D in vitro model for specificity of breast cancer metastasis to bone. *Biomaterials* **2014,** *35* (8), 2454-61.
136.   Jeon, J. S.; Bersini, S.; Gilardi, M.; Dubini, G.; Charest, J. L.; Moretti, M.; Kamm, R. D., Human 3D vascularized organotypic microfluidic assays to study breast cancer cell extravasation. *Proc Natl Acad Sci U S A* **2015,** *112* (1), 214-9.
137.   Niu, Y.; Bai, J.; Kamm, R. D.; Wang, Y.; Wang, C., Validating antimetastatic effects of natural products in an engineered microfluidic platform mimicking tumor microenvironment. *Mol Pharm* **2014,** *11* (7), 2022-9.
138.   Zervantonakis, I. K.; Hughes-Alford, S. K.; Charest, J. L.; Condeelis, J. S.; Gertler, F. B.; Kamm, R. D., Three-dimensional microfluidic model for tumor cell intravasation and endothelial barrier function. *Proc Natl Acad Sci U S A* **2012,** *109* (34), 13515-20.
139.   Song, J. W.; Cavnar, S. P.; Walker, A. C.; Luker, K. E.; Gupta, M.; Tung, Y. C.; Luker, G. D.; Takayama, S., Microfluidic endothelium for studying the intravascular adhesion of metastatic breast cancer cells. *PLoS One* **2009,** *4* (6), e5756.
140.   Zhang, Q.; Liu, T.; Qin, J., A microfluidic-based device for study of transendothelial invasion of tumor aggregates in realtime. *Lab Chip* **2012,** *12* (16), 2837-42.
141.   Roberts, S. A.; Waziri, A. E.; Agrawal, N., Development of a Single-Cell Migration and Extravasation Platform through Selective Surface Modification. *Anal Chem* **2016,** *88* (5), 2770-6.
142.   Pisano, M.; Triacca, V.; Barbee, K. A.; Swartz, M. A., An in vitro model of the tumor-lymphatic microenvironment with simultaneous transendothelial and luminal flows reveals mechanisms of flow enhanced invasion. *Integr Biol (Camb)* **2015,** *7* (5), 525-33.
143.   Huang, R.; Zheng, W.; Liu, W.; Zhang, W.; Long, Y.; Jiang, X., Investigation of Tumor Cell Behaviors on a Vascular Microenvironment-Mimicking Microfluidic Chip. *Sci Rep* **2015,** *5*, 17768.
144.   Wang, X. Y.; Pei, Y.; Xie, M.; Jin, Z. H.; Xiao, Y. S.; Wang, Y.; Zhang, L. N.; Li, Y.; Huang, W. H., An artificial blood vessel implanted three-dimensional microsystem for modeling transvascular migration of tumor cells. *Lab Chip* **2015,** *15* (4), 1178-87.

145.	Coclite, A.; de Tullio, M. D.; Pascazio, G.; Decuzzi, P., A combined Lattice Boltzmann and Immersed boundary approach for predicting the vascular transport of differently shaped particles. *Computers & Fluids* **2016,** *136*, 260-271.

146.	Coclite, A.; Mollica, H.; Ranaldo, S.; Pascazio, G.; de Tullio, M. D.; Decuzzi, P., Predicting different adhesive regimens of circulating particles at blood capipllary walls. *Under Review* **2017**.

147.	Bhatnagar, P. L.; Gross, E. P.; Krook, M., A Model for Collision Processes in Gases. I. Small Amplitude Processes in Charged and Neutral One-Component Systems. *Phys. Rev.* **1954,** *94* (3), 511-525.

148.	Shan, X. W.; Yuan, X. F.; Chen, H. D., Kinetic theory representation of hydrodynamics: a way beyond the Navier-Stokes equation. *Journal of Fluid Mechanics* **2006,** *550*, 413-441.

149.	Zou, Q. S.; He, X. Y., On pressure and velocity boundary conditions for the lattice Boltzmann BGK model. *Physics of Fluids* **1997,** *9* (6), 1591-1598.

150.	Sun, C.; Munn, L. L., Lattice Boltzmann simulation of blood flow in digitized vessel networks. *Comput Math Appl* **2008,** *55* (7), 1594-1600.

151.	Flatmark, K.; Maelandsmo, G. M.; Martinsen, M.; Rasmussen, H.; Fodstad, O., Twelve colorectal cancer cell lines exhibit highly variable growth and metastatic capacities in an orthotopic model in nude mice. *Eur J Cancer* **2004,** *40* (10), 1593-8.

152.	Holliday, D. L.; Speirs, V., Choosing the right cell line for breast cancer research. *Breast Cancer Res* **2011,** *13* (4), 215.

153.	Popel, A. S.; Johnson, P. C., Microcirculation and Hemorheology. *Annu Rev Fluid Mech* **2005,** *37*, 43-69.

154.	Ríos-Navarro, C.; de Pablo, C.; Collado-Diaz, V.; Orden, S.; Blas-Garcia, A.; Martínez-Cuesta, M. Á.; Esplugues, J. V.; Alvarez, A., Differential effects of anti-TNF-α and anti-IL-12/23 agents on human leukocyte–endothelial cell interactions. *European journal of pharmacology* **2015,** *765*, 355-365.

155.	Granger, D. N.; Senchenkova, E. In *Inflammation and the Microcirculation*, Colloquium Series on Integrated Systems Physiology: From Molecule to Function, Morgan & Claypool Life Sciences: 2010; pp 1-87.

156.	Strell, C.; Entschladen, F., Extravasation of leukocytes in comparison to tumor cells. *Cell Communication and Signaling* **2008,** *6* (1), 10.

157.	McEver, R. P.; Zhu, C., Rolling cell adhesion. *Annual review of cell and developmental biology* **2010,** *26*, 363-396.

158.	Goldsmith, H. L.; Cokelet, G. R.; Gaehtgens, P., Robin Fahraeus: evolution of his concepts in cardiovascular physiology. *Am J Physiol* **1989,** *257* (3 Pt 2), H1005-15.

159.	Pappu, V.; Bagchi, P., Hydrodynamic interaction between erythrocytes and leukocytes affects rheology of blood in microvessels. *Biorheology* **2007,** *44* (3), 191-215.

160.	Fedosov, D. A.; Noguchi, H.; Gompper, G., Multiscale modeling of blood flow: from single cells to blood rheology. *Biomech Model Mechanobiol* **2014,** *13* (2), 239-58.

161.	Firrell, J. C.; Lipowsky, H. H., Leukocyte margination and deformation in mesenteric venules of rat. *Am J Physiol* **1989,** *256* (6 Pt 2), H1667-74.

162.	Decuzzi, P.; Ferrari, M., The adhesive strength of non-spherical particles mediated by specific interactions. *Biomaterials* **2006,** *27* (30), 5307-14.

163.	Coclite, A.; Mollica, H.; Ranaldo, S.; Pascazio, G.; de Tullio, M. D.; Decuzzi, P., Predicting different adhesive regimens of circulating particles at blood capillary walls. *Microfluidics and Nanofluidics* **2017,** *21* (11), 168.

164.	Fedosov, D. A.; Caswell, B.; Karniadakis, G. E., Wall shear stress-based model for adhesive dynamics of red blood cells in malaria. *Biophysical journal* **2011,** *100* (9), 2084-2093.

165.	Muller, K.; Fedosov, D. A.; Gompper, G., Margination of micro- and nano-particles in blood flow and its effect on drug delivery. *Sci Rep* **2014,** *4*, 4871.

166.	Steeg, P. S., Targeting metastasis. *Nat Rev Cancer* **2016,** *16* (4), 201-18.

167. Gupta, G. P.; Massagué, J., Cancer metastasis: building a framework. *Cell* **2006,** *127* (4), 679-695.

168. Wirtz, D.; Konstantopoulos, K.; Searson, P. C., The physics of cancer: the role of physical interactions and mechanical forces in metastasis. *Nature Reviews Cancer* **2011,** *11* (7), 512.

169. Macara, I. G.; McCaffrey, L., Cell polarity in morphogenesis and metastasis. *Phil. Trans. R. Soc. B* **2013,** *368* (1629), 20130012.

170. Ewing, J., Neoplastic diseases; a treatise on tumors. In *cdl; americana*, University of California Libraries: Philadelphia London, W. B. Saunders company 1922; pp 987-1031.

171. Cristofanilli, M.; Hayes, D. F.; Budd, G. T.; Ellis, M. J.; Stopeck, A.; Reuben, J. M.; Doyle, G. V.; Matera, J.; Allard, W. J.; Miller, M. C., Circulating tumor cells: a novel prognostic factor for newly diagnosed metastatic breast cancer. *Journal of clinical oncology* **2005,** *23* (7), 1420-1430.

172. Azevedo, A. S.; Follain, G.; Patthabhiraman, S.; Harlepp, S.; Goetz, J. G., Metastasis of circulating tumor cells: favorable soil or suitable biomechanics, or both? *Cell adhesion & migration* **2015,** *9* (5), 345-356.

173. Yu, M.; Stott, S.; Toner, M.; Maheswaran, S.; Haber, D. A., Circulating tumor cells: approaches to isolation and characterization. *The Journal of cell biology* **2011,** *192* (3), 373-382.

174. Stuelten, C. H.; Parent, C. A.; Montell, D. J., Cell motility in cancer invasion and metastasis: insights from simple model organisms. *Nat Rev Cancer* **2018,** *18* (5), 296-312.

175. van Marion, D. M.; Domanska, U. M.; Timmer-Bosscha, H.; Walenkamp, A. M., Studying cancer metastasis: existing models, challenges and future perspectives. *Critical reviews in oncology/hematology* **2016,** *97*, 107-117.

176. Miles, W. O.; Dyson, N. J.; Walker, J. A., Modeling tumor invasion and metastasis in Drosophila. *Dis Model Mech* **2011,** *4* (6), 753-61.

177. Beaucher, M.; Hersperger, E.; Page-McCaw, A.; Shearn, A., Metastatic ability of Drosophila tumors depends on MMP activity. *Dev Biol* **2007,** *303* (2), 625-34.

178. Cock-Rada, A. M.; Medjkane, S.; Janski, N.; Yousfi, N.; Perichon, M.; Chaussepied, M.; Chluba, J.; Langsley, G.; Weitzman, J. B., SMYD3 promotes cancer invasion by epigenetic upregulation of the metalloproteinase MMP-9. *Cancer Res* **2012,** *72* (3), 810-20.

179. Osswald, M.; Jung, E.; Sahm, F.; Solecki, G.; Venkataramani, V.; Blaes, J.; Weil, S.; Horstmann, H.; Wiestler, B.; Syed, M.; Huang, L.; Ratliff, M.; Karimian Jazi, K.; Kurz, F. T.; Schmenger, T.; Lemke, D.; Gommel, M.; Pauli, M.; Liao, Y.; Haring, P.; Pusch, S.; Herl, V.; Steinhauser, C.; Krunic, D.; Jarahian, M.; Miletic, H.; Berghoff, A. S.; Griesbeck, O.; Kalamakis, G.; Garaschuk, O.; Preusser, M.; Weiss, S.; Liu, H.; Heiland, S.; Platten, M.; Huber, P. E.; Kuner, T.; von Deimling, A.; Wick, W.; Winkler, F., Brain tumour cells interconnect to a functional and resistant network. *Nature* **2015,** *528* (7580), 93-8.

180. Kimura, H.; Hayashi, K.; Yamauchi, K.; Yamamoto, N.; Tsuchiya, H.; Tomita, K.; Kishimoto, H.; Bouvet, M.; Hoffman, R. M., Real-time imaging of single cancer-cell dynamics of lung metastasis. *J Cell Biochem* **2010,** *109* (1), 58-64.

181. Bouvet, M.; Wang, J.; Nardin, S. R.; Nassirpour, R.; Yang, M.; Baranov, E.; Jiang, P.; Moossa, A. R.; Hoffman, R. M., Real-time optical imaging of primary tumor growth and multiple metastatic events in a pancreatic cancer orthotopic model. *Cancer Res* **2002,** *62* (5), 1534-40.

182. Zhang, Y.; Toneri, M.; Ma, H.; Yang, Z.; Bouvet, M.; Goto, Y.; Seki, N.; Hoffman, R. M., Real-Time GFP Intravital Imaging of the Differences in Cellular and Angiogenic Behavior of Subcutaneous and Orthotopic Nude-Mouse Models of Human PC-3 Prostate Cancer. *J Cell Biochem* **2016,** *117* (11), 2546-51.

183. Garona, J.; Alonso, D. F., Urokinase Exerts Antimetastatic Effects by Dissociating Clusters of Circulating Tumor Cells-Letter. *Cancer Res* **2016,** *76* (16), 4908.

184. Albini, A.; Benelli, R., The chemoinvasion assay: a method to assess tumor and endothelial cell invasion and its modulation. *Nat Protoc* **2007,** *2* (3), 504-11.

185. Chaw, K. C.; Manimaran, M.; Tay, E. H.; Swaminathan, S., Multi-step microfluidic device for studying cancer metastasis. *Lab Chip* **2007,** *7* (8), 1041-7.

186.   Li, J.; Zhu, L.; Zhang, M.; Lin, F., Microfluidic device for studying cell migration in single or co-existing chemical gradients and electric fields. *Biomicrofluidics* **2012,** *6* (2), 24121-2412113.

187.   Chung, S.; Sudo, R.; Mack, P. J.; Wan, C. R.; Vickerman, V.; Kamm, R. D., Cell migration into scaffolds under co-culture conditions in a microfluidic platform. *Lab Chip* **2009,** *9* (2), 269-75.

188.   Chen, M. B.; Lamar, J. M.; Li, R.; Hynes, R. O.; Kamm, R. D., Elucidation of the Roles of Tumor Integrin beta1 in the Extravasation Stage of the Metastasis Cascade. *Cancer Res* **2016,** *76* (9), 2513-24.

189.   Chen, M. B.; Whisler, J. A.; Jeon, J. S.; Kamm, R. D., Mechanisms of tumor cell extravasation in an in vitro microvascular network platform. *Integr Biol (Camb)* **2013,** *5* (10), 1262-71.

190.   Thompson, T. J.; Han, B., Analysis of adhesion kinetics of cancer cells on inflamed endothelium using a microfluidic platform. *Biomicrofluidics* **2018,** *12* (4), 042215.

191.   Manneschi, C.; Pereira, R.; Marinaro, G.; Bosca, A.; Francardi, M.; Decuzzi, P., A microfluidic platform with permeable walls for the analysis of vascular and extravascular mass transport. *Microfluidics and Nanofluidics* **2016,** *20* (8), 113.

192.   Mollica, H.; Coclite, A.; Miali, M. E.; Pereira, R. C.; Paleari, L.; Manneschi, C.; DeCensi, A.; Decuzzi, P., Deciphering the relative contribution of vascular inflammation and blood rheology in metastatic spreading. *Biomicrofluidics* **2018,** *12* (4), 042205.

193.   Albelda, S. M.; Sampson, P. M.; Haselton, F. R.; McNiff, J.; Mueller, S.; Williams, S.; Fishman, A.; Levine, E., Permeability characteristics of cultured endothelial cell monolayers. *Journal of Applied Physiology* **1988,** *64* (1), 308-322.

194.   Popel, A. S.; Johnson, P. C., Microcirculation and hemorheology. *Annu. Rev. Fluid Mech.* **2005,** *37*, 43-69.

195.   van Zijl, F.; Krupitza, G.; Mikulits, W., Initial steps of metastasis: cell invasion and endothelial transmigration. *Mutation Research/Reviews in Mutation Research* **2011,** *728* (1), 23-34.

196.   Martin, T. A.; Ye, L.; Sanders, A. J.; Lane, J.; Jiang, W. G., Cancer invasion and metastasis: molecular and cellular perspective. In *Madame Curie Bioscience Database [Internet]*, Landes Bioscience: 2013.

197.   Ghaffari, A.; Hoskin, V.; Turashvili, G.; Varma, S.; Mewburn, J.; Mullins, G.; Greer, P. A.; Kiefer, F.; Day, A. G.; Madarnas, Y., Intravital imaging reveals systemic ezrin inhibition impedes cancer cell migration and lymph node metastasis in breast cancer. *Breast Cancer Research* **2019,** *21* (1), 12.

198.   Sun, W.; Lim, C. T.; Kurniawan, N. A., Mechanistic adaptability of cancer cells strongly affects anti-migratory drug efficacy. *Journal of The Royal Society Interface* **2014,** *11* (99), 20140638.

199.   Kurniawan, N. A.; Chaudhuri, P. K.; Lim, C. T., Concentric gel system to study the biophysical role of matrix microenvironment on 3D cell migration. *JoVE (Journal of Visualized Experiments)* **2015,** (98), e52735.

200.   Stoletov, K.; Kato, H.; Zardouzian, E.; Kelber, J.; Yang, J.; Shattil, S.; Klemke, R., Visualizing extravasation dynamics of metastatic tumor cells. *J Cell Sci* **2010,** *123* (13), 2332-2341.

201.   Beerling, E.; Oosterom, I.; Voest, E.; Lolkema, M.; van Rheenen, J., Intravital characterization of tumor cell migration in pancreatic cancer. *Intravital* **2016,** *5* (3), e1261773.

202.   Wyckoff, J. B.; Jones, J. G.; Condeelis, J. S.; Segall, J. E., A critical step in metastasis: in vivo analysis of intravasation at the primary tumor. *Cancer research* **2000,** *60* (9), 2504-2511.

203.   Zijlstra, A.; Lewis, J.; DeGryse, B.; Stuhlmann, H.; Quigley, J. P., The inhibition of tumor cell intravasation and subsequent metastasis via regulation of in vivo tumor cell motility by the tetraspanin CD151. *Cancer cell* **2008,** *13* (3), 221-234.

204.   Ilic, M.; Ilic, I., Epidemiology of pancreatic cancer. *World journal of gastroenterology* **2016,** *22* (44), 9694.

205.   Alderton, G. K., Pancreatic cancer: PDAC subtypes. *Nature Reviews Cancer* **2015,** *15* (10), 575.

206.   Burris, H. r.; Moore, M. J.; Andersen, J.; Green, M. R.; Rothenberg, M. L.; Modiano, M. R.; Christine Cripps, M.; Portenoy, R. K.; Storniolo, A. M.; Tarassoff, P., Improvements in survival and clinical benefit with gemcitabine as first-line therapy for patients with advanced pancreas cancer: a randomized trial. *Journal of clinical oncology* **1997,** *15* (6), 2403-2413.

207.   Conroy, T.; Desseigne, F.; Ychou, M.; Bouché, O.; Guimbaud, R.; Bécouarn, Y.; Adenis, A.; Raoul, J.-L.; Gourgou-Bourgade, S.; de la Fouchardière, C., FOLFIRINOX versus gemcitabine for metastatic pancreatic cancer. *New England Journal of Medicine* **2011,** *364* (19), 1817-1825.

208.   Hajatdoost, L.; Sedaghat, K.; Walker, E. J.; Thomas, J.; Kosari, S., Chemotherapy in pancreatic cancer: A systematic review. *Medicina* **2018,** *54* (3), 48.

209.   Liu, Q.; Liao, Q.; Zhao, Y., Chemotherapy and tumor microenvironment of pancreatic cancer. *Cancer cell international* **2017,** *17* (1), 68.

210.   Protti, M. P.; De Monte, L., Immune infiltrates as predictive markers of survival in pancreatic cancer patients. *Frontiers in physiology* **2013,** *4*, 210.

211.   Yu, X.; Ji, S.; Xu, J.; Yao, W.; Qu, B.; Zhu, W.; Xu, W.; Zhang, B.; Xu, Y., CD8+ T Cells are compromised in human pancreatic cancer. *Transl Med* **2012,** *2* (105), 2161-1025.1000105.

212.   Ino, Y.; Yamazaki-Itoh, R.; Shimada, K.; Iwasaki, M.; Kosuge, T.; Kanai, Y.; Hiraoka, N., Immune cell infiltration as an indicator of the immune microenvironment of pancreatic cancer. *British journal of cancer* **2013,** *108* (4), 914-923.

213.   Nomi, T.; Sho, M.; Akahori, T.; Hamada, K.; Kubo, A.; Kanehiro, H.; Nakamura, S.; Enomoto, K.; Yagita, H.; Azuma, M., Clinical significance and therapeutic potential of the programmed death-1 ligand/programmed death-1 pathway in human pancreatic cancer. *Clinical cancer research* **2007,** *13* (7), 2151-2157.

214.   Salmaninejad, A.; Valilou, S. F.; Shabgah, A. G.; Aslani, S.; Alimardani, M.; Pasdar, A.; Sahebkar, A., PD-1/PD-L1 pathway: Basic biology and role in cancer immunotherapy. *Journal of cellular physiology* **2019**.

215.   Bang, S.; Kim, H.-S.; Choo, Y. S.; Park, S. W.; Chung, J. B.; Song, S. Y., Differences in immune cells engaged in cell-mediated immunity after chemotherapy for far advanced pancreatic cancer. *Pancreas* **2006,** *32* (1), 29-36.

216.   Apte, M.; Haber, P.; Applegate, T.; Norton, I.; McCaughan, G.; Korsten, M.; Pirola, R.; Wilson, J., Periacinar stellate shaped cells in rat pancreas: identification, isolation, and culture. *Gut* **1998,** *43* (1), 128-133.

217.   Apte, M.; Haber, P.; Darby, S.; Rodgers, S.; McCaughan, G.; Korsten, M.; Pirola, R.; Wilson, J., Pancreatic stellate cells are activated by proinflammatory cytokines: implications for pancreatic fibrogenesis. *Gut* **1999,** *44* (4), 534-541.

218.   Tang, D.; Yuan, Z.; Xue, X.; Lu, Z.; Zhang, Y.; Wang, H.; Chen, M.; An, Y.; Wei, J.; Zhu, Y., High expression of Galectin-1 in pancreatic stellate cells plays a role in the development and maintenance of an immunosuppressive microenvironment in pancreatic cancer. *International journal of cancer* **2012,** *130* (10), 2337-2348.

219.   Guo, S.; Contratto, M.; Miller, G.; Leichman, L.; Wu, J., Immunotherapy in pancreatic cancer: Unleash its potential through novel combinations. *World journal of clinical oncology* **2017,** *8* (3), 230.

220.   Gjertsen, M. K.; Breivik, J.; Saeterdal, I.; Thorsby, E.; Gaudernack, G.; Bakka, A.; Søreide, O.; Solheim, B., Vaccination with mutant ras peptides and induction of T-cell responsiveness in pancreatic carcinoma patients carrying the corresponding RAS mutation. *The Lancet* **1995,** *346* (8987), 1399-1400.

221.   Chmielewski, M.; Hahn, O.; Rappl, G.; Nowak, M.; Schmidt–Wolf, I. H.; Hombach, A. A.; Abken, H., T cells that target carcinoembryonic antigen eradicate orthotopic pancreatic carcinomas without inducing autoimmune colitis in mice. *Gastroenterology* **2012,** *143* (4), 1095-1107. e2.

222.   Winograd, R.; Byrne, K. T.; Evans, R. A.; Odorizzi, P. M.; Meyer, A. R.; Bajor, D. L.; Clendenin, C.; Stanger, B. Z.; Furth, E. E.; Wherry, E. J., Induction of T-cell immunity overcomes

complete resistance to PD-1 and CTLA-4 blockade and improves survival in pancreatic carcinoma. *Cancer immunology research* **2015,** *3* (4), 399-411.

223.   Augustine, T. N.; Dix-Peek, T.; Duarte, R.; Candy, G. P., Establishment of a heterotypic 3D culture system to evaluate the interaction of TREG lymphocytes and NK cells with breast cancer. *Journal of immunological methods* **2015,** *426*, 1-13.

224.   Nandagopal, S.; Wu, D.; Lin, F., Combinatorial guidance by CCR7 ligands for T lymphocytes migration in co-existing chemokine fields. *PloS one* **2011,** *6* (3), e18183.

225.   Bai, J.; Adriani, G.; Dang, T.-M.; Tu, T.-Y.; Penny, H.-X. L.; Wong, S.-C.; Kamm, R. D.; Thiery, J.-P., Contact-dependent carcinoma aggregate dispersion by M2a macrophages via ICAM-1 and β2 integrin interactions. *Oncotarget* **2015,** *6* (28), 25295.

226.   Beer, M.; Kuppalu, N.; Stefanini, M.; Becker, H.; Schulz, I.; Manoli, S.; Schuette, J.; Schmees, C.; Casazza, A.; Stelzle, M., A novel microfluidic 3D platform for culturing pancreatic ductal adenocarcinoma cells: comparison with in vitro cultures and in vivo xenografts. *Scientific reports* **2017,** *7* (1), 1325.

227.   Neurauter, A. A.; Bonyhadi, M.; Lien, E.; Nøkleby, L.; Ruud, E.; Camacho, S.; Aarvak, T., Cell isolation and expansion using Dynabeads®. In *Cell separation*, Springer: 2007; pp 41-73.